PROPAGATION OF HIGH POWER PULSES OF 10.6 μm RADIATION FROM A CO_2 TEA LASER OF NOVEL DESIGN THROUGH CLOUDS PRODUCED BY ADIABATIC EXPANSION IN THE LABORATORY

Final Technical Report

P. F. Browne and P. M. Webber

July 1976

EUROPEAN RESEARCH OFFICE
United States Army
London NW1 5TH, England

Contract Number DAJA37-74-C-1686

University of Manchester Institute of Science and Technology
Manchester M60 1QD, England

UNCLASSIFIED

SECURITY CLASSIFICATION OF THIS PAGE (When Data Entered)

REPORT DOCUMENTATION PAGE	READ INSTRUCTIONS BEFORE COMPLETING FORM
1. REPORT NUMBER	2. GOVT ACCESSION NO. micrometers 3. RECIPIENT'S CATALOG NUMBER (9)
4. TITLE (and Subtitle) (6) PROPAGATION OF HIGH POWER PULSES OF 10.6 RADIATION FROM A CO_2 TEA LASER OF NOVEL DESIGN THROUGH CLOUDS PRODUCED BY ADIABATIC EXPANSION IN THE LABORATORY	5. TYPE OF REPORT & PERIOD COVERED FINAL TECHNICAL REPORT FEB - Jul 76 6. PERFORMING ORG. REPORT NUMBER
7. AUTHOR(s) (10) P.F. BROWNE & P.M. WEBBER	8. CONTRACT OR GRANT NUMBER(s) (15) DAJA37-74-C-1686 NEW
9. PERFORMING ORGANIZATION NAME AND ADDRESS UNIVERSITY OF MANCHESTER INSTITUTE OF SCIENCE & TECHNOLOGY MANCHESTER M60 1QD UK	10. PROGRAM ELEMENT, PROJECT, TASK AREA & WORK UNIT NUMBERS (16) 61102A-DM161103B53B-00-338 (17)
11. CONTROLLING OFFICE NAME AND ADDRESS USA R&S GRP(EUR) BOX 65 FPO NEW YORK 09510	12. REPORT DATE (11) JUL 76 13. NUMBER OF PAGES 96 (12) 99 p.
14. MONITORING AGENCY NAME & ADDRESS(if different from Controlling Office)	15. SECURITY CLASS. (of this report) UNCLASSIFIED 15a. DECLASSIFICATION/DOWNGRADING SCHEDULE

16. DISTRIBUTION STATEMENT (of this Report)

APPROVED FOR PUBLIC RELEASE
DISTRIBUTION UNLIMITED

17. DISTRIBUTION STATEMENT (of the abstract entered in Block 20, if different from Report)

DDC RECEIVED NOV 12 1976 B

18. SUPPLEMENTARY NOTES

19. KEY WORDS (Continue on reverse side if necessary and identify by block number)

(U) TEA LASER: (U) DIFFUSION: (U) CLOUD CLEARING:

(U) REFRACTURE INDEX CHARGES

407 a 78

20. ABSTRACT (Continue on reverse side if necessary and identify by block number)

This report describes (a) theory, design and performance of a CO_2 TEA laser with VUV preionization delivering typically 25J pulses of duration 0.1μs and beam cross section 20cm^2 ; (b) the production of clouds in the laboratory by adiabatic expansion of compressed gas in a 300 l glass chamber and the measurement of the cloud parameters (liquid water content, drop radius); (c) measurements of attenuation by such clouds of TEA laser pulses of the above type and also measurement of partial cloud clearing by a CW 10.6μm

DD FORM 1 JAN 73 1473 EDITION OF 1 NOV 68 IS OBSOLETE

UNCLASSIFIED

SECURITY CLASSIFICATION OF THIS PAGE (When Data Entered)

Beam (by recording the change in attenuation of a collinear He-Ne beam); and (d) the theory required to understand the interaction between 10.6μm radiation and clouds of droplets.

AD

PROPAGATION OF HIGH POWER PULSES OF 10.6μm RADIATION FROM A CO_2 TEA LASER OF NOVEL DESIGN THROUGH CLOUDS PRODUCED BY ADIABATIC EXPANSION IN THE LABORATORY

Final Technical Report

By

P.F.Browne and P.M.Webber

JULY, 1976

EUROPEAN RESEARCH OFFICE
United States Army
London NW1 5TH, England

Contract Number DAJA 37-74-C-1686

University of Manchester Institute of Science and Technology
Manchester M60 1QD, England

ABSTRACT

This report describes (a) theory, design and performance of a CO_2 TEA laser with VUV preionization delivering typically 2J pulses of duration 0.1μs and beam cross section 20cm²; (b) the production of clouds in the laboratory by adiabatic expansion of compressed gas in a 300 l glass chamber and the measurement of the cloud parameters (liquid water content, drop radius); (c) measurements of attenuation by such clouds of TEA laser pulses of the above type and also measurement of partial cloud clearing by a CW 10.6μm beam (by recording the change in attenuation of a collinear He-Ne beam); and (d) the theory required to understand the interaction between 10.6μm radiation and clouds of droplets.

CONTENT

INTRODUCTION

Infrared imaging systems and ranging devices are often limited by the transmission of the atmosphere at the wavelength used. The atmosphere is particularly clear at 10.6μm, the wavelength of CO_2 lasers which offer versatility, efficiency and high power. This report is concerned with the attenuation of 10.6μm radiations, both high power pulsed and CW, by fogs and clouds of water droplets.

Any mechanism which produces absorption has the further consequence of causing thermal blooming (i.e. a negative lens effect) and beam deflection in the atmosphere. These effects have received much attention in the literature (see appendix X1) since they effectively determine the power concentrations that can be achieved by laser beams at long range. Absorption of 10.6μm radiation by mists, fogs or clouds clearly must contribute to thermal blooming.

Part A of this report describes the theory, design and performance of a CO_2 TEA laser with VUV preionization, delivering typically 25J, 0.1μs pulses of 10.6μm radiation over a beam cross section of about $20cm^2$. Design of a conventional CW CO_2 laser is also reported.

Part B describes the production of laboratory fogs by adiabatic expansion of compressed gas in a 300 litre glass chamber (diameter 0.5m, length 1.5m). Falls in temperature of order 10K are produced by sudden venting to the atmosphere and the quantity of liquid water condensed is determined from the measured temperature fall and the expansion ratio. The quality of the fog, i.e. the drop size, is determined by the concentration of effective condensation nuclei; both smoke and ions have been used. Typically, fogs contain about 4g m^{-3} of liquid water which gives an optical depth to 10.6μm of order 1.5m.

Part C describes results obtained to date. The attenuation of TEA laser pulses of energy density ~1J cm^{-2} over $20cm^2$ beam cross section has been measured at various times during evolution of a cloud whose 0.63μm attenuation coefficient is automatically charted. Attenuations at 10.6μm (in dB m^{-1}) are over ten times less than at 0.63μm for our clouds whose mean drop radius is ~1.5μm. Attenuations at 10.6μm are close to what is expected for absorption by the equivalent layer of liquid water — 0.4dB m^{-1} per g m^{-3} of liquid water. For larger drops scattering will no longer be insignificant. The change in transmittance of a 0.63μm beam due to drop evaporation by a collinear CW CO_2 beam has also been measured, with results similar to those reported by Mullaney et al.

In Part D the theoretical basis for interpreting scattering and attenuation by drops is outlined and the literature briefly surveyed, including cloud clearing measurements.

PART A: CO_2 LASER DEVELOPMENT

Section A1. High Power CO_2 TEA Laser (see also reference A1 and appendix X3)

(I) Mechanical design features

Figures A1 and A2 show the main constructional details for the TEA laser. Bruce-profiled solid aluminium electrodes with base dimensions of 50cm x 15cm, and with separation 6cm, are positioned inside a rectangular box made from ½" perspex (dimensions 105cm x35cm x 25cm). The upper electrode is supported from a lid (not shown) which covers a cut-away section of the top face of the perspex box, being screwed down on top of a rubber-gasket gas seal. The lid provides easy access without misalignment of reflectors.

The reflectors form an integral part of the discharge chamber, obviating the need for Brewster angle NaCl windows with their problem of deliquescence. The mounting is extremely simple, consisting solely of a thick rubber gasket which acts both as a gas seal and as a spring reaction for the three adjusting screws (figure A2). It was feared, originally, that the shock wave from either the arc or the main discharge might misalign the reflectors, but this proved not to be so. Of course such misalignment would only affect the succeeding pulse, the original having passed before the shock hits the reflectors.

Three separate cylinders of He, CO_2 and N_2 with standard regulators to control the gas feed pressure feed gas through three flowmeters, each fitted with an adjustable needle valve (He at 0.5-9 l min^{-1}, CO_2 at 0.4-4.6 l min^{-1}, N_2 at 0.5-5 l min^{-1}) into a mixing chamber and thence into the main discharge chamber. A supply of He is taken through a fourth flowmeter into a duct behind the multiple-pin electrodes of the arc preionization system, since it has been reported that running arcs in pure He is beneficial (A2). The nitrogen cylinder also supplies two pressurised trigger spark chambers through two controlled-leak pressure regulators. Spark gaps were set to about 1.5cm, and operational pressures were 12 - 18 psi above atmospheric.

Provision was made for bubbling the gas mixture through liquids such as triethylamine and acetone, thus introducing these vapours as trace additives. Despite reports (A2) that this was beneficial we have observed no significant improvement under our operating conditions.

(II) Optics

The reflectors in most use are (a) an uncoated Ge flat of 7.5cm diameter and 6mm thickness, having reflectivity 36% per face (total 72%); and (b) a Au-coated Cu-Zr concave mirror of diameter 7.5cm and radius of curvature 3m, having reflectivity 99%. Each face of the Ge flat reflects 36% of the incident radiation since the refractive index n of Ge is 4 at 10.6μm and $R = (n-1)^2/(n+1)^2$. With two sides the total reflectivity is 72%. Multiple reflections between the two faces

(giving a Fabry-Perot effect) are attenuated fairly rapidly, since Ge absorbs 0.7 to 1.0% mm^{-1}, but we have clear evidence from the mode pattern (see below) that they did occur.

Alignment was accomplished by first passing a He-Ne laser beam centrally down the cavity without any reflectors; two centrally-drilled perspex discs, which slotted onto the mirror adjustment screws, served to locate the central position. The perspex disc furthest from the He-Ne laser was replaced by the Cu-Zr concave mirror which was aligned to return the beam along the same path; the same procedure was followed for the output mirror, the remaining perspex alignment disc being replaced by the Ge flat which, as before, was aligned to return the beam collinearly from its outer face.

Exact mirror alignment was found to be non-critical. During operation, deliberate misalignment of the mirrors by as much as 10 milliradians out of parallel produced no substantial change in output. As the Ge output mirror has an inherent wedge of about 0.27mr which renders complicated alignment accuracy of better than this limit, the insensitivity of the performance to this parameter is something of an advantage.

The laser has in addition been operated with an unstable resonator in view of the advantages reported by Dyer et al (A3) for such a system - single transverse mode operation and beam divergence of only 0.2 mr. Conversion to this type of optics was simple. We replaced the Au-coated Cu-Zr reflector with one of radius of curvature 10m and we attached (using double-sided sticky tape) a 3.75cm diameter convex Au-coated reflector of radius of curvature 7.5m onto the 7.5cm Ge flat. When spaced by 1.25m this arrangement was confocal, the common focus lying 3.75m beyond the convex mirror. The beam is then expanded by a factor of 4/3 per pass. The radiation escapes from the annulus around the smaller mirror, but the far-field beam pattern, of course, is not annular (A4). This system would have operated better if the Ge flat had been anti-reflection coated. As it was, not only was the pulse expanded in area during growth (thus reducing the growth of power density) but just the reverse occurred for the portion of the signal reflected by the Ge etalon and the exceptionally strong power density then tended to damage the mirrors.

(III) Preionizing system

The gas between the main electrodes is preionized by vacuum ultraviolet radiation generated by two lines of arcs on either side of the main gap, separated by 28cm. The arcs strike between tungsten or copper pins which are glued into the ravine between two capillary glass tubes with earthed central conducting rods. 34 arcs with gaps of 3-4 mm were run in series on each side. The striking voltage was about 20kV, but usually a 0.5μF rapid discharge capacitor charged to 50kV supplied the arc current. From the ringing period of 6μs (measured by means of a pickup coil) one estimates 1.6μH for the circuit inductance, and the maximum current $V(C/L)^{\frac{1}{2}}$ then works out at 3000A.

About 600J was discharged through some 60 arcs which is ~10J per arc. Exactly how the radiation from such arcs preionizes the gas is not yet fully understood. The effective radiation may have wavelength as short as 1 nm in which case the temperature of the arc is the vital parameter. (See reference A1).

Other systems have also been tested. For example, the system used by Pearson and Lamberton (A5) was improved by putting the tungsten wire trigger electrode in the ravine between polarised glass capillary tubes as described above (see figure A3).

(IV) Circuitry

For a gap of 6cm it is necessary to apply across the main electrodes a voltage pulse of 100kV. In order to avoid breakdown and short circuiting to the arc lines which were only 7cm away from the edge of the main electrodes, we were forced to apply +50kV to one electrode and -50kV to the other. The circuit used is shown in figure A4. Spark gap S_0 is fired by a conventional trigatron system; a car spark plug screwed into a disc electrode with a small central hole provides a convenient trigger electrode, and can be fired by the voltage pulse from a car induction coil. Firing S_0 applies -50kV across the arc lines, and the preionization of the gas is sufficient to carry the -50kV pulse onto the main discharge circuit (heavily outlined in figure A4). A voltage pulse of 100kV appears across S_2, causing S_2 to break down. The UV from S_2 triggers S_1, which is in the same pressurised spark chamber. When both S_2 and S_1 break down, voltage pulses of +50kV and -50kV appear respectively on the main anode and cathode. The two 0.12μF low inductance capacitors then discharge.

All circuitry, including the three rapid discharge capacitors was enclosed in an oil bath of dimensions 50cm x 50cm x 45cm constructed from $\frac{1}{2}$" perspex. Care was taken to minimise the lengths of both arc and main discharge circuits, and 1" wide copper strip was used to minimise inductance.

Originally it was planned to trigger S_1 independently of S_0, a trigatron being built in for this purpose. The pulse which fires the S_1 trigatron is obtained from the arc discharge, with suitable delay; we used a pickup coil to trigger a thyratron which fed the primary of a car induction coil. This mode of operation is also effective.

(V) Performance

The brightness of the preionizing arcs makes it extremely difficult to monitor visually the uniformity of the main discharge, but with some practice one could tell, at least, if an arc had occurred. Several minutes of flushing with the laser gas mix was necessary before successful operation.

A photon drag detector with voltage responsivity 0.18mV kW^{-1} and sensitive area 4mm x 4mm gave oscillographs of the type shown in figure A5. Figure A5a shows the output of the photon drag detector at a distance

of 0.24m from the Ge window; the pulse appears superimposed on pickup. Figure A5b shows the output from the detector at 3m from the output window the pickup now having been eliminated. In each case the detector is plugged directly in o the oscilloscope amplifier, leads being avoided to reduce pickup.

The full-width half-intensit points of the pulse have a separation of about 0.1μs in all traces. A small amplitude peak of width 1.0μs was noted following the main 0.1μs peak, and is probably caused by the delayed resonance transfer of energy from N_2 molecules. In figure A5a the pulse height of 0.3V implies power of 1.7MW incident on the detector area of 4mm x 4mm, and since the beam area was known from independent measurements to be 20cm^2 close to the laser one infers an output power of 210MW. Since the pulse duration is 0.1μs the energy is 21J. This output was achieved by discharging 276J of electrical energy through 1.8 l of gas mix - the actual mix in this case being 5:2.6:2 of He:CO_2:N_2. Thus the efficiency was 7.6% and the energy discharged per unit volume was 153 J l^{-1}.

The laser has also been operated with 0.25μF (instead of 0.12μF) capacitors without any limitation from arcing. We have not determined the maximum energy which can be discharged through unit volume of gas but probably it is in excess of 300 J l^{-1}

The area of the output beam can be determined by lateral displacement of the photon drag detector. However the simplest procedure was to interpose an exposed polaroid positive near the output window. A record of the beam pattern is burnt onto the film as shown in figure A6. The interference pattern visible on this record (and indeed all records) must be attributed to a slight wedge in the Ge output window, since the pattern rotates if the window is rotated. The fringes are spaced by 0.65cm so that half a wavelength change in thickness of the etalon per 0.65cm gives a wedge of 0.27 mr. By comparison of such prints taken close to the Ge output window and at 60cm range a beam divergence of 9mr was estimated. This is confirmed by the imprint produced at the focus of a mirror of focal length 1.5m (figure A7). The 1.5cm size of this imprint implies a beam divergence of 10mr.

In general air-breakdown provides a ready monitor of the output from the laser. Double air-breakdown could be achieved at 10cm and 24cm in front of a concave mirror which intercepts the beam (figure A8). A power of 250MW (25J in 0.1μs) will focus down to 10^{-2} cm^2 using a 10cm focal length mirror since the beam divergence is 10mr. This provides power density of 2.5×10^{10} W cm^{-2}, well above the threshold for breakdown, which is 10^9 W cm^{-2} (A6).

Section A2. CW CO_2 Laser

(I) Mechanical design features (see figure A9)

A discharge at gas pressure 14 - 16 torr is run inside a silica tube of length 1m and diameter 1cm. Two short copper T-sections serve both as gas inlet/outlet and as electrodes. The join between the silica tube and a copper T-section is made simply by inserting each halfway into a rubber bung: the system is supported by wedging the bung into a $1\frac{1}{2}$" i.d. perspex tube which is fixed to the base, and which also serves as a water cooling jacket. At the outside ends, each copper T-section is joined by a rubber bung to metal bellows, supported with respect to the base by an insulating perspex mount. The reflector mount plates are attached to the bellows, being pulled by springs onto three adjustment screws fixed to a heavy aluminium support structure which is kinematically mounted on runners for length adjustment. The plates with the runners are insulated from the aluminium base by $\frac{1}{2}$" perspex, since one end (including bellows and reflector) floats at ~12kV with respect to earth. A perspex housing shields the operator from this potential. Water cooling is provided for the Ge reflector.

(II) Gas supply

A cylinder of premixed gas (9:1:2 $He:CO_2:N_2$) with standard pressure regulator provides a flow of gas via a fine control needle valve and a flowmeter to the discharge tube. A pressure of 14 - 16 torr is maintained inside the discharge tube by an ordinary rotary vacuum pump, an offshoot leading to a pressure gauge between two isolating valves.

The laser was operated with a gas flow of 250 discharge volume changes per minute - that is 24 l min^{-1} at operating pressure or 0.8 l min^{-1} at STP. The pump has a maximum displacement of 85 l min^{-1}.

(III) Optics

The optical cavity has a length of 1.47m. The reflectors are (a) a Ge flat of diameter 3.75cm, antireflection coated on the outside and 85% reflection coated on the inside; (b) a Au-coated Cu-Ni concave reflector of radius of curvature 20m and reflectivity 98.8%.

Due to a wedge of 2.8mr on the Ge flat it was necessary to adopt a slightly more complex alignment procedure than was required for the TEA laser. Our reference He-Ne beam first was directed through the open end of the laser tube onto the inside surface of the Ge flat at the far end. The orientation of the flat was adjusted so as to return the beam along the same path. On the reverse side of the metal mirror a secondary flat mirror was mounted on spring-loaded adjustment screws; using two He-Ne beams the axis of the primary mirror was adjusted to be normal to the plane of the secondary mirror. Then by reflecting the reference beam along the same path from the outside secondary mirror one ensures that the inside cavity mirror is approximately aligned. Final adjustment for optimum output is carried out with the laser running.

(IV) Circuitry

A 25kV, 100mA DC power supply with one side earthed and positive polarity feeds the discharge through a 200kΩ ballast resistor (figure A10). The metal mirror was at the anode side because water cooling to the Ge reflector meant that it could not be raised to high potential.

Under normal and correct operating conditions the voltage across the tube is 12kV and the current drawn is 20mA. Thus 240W is dissipated in the discharge, which implies ~50W output at 20% efficiency.

(V) Performance

For reasons that are not yet clear (but will be investigated when time permits) the CW laser gives only about 5W output. Some 50W can be achieved from a discharge of length 1m and diameter 1cm. The intensity of the beam has 5% modulation at 100Hz (figure C8c). The beam diameter as measured with an Optical Engineering thermal image plate (phosphorescence quenching) is about 3mm. The beam divergence is about 1mr.

PART A REFERENCES

A1 P.F.Browne and P.M.Webber, A Compact 50J CO_2 TEA Laser with VUV Preionization and the Discharge Mechanism, Appl. Phys. Lett. 28, 662 (1976)

A2 H.J.Seguin, J.Tulip and D.C.McKen, Ultraviolet Photoionization in TEA Lasers, IEEE J. Quantum Electron., QE-10, 311 (1974)

A3 P.E.Dyer, D.J.James and S.A.Ramsden, Single Transverse Mode Operation of a Pulsed Volume Excited Atmospheric Pressure CO_2 Laser Using an Unstable Resonator, Optics Communications 5, 236 (1972)

A4 J.M.Burch, private communication (1961), see also A.E.Siegman, Unstable Optical Resonators, Proc. IEEE 53, 277 (1965)

A5 P.R.Pearson and H.M.Lamberton, Atmospheric Pressure CO_2 Lasers Giving High Output Energy per Unit Volume, IEEE J. Quantum Electron. QE-8, 145 (1972)

A6 D.C.Smith, Gas-Breakdown Dependence on Beam Size and Pulse Duration with 10.6μm Wavelength Radiation, Appl. Phys. Lett. 19, 405 (1971)

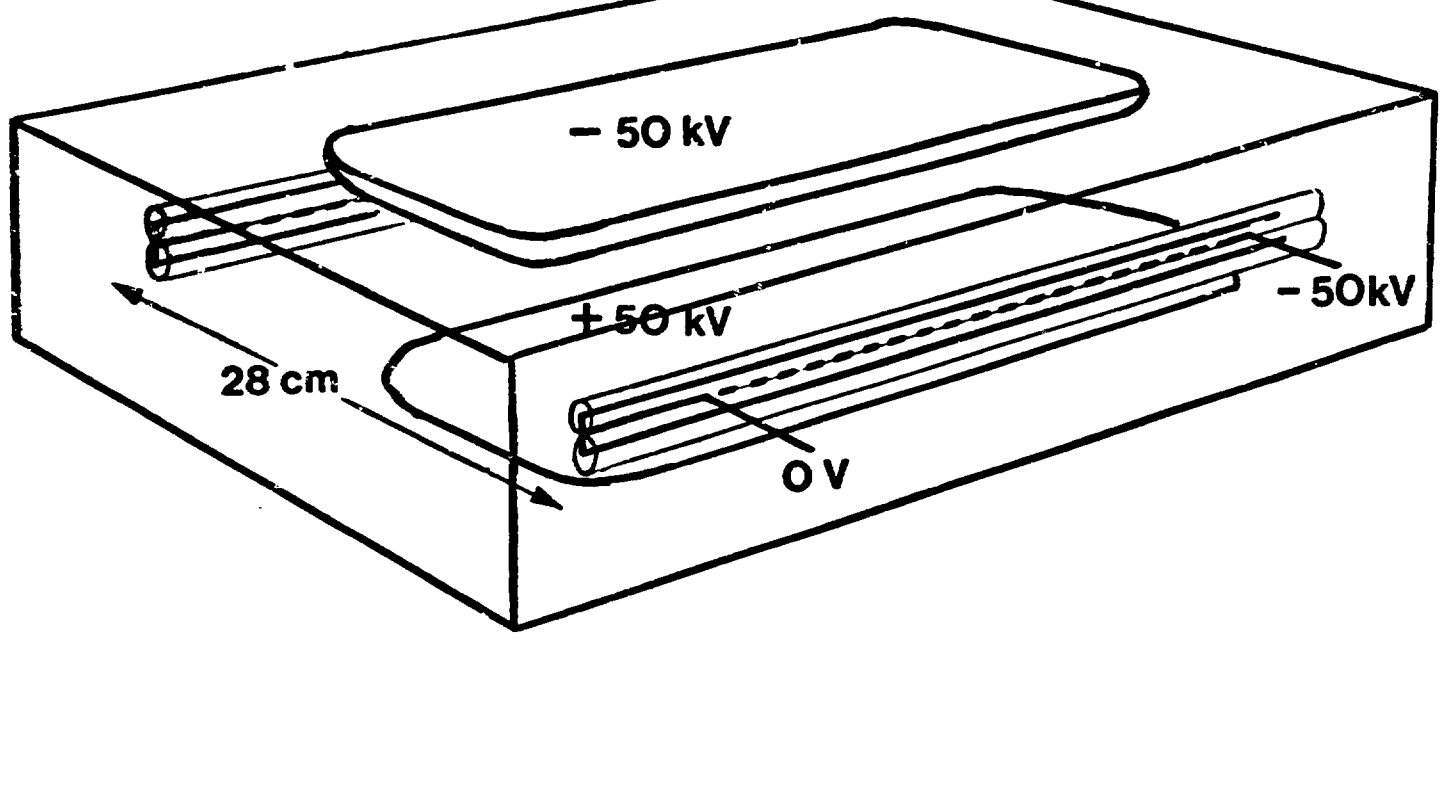

Figure A1: Solid aluminium electrodes machined with a Bruce profile and with base dimensions 15cm x 50cm are supported from top and bottom of a perspex box of dimensions 105cm x 35cm x 25cm. On either side and 28cm apart are two lines of 34 arc gaps each ~4mm. The arcs occur between tungsten or copper pins in the ravine between two glass capillary tubes with earthed central conductors. The main interelectrode gap is 6cm.

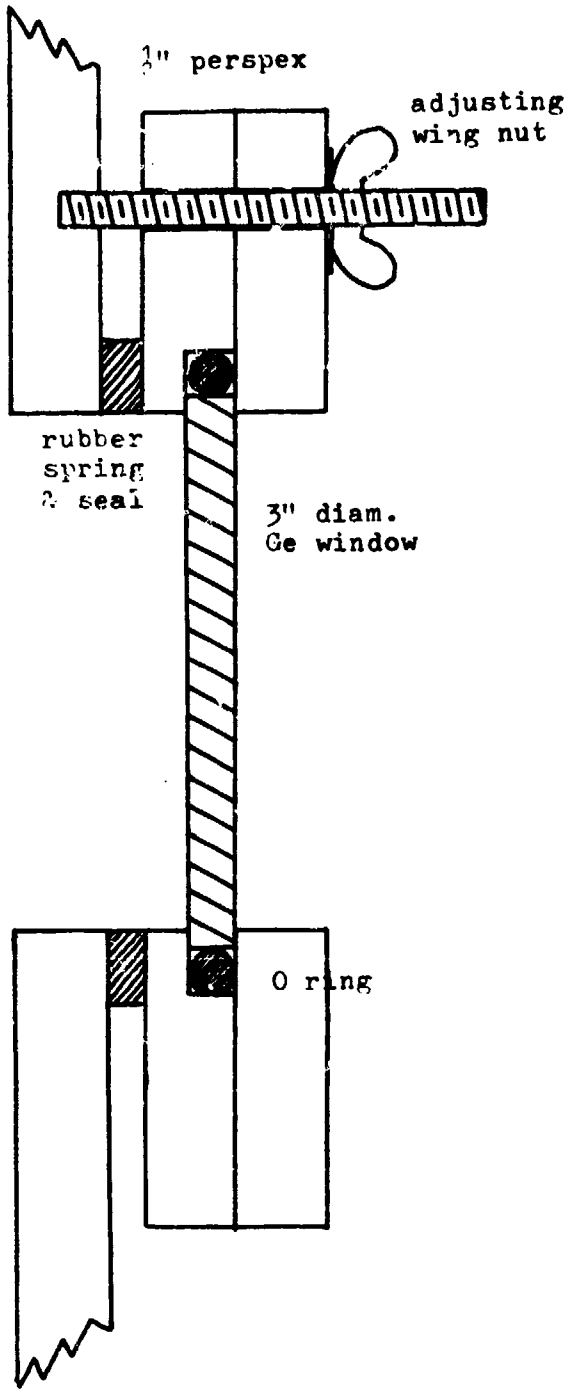

Figure A2: Mounting for reflectors showing thick rubber gasket which is both a gas seal and a spring load for the three adjustment screws.

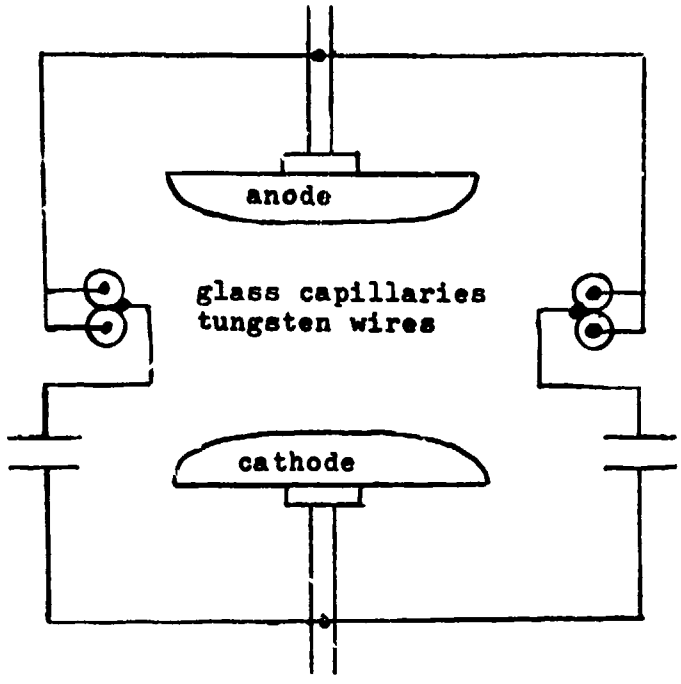

Figure A3: The Lamberton–Pearson system of preionization by a corona discharge from two fine tungsten wires to the main anode is shown modified by positioning the tungsten wires in the ravine between polarised capillary glass tubes. The diagram (end view) illustrates the electrical connections to the tungsten wires and to the central conductors in the glass tubes.

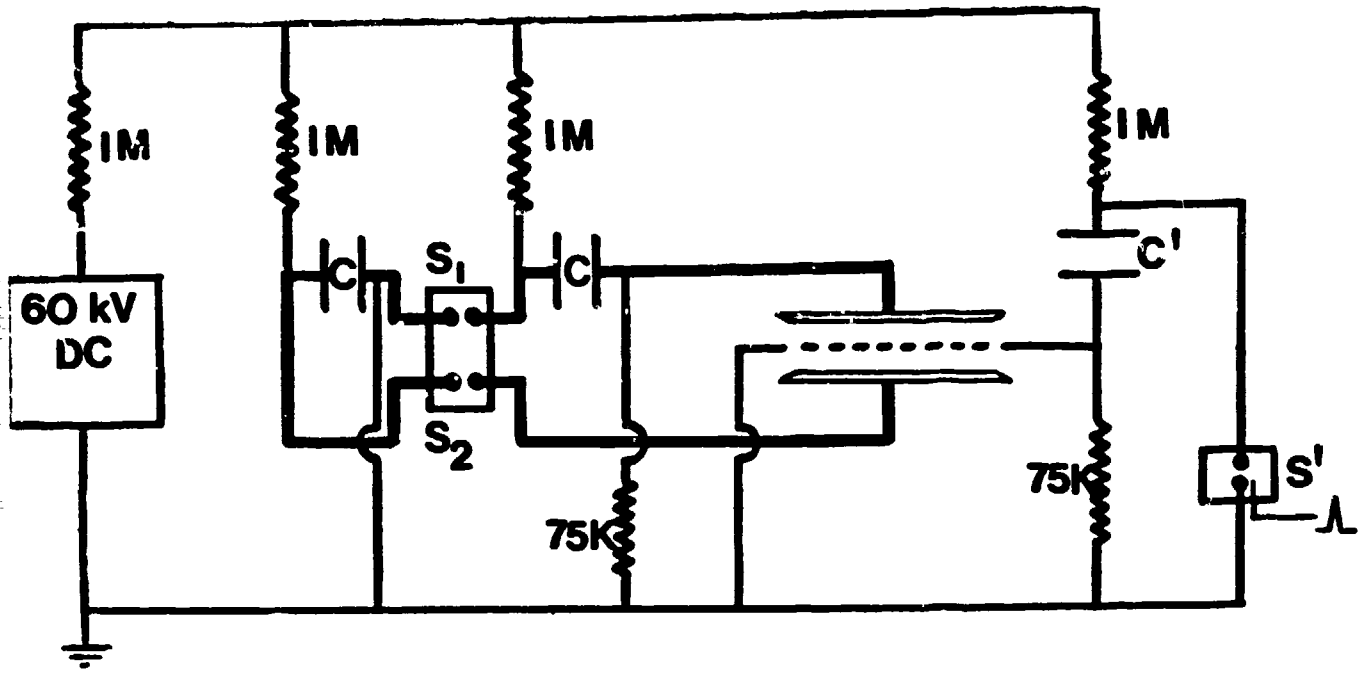

Figure A4: Circuit for simultaneous application of +50kV to the anode and -50kV to the cathode. The low inductance main discharge circuit is heavily lined. Spark gaps S_1 and S_2 are in the same chamber of pressurised nitrogen. The arc circuit is also shown.

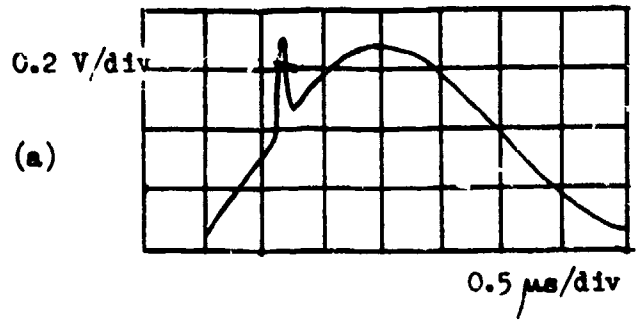

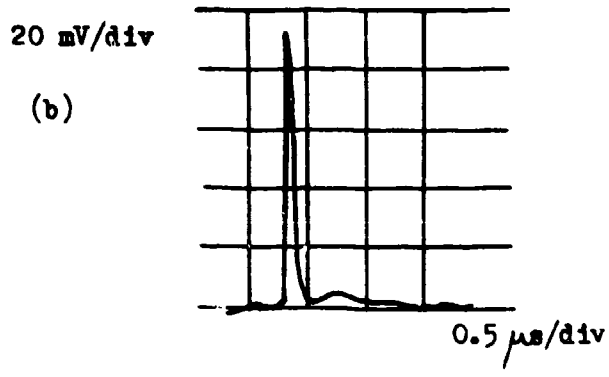

Figure A5

Tracings of oscillographs of the output from a photon drag detector of voltage responsivity 0.18 mv/kW and sensitive area 4 mm x 4 mm (a)24 cm from the output Ge window of the CO_2 TEA laser and (b) 3 m from the output window. The signal in (a) is superimposed on electrical pick-up. In (a) the beam area was 20 cm^2 implying peak pulse power of 210 MW and pulse energy 21J.

Figure A6: Imprint of TEA laser beam on polaroid film (actual size). Beam area = 20cm^2. Fringes are caused by a 0.27mr wedge on the uncoated Ge output window (reflectivity 36% per face).

Figure A7: Imprint of TEA laser beam at focus of a mirror of focal length 1.5 m. The 1.5 cm diameter of the imprint implies 10 mradian beam divergence.

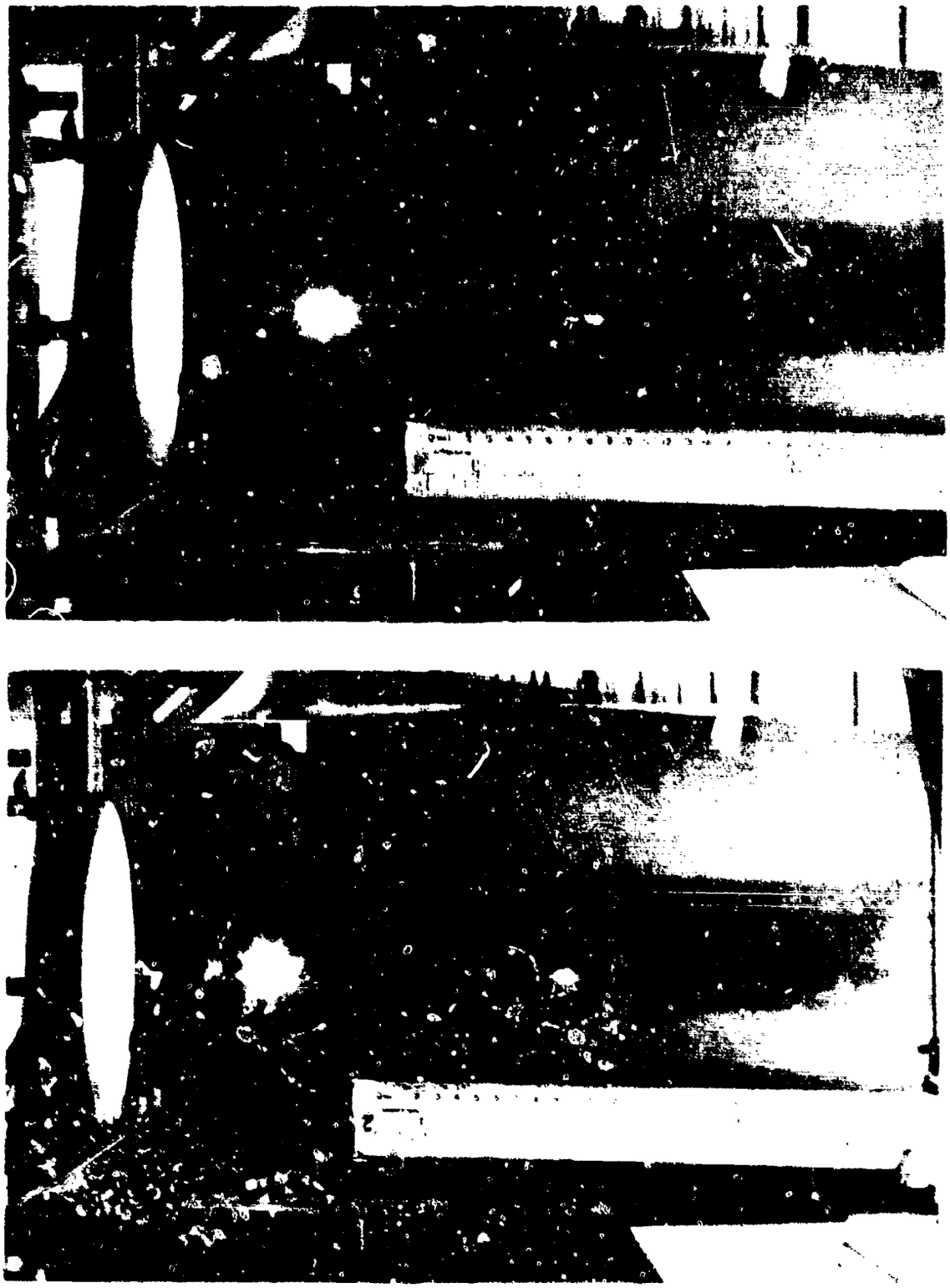

Figure A8: Double air-breakdown at approximately 10 cm and 24 cm in front of mirror intercepting the beam. Note luminous blow-off from Ge output window on right of lower photo. Photos are time-exposures with light from arcs and discharge shielded from the camera.

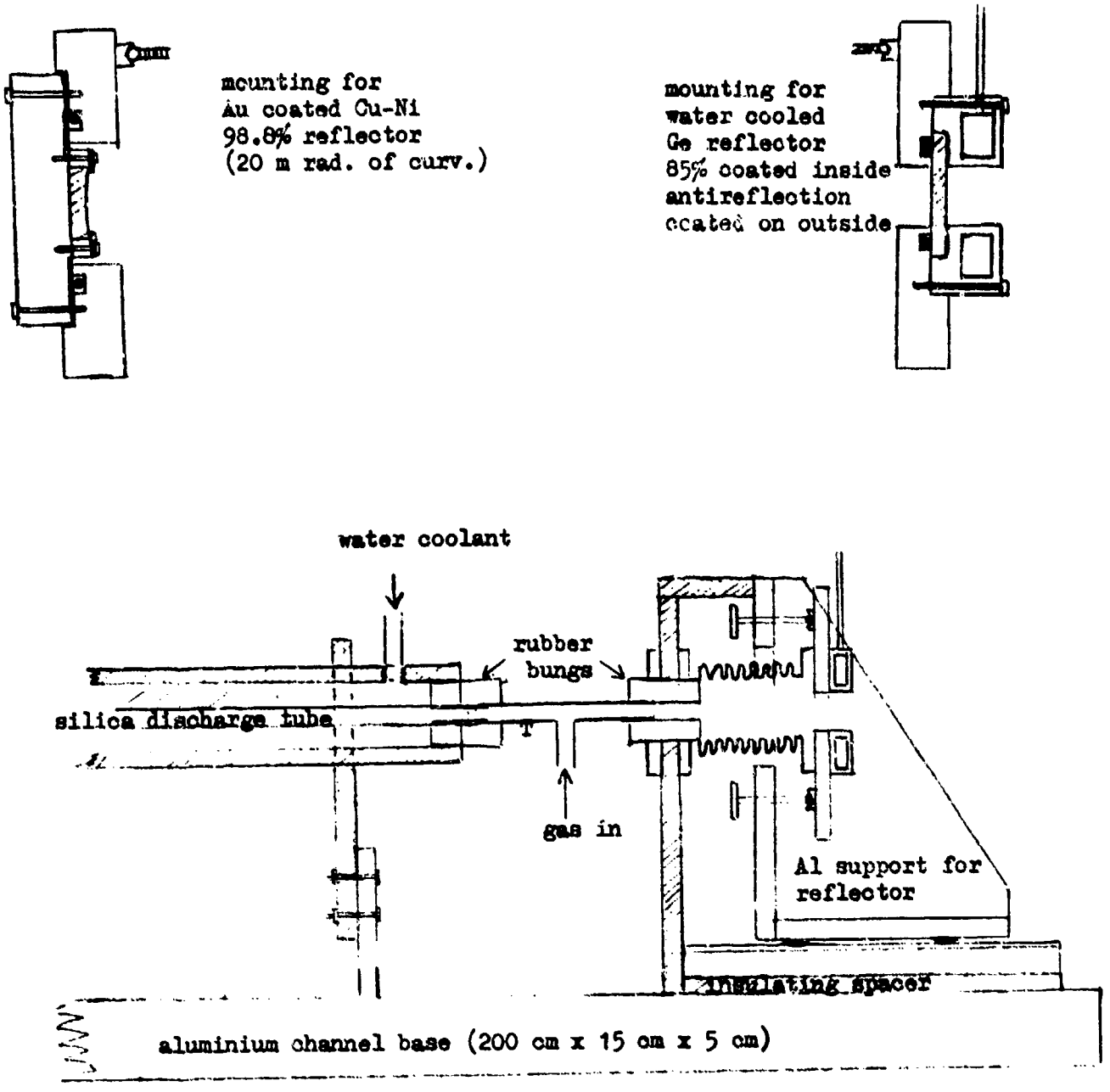

Figure A9:

Mechanical design features of simple diffusion cooled cw CO_2 laser. Perspex material shown by hatching. The diagram shows only one side, the other being similar. A magnified section of the reflector mountings is shown above. Scale: $\frac{1}{4}$ actual size.

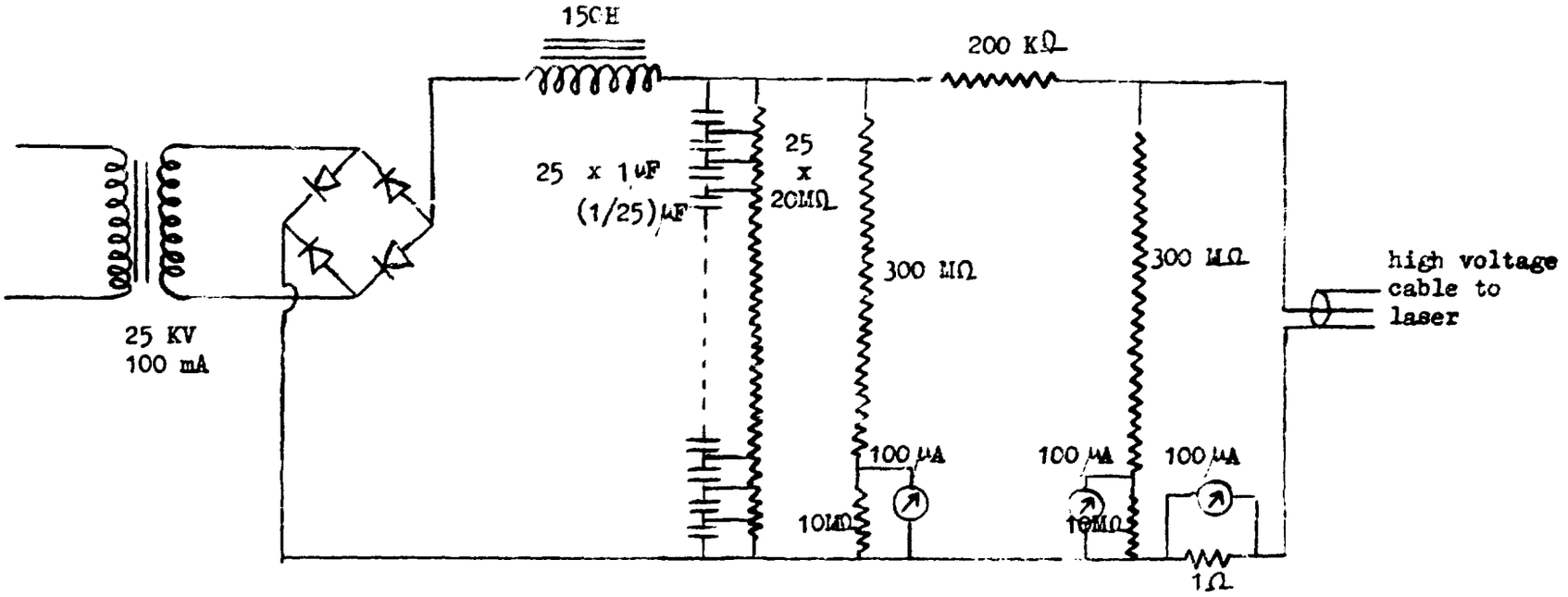

Figure A10: 25KV 100 mA power supply plus current and voltage monitoring instrumentation. All circuitry is immersed in an oil bath.

PART B: CLOUD PRODUCTION

Section B1. Cloud Chamber Construction

A cloud chamber of volume 300 l has been constructed from commercially available modular glass pipeline. A single unit, of diameter 0.5m and length 1.5m, with ground end faces, is sealed by two galvanised steel end flanges. These are bolted to collars supported by tapers on the outside diameter of the glass pipeline (figures B1 and B2). The chamber can be pressurised up to 1.5 atm. Sudden venting to the atmosphere through a 1 inch solenoidal valve produces a temperature drop uniformly throughout the chamber. This results in supersaturations of over 600% if required. Condensation then proceeds on whatever nuclei may be present.

How much water will be condensed out per unit volume of cloud is determined by the expansion ratio, the initial temperature and the initial relative humidity, or equivalently the expansion ratio and the observed temperature fall (see below). The concentration of condensation nuclei (which can be, at least crudely, controlled) determines the number density of droplets. The size of the droplets is then fixed, and the cloud will be monodisperse if all condensation nuclei are equally effective. Provision is made for feeding the input gas through a discharge in order to introduce ions as condensation nuclei.

The steel end flanges have central ports of diameter 7.5cm which are sealed by spring-loaded caps when the chamber is being pressurised. (These were constructed from motorcycle tank filler caps). Once the cloud has formed, the ports are quickly opened, and an unobstructed passage is available through the homogeneous and well-defined cloud. For attenuation and other measurements it is a great advantage to eliminate completely windows on which condensation can occur; the choice of windows at 10.6μm wavelength is very restricted in any case. Thus, there is considerable advantage in arranging that the final pressure after adiabatic expansion, is atmospheric.

The gas picks up water vapour on its way into the chamber by being bubbled through a water tank. Alternatively one may wait for saturation to occur due to liquid water present in the bottom of the chamber.

Section B2. Measurement of Water Condensed

Before condensation occurs the adiabatic expansion from pressure p_1 to pressure p_2 implies a temperature fall from T_1 to T_2 where

$$\frac{T_2}{T_1} = \frac{p_2}{p_1}^{(\gamma-1)/\gamma}$$

γ being the ratio of principal specific heat capacities (1.4 for air). If the gas is supersaturated at the lower temperature T_2 condensation will occur on whatever nuclei are effective in initiating the process. The latent heat liberated during condensation increases the temperature

of the gas to T_2', where

$$\rho_a c_v (T_2' - T_2) = L \Delta\rho \qquad (B2)$$

Here ρ_a is the mass density of air, c_v is the specific heat capacity of air at constant volume, L is the latent heat of vaporisation, and $\Delta\rho$ is the mass of water condensed per unit volume of air. These constants have the values

$$\begin{aligned} \rho_a &= 1.293 \times 10^{-3} \text{ g cm}^{-3} \\ c_v &= 0.718 \text{ J g}^{-1} \text{ K}^{-1} \\ L &= 2.45 \times 10^{3} \text{ J g}^{-1} \end{aligned} \qquad (B3)$$

Thus

$$\Delta\rho = 0.38(T_2' - T_2) = 0.38(\Delta T_0 - \Delta T) \qquad (B4)$$

where $T_2' - T_2$ is in degrees Kelvin and $\Delta\rho$ is in g m^{-3}. In order to determine $\Delta\rho$ one calculates first $T_1 - T_2$ $(=\Delta T_0)$ from the initial excess pressure Δp (figure B4 shows how ΔT_0 varies with Δp), and then one substitutes into equation (B4) the measured value of ΔT. Typically $\Delta\rho \sim 4$ g m^{-3} for our clouds (see figure C5).

With the help of the curve of saturated water vapour density as a function of temperature $\rho_s(T)$ given in figure B3, we can then proceed to infer the initial relative humidity. During compression of the gas in a time of two or three minutes heating of about 4K was observed (figure B6). However, it is more appropriate to consider the relative humidity with respect to the saturated water vapour content for room temperature $\rho(T_{room})$ minus that for the final temperature $\rho(T_2)$. Typically relative humidities range from 50% - 85%.

The initial excess pressure Δp is measured with an aneroid pressure gauge. The parameters T_{room}, T_1, T_2' are measured with a copper—constantan thermocouple with the cold junction at ice temperature. Figure B5 is the calibration curve. Usually the output of the thermocouple ($\sim$1mV) was fed into a Hewlett-Packard 7100B chart recorder with integral amplifier. Figure B6 shows typical temperature vs. time curves for expansion from different excess pressures. Of course the temperature fall is less the higher the relative humidity, but for approximately the same relative humidity we have observed 7.4K, 11.2K and 13.5K for Δp = 3 psi, 5 psi and 6 psi respectively (1atm = 14.7 psi).

Section B3. Cloud Nucleation

Aerosols normally present in laboratory air in concentrations of order 10^5 particles cm^{-3} may be used to nucleate a cloud. We have found, however, that much denser clouds (visually) can be produced by ion nucleation; one feeds the ingoing gas through a discharge (typically 40mA, 2.5kV), and then expands from 6 psi above atmospheric pressure. This gives 586% supersaturation for 100% initial relative humidity and 410% supersaturation for 70 % initial relative humidity.

With regard to ion concentrations one notes that the rate of production of ions naturally (due to cosmic rays, radioactivity etc.) is of order

10 cm^{-3} s^{-1} and the rate of recombination of small ions is $\alpha n_+ n_-$ where $\alpha = 1.6 \times 10^{-5}$ cm^3 s^{-1}; hence $n_+ = n_- \sim 2500$ cm^{-3} for equilibrium. However the density of large ions in cities may be of order 30 000 cm^{-3}. If, in our discharge, we produce n_0 ion pairs cm^{-3}, then after time t we shall have n where

$$\frac{1}{n} - \frac{1}{n_0} = \alpha t \qquad (85)$$

After say 3 minutes (our filling time) one might expect to be left with only 3000 ions cm^{-3} according to (85), but the recombination rate for large ions is slower and we may in fact approach 3×10^5 cm^{-3}.

Cigarette smoke and magnesium oxide smoke have proved effective in nucleating clouds. A simple way to introduce smoke is to jam the "mouth" end of a lighted cigarette into a hole which is cut in the polythene gas input tube. A crude venturi is thus formed which tends to draw the smoke into the gas flow.

Further work on the control of droplet concentration by specifying the concentration of condensation nuclei is required (B1).

Section B4. Drop Sizes

Frequently clouds have exhibited a well-defined ceiling which descends slowly under gravity. The velocity v of descent is given by Stokes's law

$$v = 2 g a^2 d / 9\eta \qquad (86)$$

where a is the drop radius, d is the mass density of water, g is the acceleration due to gravity and η is the viscosity of air ($\eta = 1.8 \times 10^{-4}$ dyne cm^{-2} s). Thus a well-defined ceiling, uniformly descending, suggests a monodisperse cloud. Figure B7 is a plot of v as a function of a on log-log graph paper. Clearly a drop of radius 1.5μm will descend with velocity 0.027 cm s^{-1} and hence will require 1000s to cover 27cm (about the radius of the cloud chamber) - that is, a cloud lifetime of about 16 minutes. For a = 3μm this lifetime will be only 4 minutes.

That clouds formed by adiabatic expansion should be monodisperse is to be expected. Thus the radius of a drop grows in accordance with the relation (B2)

$$a \frac{da}{dt} = D(\rho_\infty - \rho_a) \qquad (87)$$

where D is the diffusion coefficient for water vapour in air (D = 0.239 cm^2 s^{-1}) and ρ_∞, ρ_a are water vapour densities for, respectively, infinite distance from the drop and the surface of the drop. Since $da/dt \propto 1/a$ there will be a tendency toward a monodisperse distribution even if the condensation nuclei are heterogeneous.

Direct confirmation that clouds produced by adiabatic expansion with ion nucleation are monodisperse has been obtained by Cole et al (B3). Using a piston-driven expansion chamber in which the same gas can be

recycled they monitored all over the 100ms period of the expansion by identifying the oscillations in the Mie efficiency factor $K(\alpha)$, where $\alpha = ak$ and $k = 2\pi/\lambda$ with λ the wavelength. As a, and hence α, varies, $K(\alpha)$ undergoes oscillations (figure B10) and the identification of a peak immediately gives the drop radius at that time. Since $K(\alpha)$ is a known function the measurement of light beam attenuation coefficient, $K\pi a^2 N$, then gives the concentration of droplets. Unless these clouds were monodisperse the oscillations of $K(\alpha)$ could not be resolved. The observation of Tyndall spectra also indicated monodisperse clouds. Typically they found $a = 1.05\mu m$ and $N = 1.17 \times 10^6$ cm^{-3}. They concluded that the half-width of the distribution was less than 20% of the most probable size.

Assuming, then, that our clouds are at least approximately monodisperse a quick method of measuring the most probable drop radius for a cloud whose water content $\Delta\rho$ is known is to record the attenuation of a $0.63\mu m$ beam from a He-Ne laser. For this beam the attenuation is due primarily to scattering and the cofficient is proportional to a^2 (rather than a^3 as for attenuation cefficient at $10.6\mu m$). In fact, we have

$$\gamma(0.63) = K\pi a^2 N = 3\Delta\rho/2d\bar{a} \qquad (B8)$$

Where we have taken $K = 2$ (a reasonable assumption since $k = 2\pi/\lambda \simeq 10$ and so $\alpha = ak \simeq 15$ for our clouds - see figure D2). Equation (B8) should be compared with (D46), valid for a natural size distribution. Writing $\gamma = 0.23\gamma^*$ where γ^* is the attenuation in dB m^{-1} we can express (B8) in the form

$$\bar{a} = 6.513 \times 10^{-4} \Delta\rho\ \gamma^* \qquad (B9)$$

where $\Delta\rho$ is in g m^{-3} and $\bar{a}$ is in μm. Typical values obtained for $\bar{a}$ for clouds whose $\Delta\rho$ is inferred from measurement of Δp and ΔT are recorded in figure C5.

A logarithmic amplifier (circuit shown in figure B7 and calibration graph in figure B8) gives 1V output for each 10dB change in input signal. Thus the output from this amplifier is proportional to the attenuation coefficient $\gamma(0.63)$ rather than the transmittance $I(o)/I(z)$. This permits several decades of transmittance to be recorded without change of scale. Typical chart recordings of $\gamma(0.63)$ are given in figures C1a, C2a and C3a.

The measurement of drop size distributions is a problem which has received wide consideration. The chief methods available are surveyed in appendix X2. For present purposes a real-time method which is instantaneous in operation has very great advantages.

A possibility worthy of further investigation would be to gate the descent of the drops. Then the different sizes will be dispersed in height at a particular time after opening the gate, and the drops moving through the $0.63\mu m$ beam on the axis of the chamber will have a radius which decreases monotonically with time. The chart recording of γ vs. time should then reveal oscillations due to the oscillating variation of $K(\alpha)$ with a (arising from interference between radiation transmitted through

the drop and radiation diffracted by the drop). Identification of the peaks then yields a value for a - essentially the method used by Cole et al (B3) except that we employ a logarithmic amplifier and a longer time scale.

Section B5. Cloud Lifetime

A cloud with $\bar{a} = 1.5\mu m$ should descend distance 25cm in a time of order 16 min according to Stokes's law. Frequently such clouds were observed to disappear in 3 - 4 minutes (contrast, for example, figures C1a or C2a with C3a or C10a; the clouds in C3a and C10a were eventually blown away). Presumably evaporation was determining the lifetime of these clouds. The final temperature, after adiabatic expansion, was below room temperature and temperature charts show that recovery to room temperature occurs in a matter of minutes. Whether the cloud then disappears will depend on whether the amount of water vapour initially present was above the saturation water vapour at room temperature - as can be achieved by preheating of the gas.

It is significant that a cloud such as that recorded in figure C10a should persist for as long as one hour probably because it was produced immediately after a steam cloud which had preheated the gas.

PART B REFERENCES

B1 N.A.Fuchs and A.G.Sutugin, Generation and Use of Monodisperse Aerosols, ed. C.N.Davies (Academic Press: New York) Ch.1

B2 B.J.Mason, Physics of Clouds (Clarendon Press, Oxford) 1971

B3 J.E.Cole III, R.A.Dobbins and H.Semerjian, Time-Resolved Measurement of Droplet Size and Concentration in Cloud Chambers, J. Appl. Meteor. 9, 684 (1970)

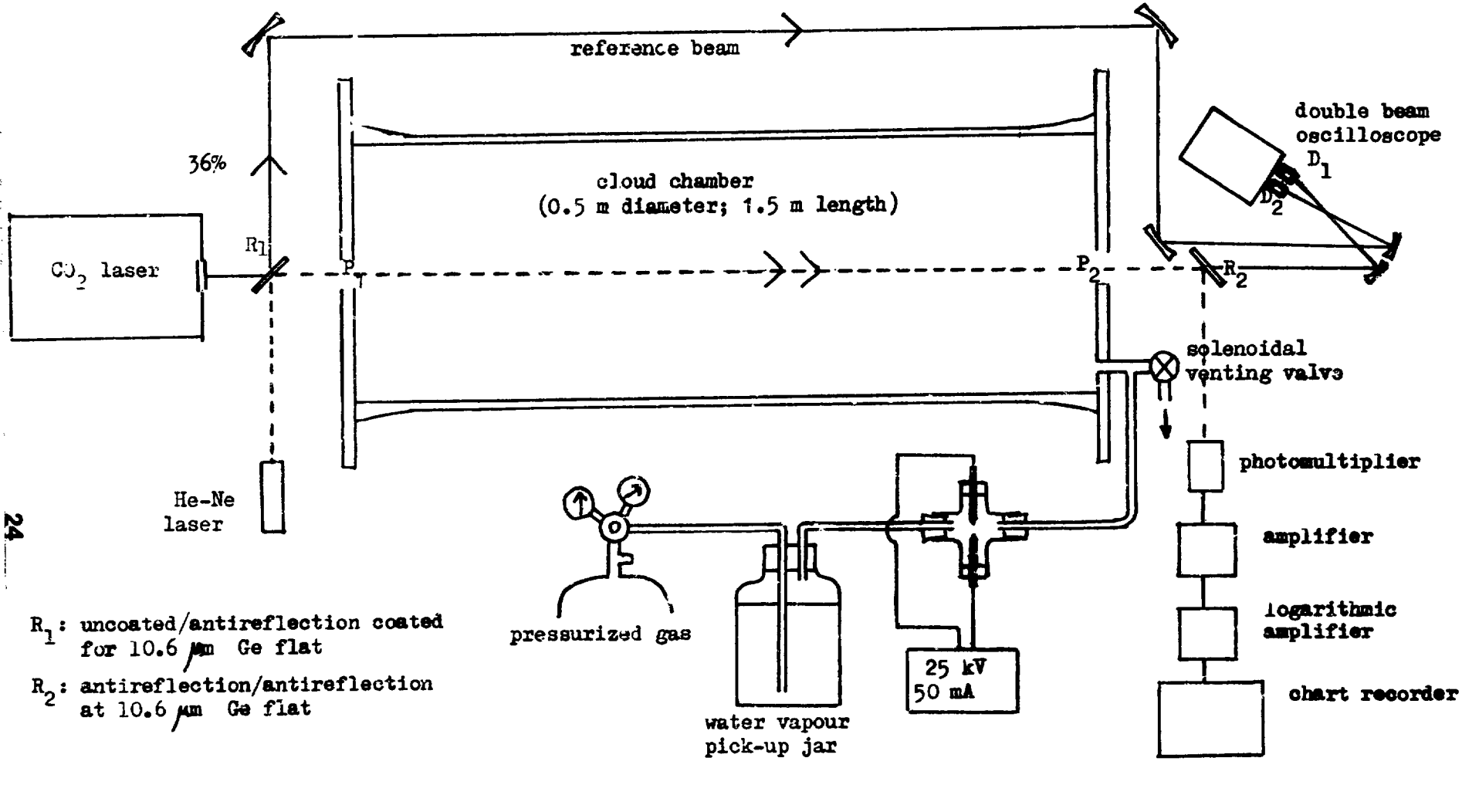

Figure B1: Cloud chamber of volume 300 litre constructed from QVF glass unit with galvanized metal end plates. Quick-release pressure caps close the ports P_1 and P_2 during pressurization. Water vapour and ions are added to gas before entry. Detectors D_1 and D_2 are of the photon drag type for high power pulses of 10.6 μm radiation. A coincident He-Ne beam monitors cloud clearing.

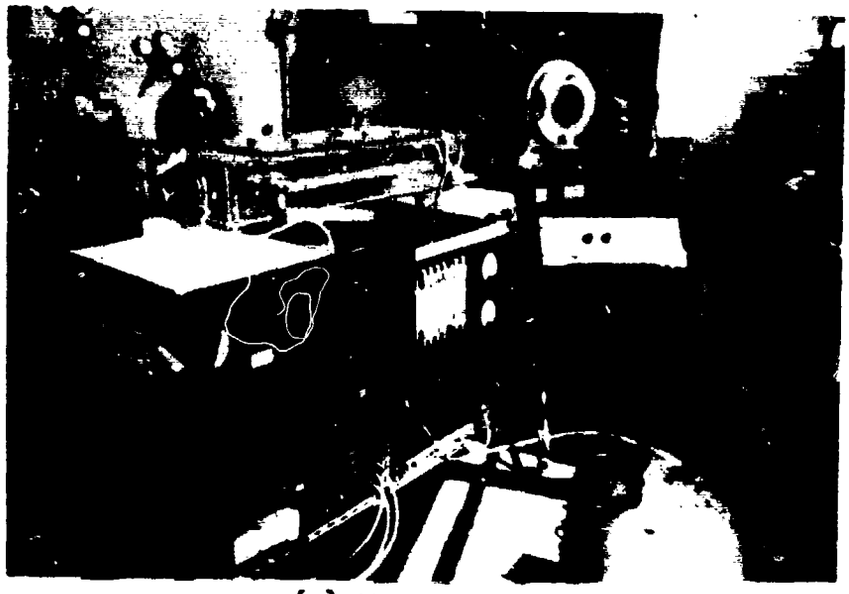

(a) the TEA laser

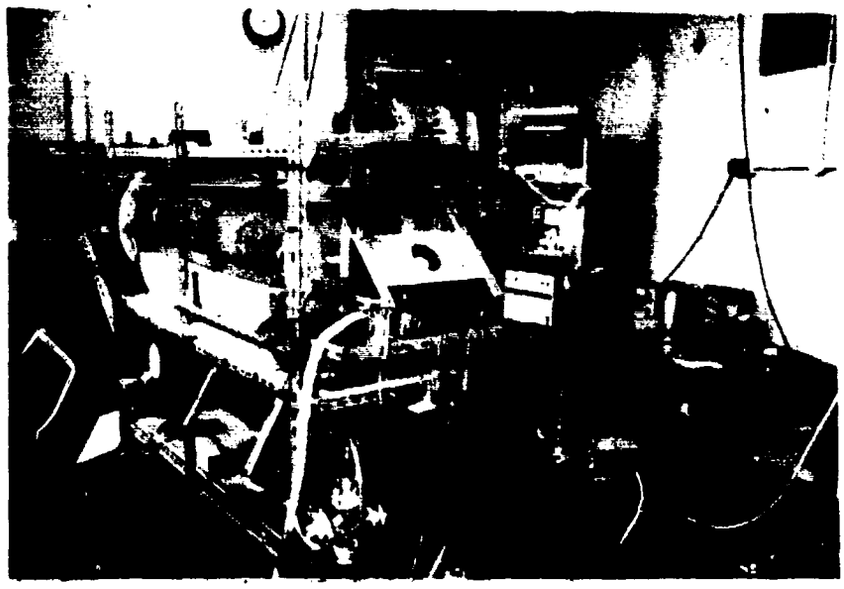

(b) the cloud chamber

Figure B2: (a) the TEA laser
(b) the cloud chamber

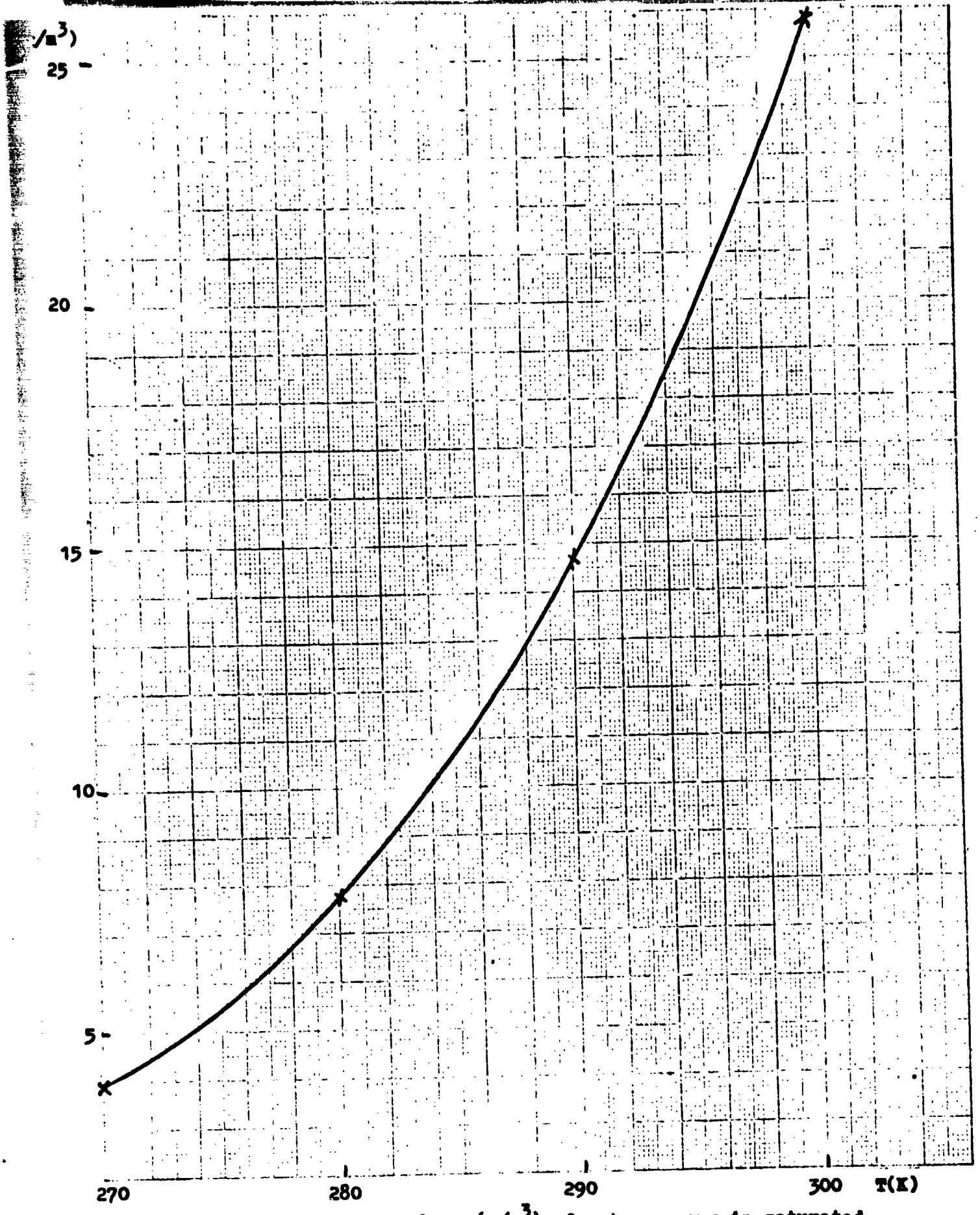

Figure B3: Mass per unit volume (g/m^3) of water vapour in saturated air as a function of temperature (T)

T_1 = 300 K (27 C)

Δp (psi)	$\frac{P_1}{P_2}$	$\frac{V_2}{V_1}$	ΔT (dry)	ΔT (sat.)	$\Delta \rho$ (g/m^3)
1.0	1.07	1.05	5.7	1.3	1.8
2.0	1.14	1.10	10.7	2.6	3.4
3.0	1.20	1.14	15.5	3.6	4.5
4.0	1.27	1.19	19.9	4.6	5.8
5.0	1.34	1.23	24.1	5.7	7.0
6.0	1.41	1.28	28.0	6.7	8.1
7.0	1.48	1.32	31.6	7.8	9.1
8.0	1.54	1.36	35.0	8.6	15.7

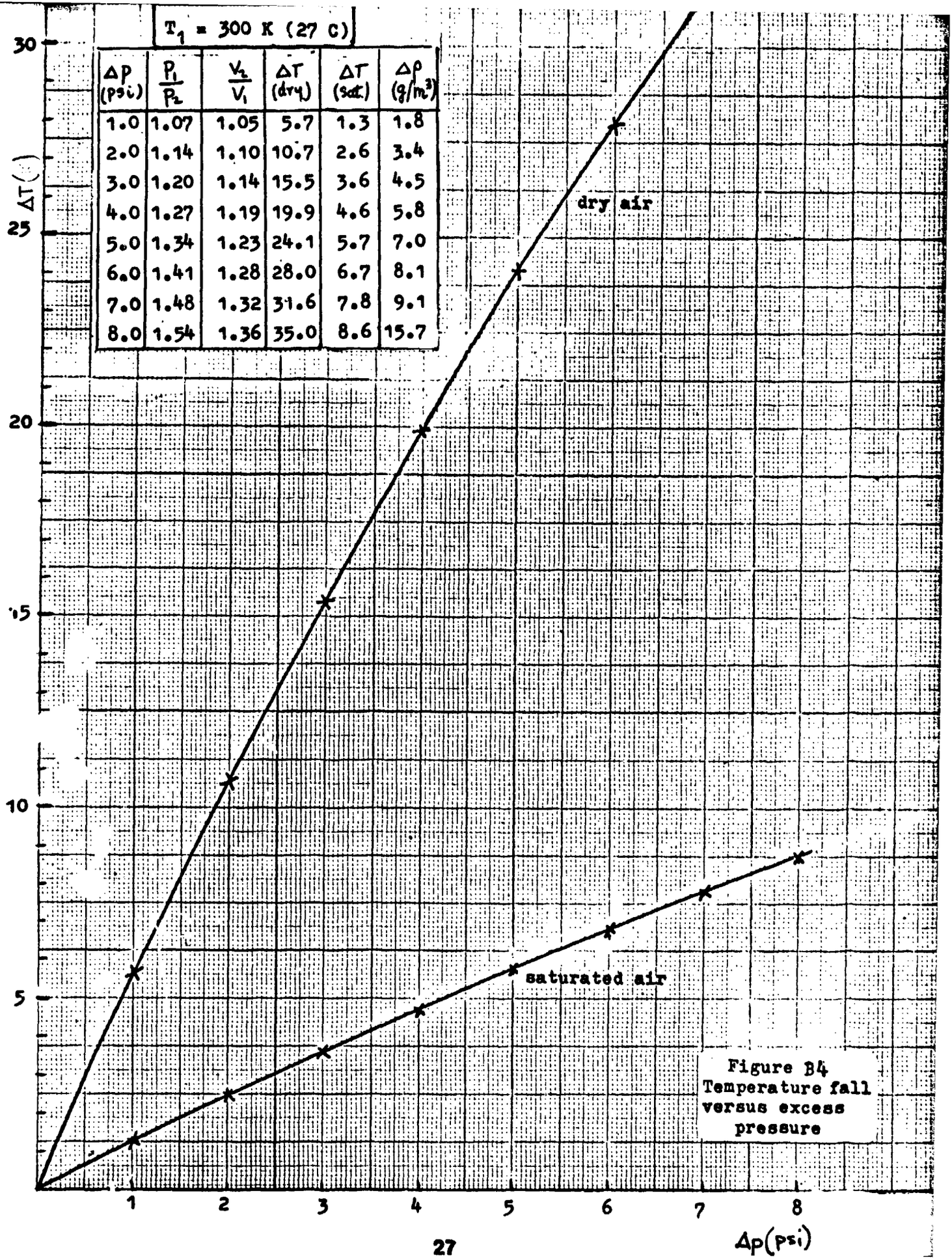

Figure B4
Temperature fall versus excess pressure

Figure B5: Calibration curve for thermocouple

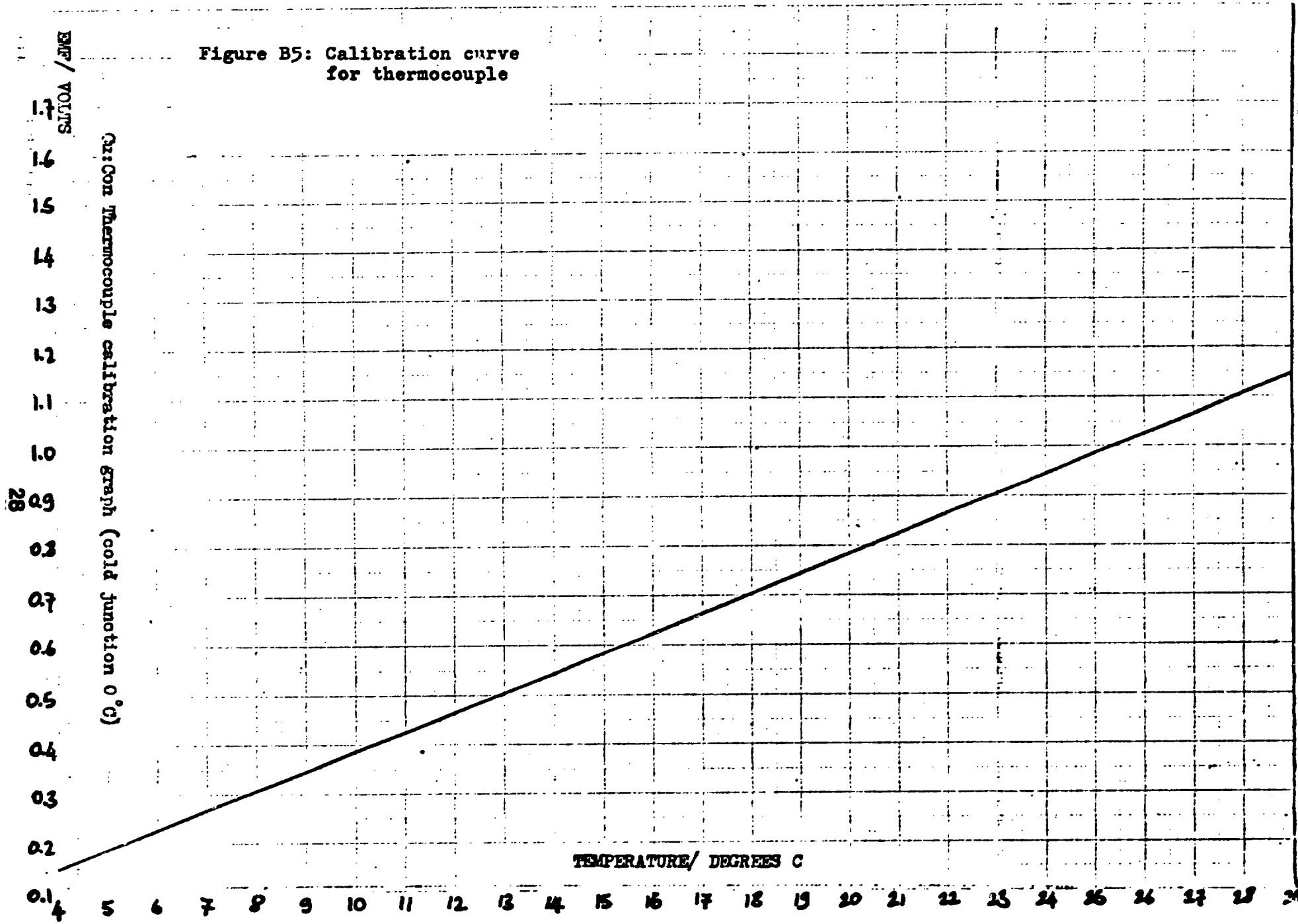

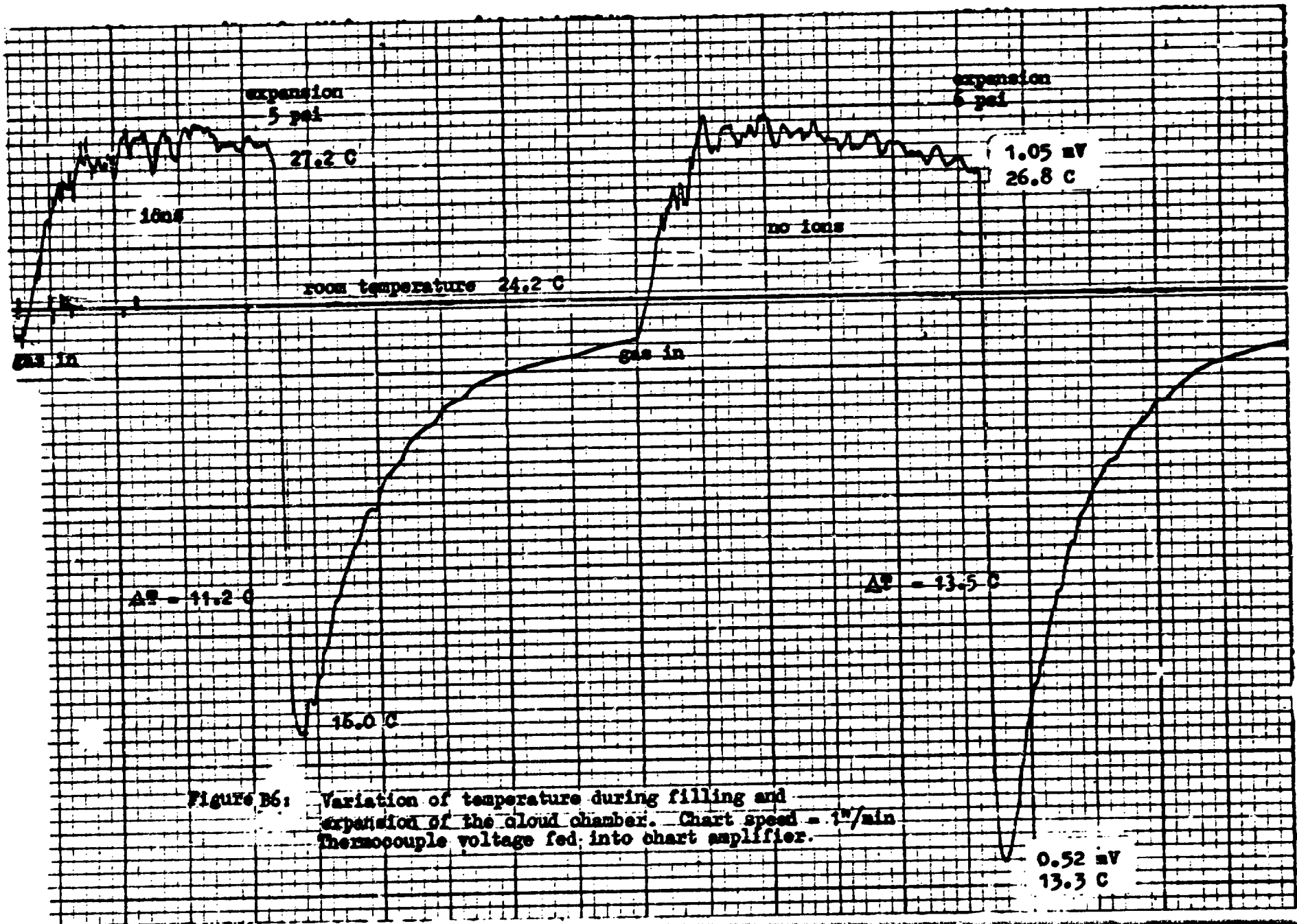

Figure B6: Variation of temperature during filling and expansion of the cloud chamber. Chart speed = 1"/min Thermocouple voltage fed into chart amplifier.

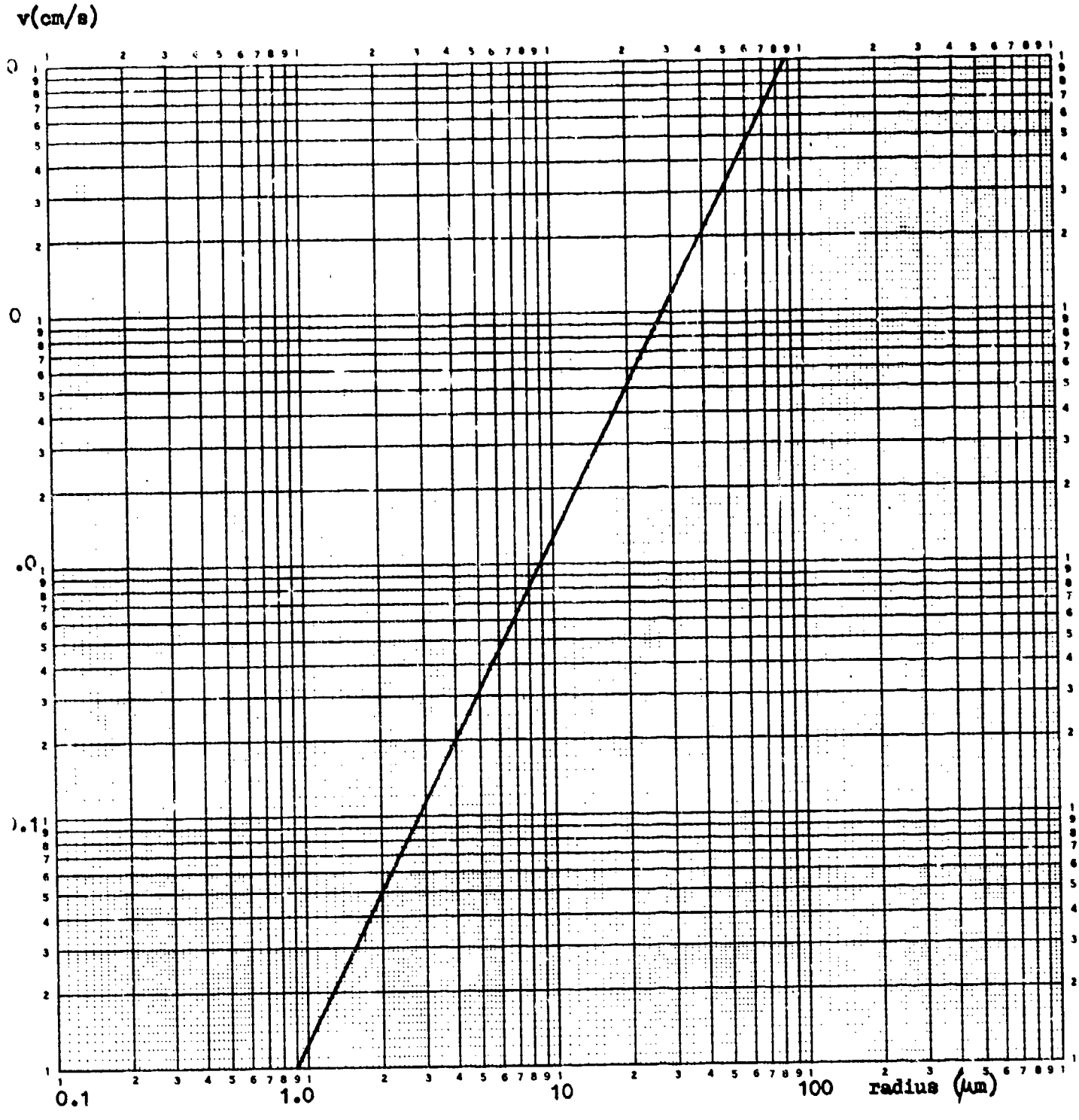

Figure B7: Velocity of descent of drops as a function of radius according to Stokes's law.

Figure 8:
Amplification, smoothing, and logarithmic amplification of photomultiplier signal

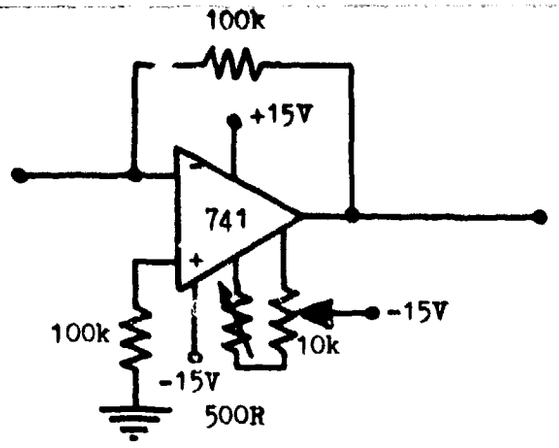

Current to voltage converter for photomultiplier tube

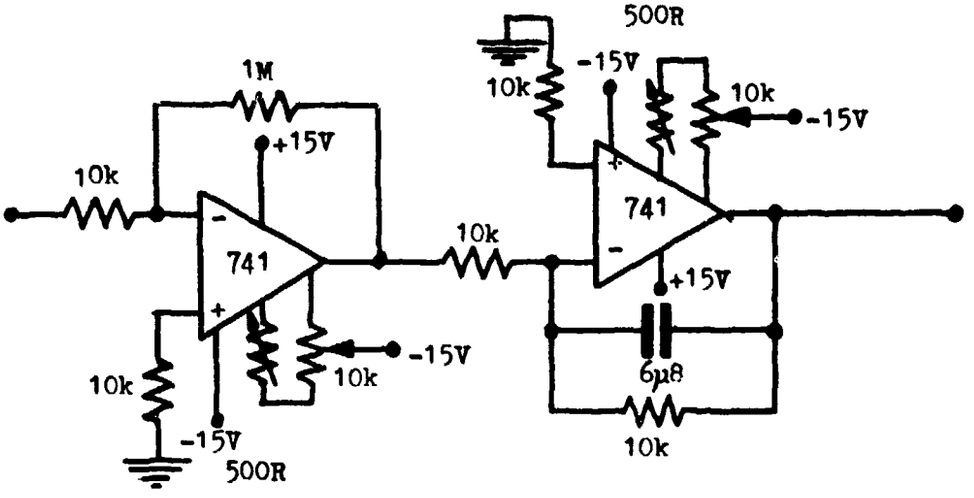

Voltage amplifier and signal integrator

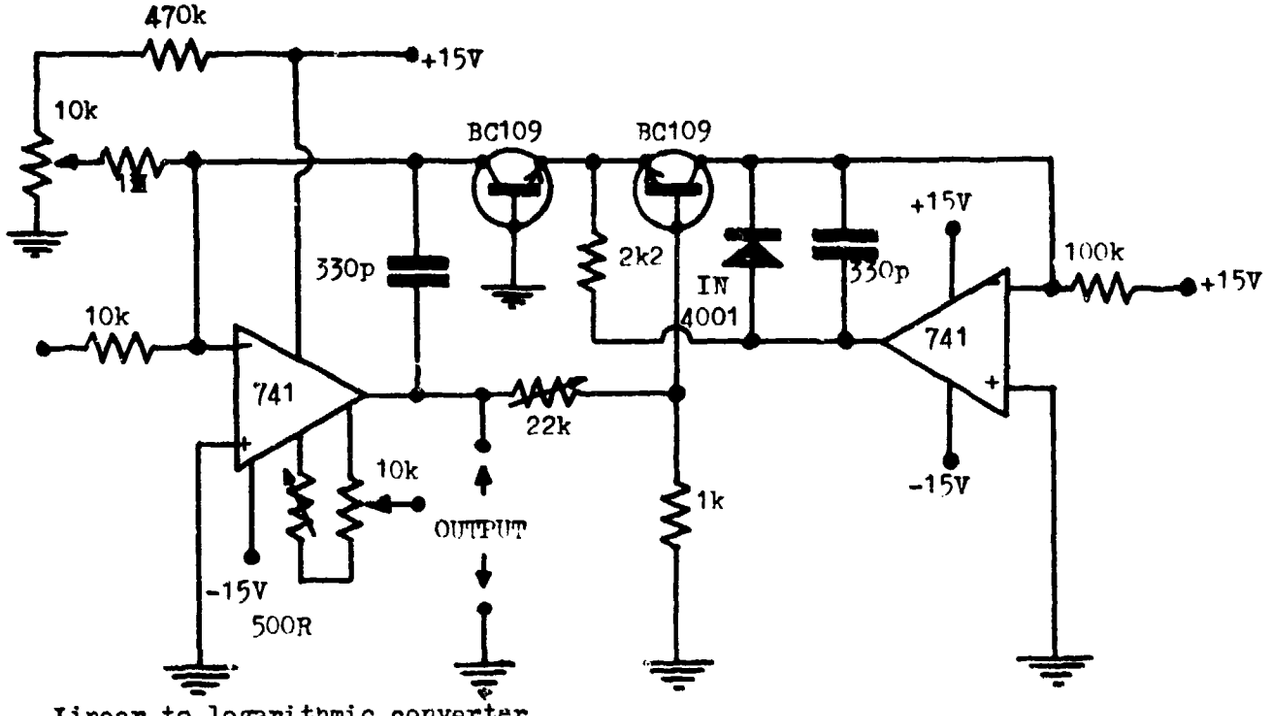

Linear to logarithmic converter

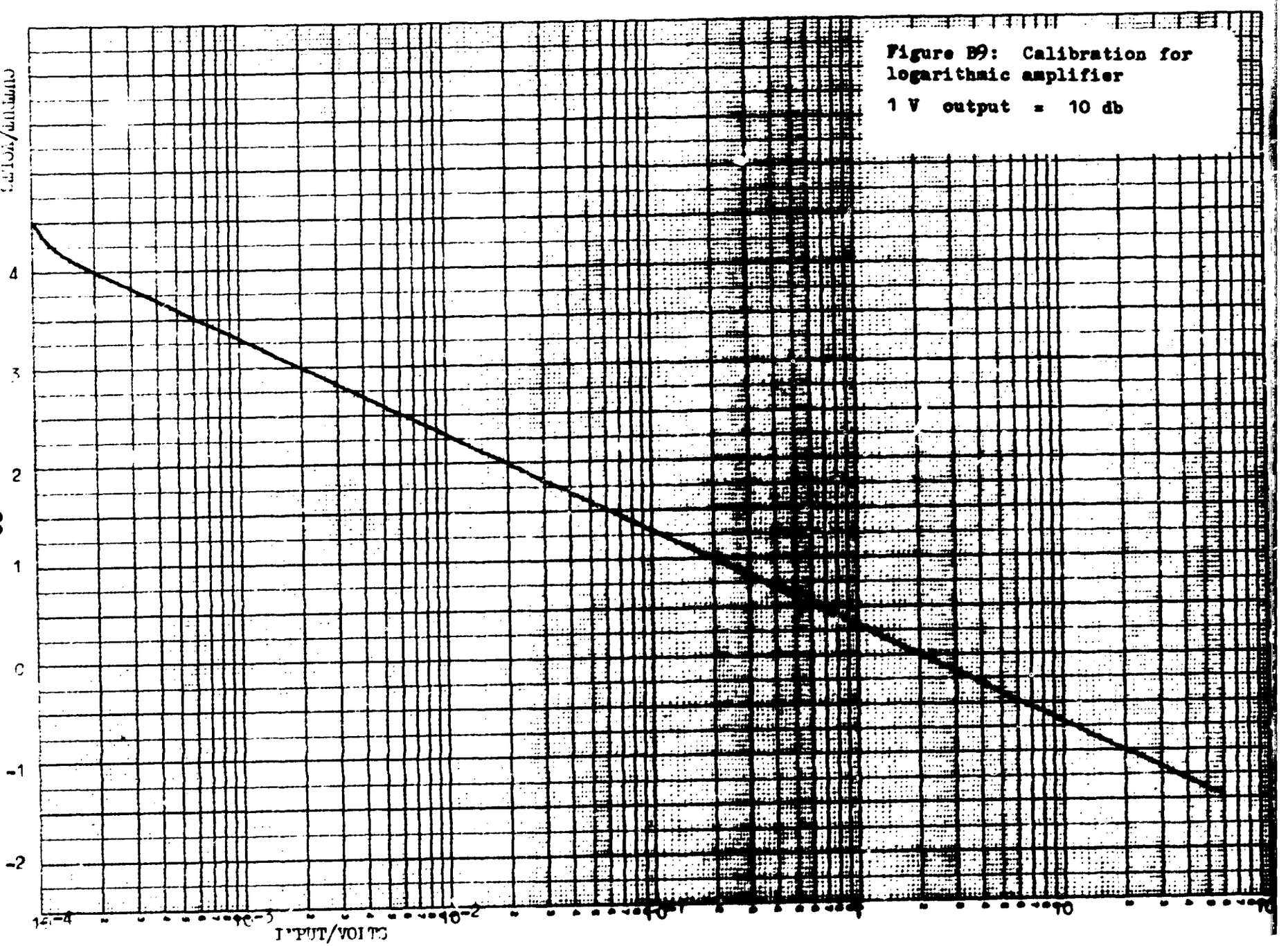

Figure B9: Calibration for logarithmic amplifier

1 V output = 10 db

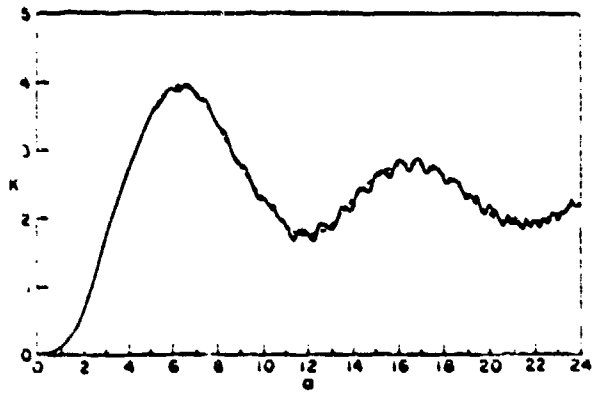

FIG. 1. Scattering coefficient as a function of $\alpha = \pi D/\lambda$ for $m = 1.33$. Solid curve, exact Mie scattering coefficient; dashed curve, smoothed scattering coefficient.

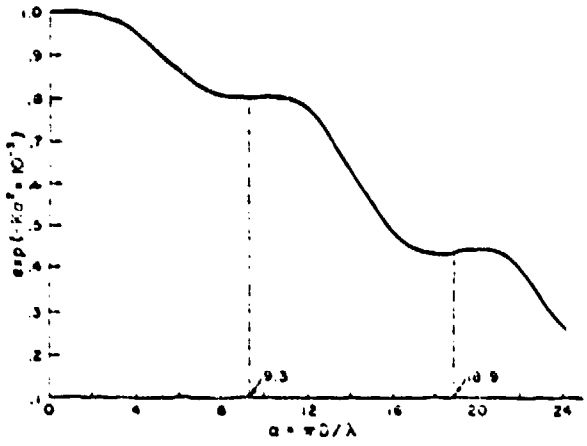

FIG. 2. Mie transmission curve, $\exp(-K\alpha^2 \times 10^{-2})$ vs α, obtained from the data of the dashed curve of Fig. 1 for $m = 1.33$.

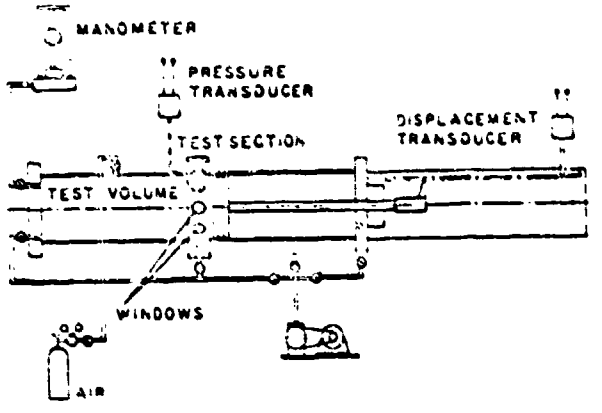

FIG. 3. Schematic diagram of cloud chamber.

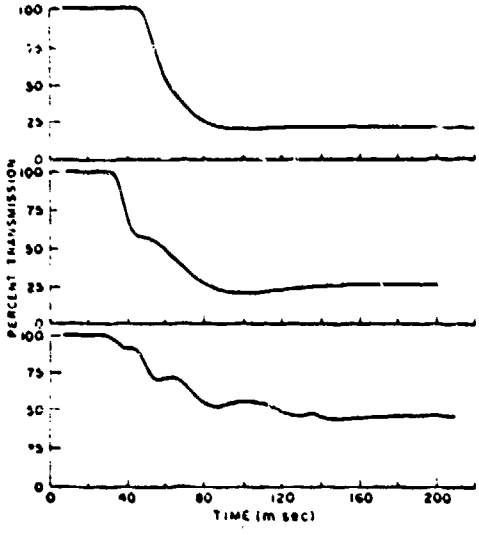

FIG. 5. Typical spectral transmission curves displaying various features.

Figure B10: After J.E. Cole III, R.A. Dobbins, and H. Semerjian, "Time-Resolved Measurement of Droplet Size and Concentration in Cloud Chambers", J. Appl. Meteorology 9, 684 (1970).

Oscillations in scattering cross section $K\pi a^2$ produce steps in $I(z)/I(0)$ versus α (= ak) curve. At second inflection point ak = 9.3 and K = 2.5. Hence a, and from measured $I(z)/I(0) = \exp(-\gamma z)$, where $\gamma = K\pi a^2 N$, one infers N.

PART C: TRANSMITTANCE MEASUREMENTS

Section C1. Attenuation of TEA Laser 10.6μm Pulses

The system shown in figure B1 has been used to produce clouds of length 1.5m with water content ~5 g m^{-3}. Following expansion ports P_1 and P_2 (figure B1) are opened, and a TEA laser pulse (typically 250MW over 20cm^2 beam cross section) is propagated through the cloud. The pulse is focused by a mirror onto a photon drag detector D_1 which is connected directly to the input of one channel of a double beam oscilloscope. A germanium flat, uncoated on one side and antireflection coated for 10.6μm radiation on the other side, diverts 36% of the beam into a path around the chamber; after reflections at three mirrors this beam is focused onto a second photon drag detector D_2 directly connected to the second channel of the oscilloscope.

The Ge flat R_1 served also to deflect a He-Ne laser beam along the path of the 10.6μm beam. The 0.63μm beam was deflected out again by a second Ge flat R_2 which was antireflection coated on both sides.

Typical results are shown in figures C1, C2 and C3. Figures C1a, C2a and C3a are chart recordings of 0.63μm attenuation coefficient for various clouds, showing the times at which the attenuations of TEA laser pulses were measured (automatically recorded by interference pickup spike). Figures C1b, C2b and C3b show the actual pulses as recorded on polaroid film. Figures C1c, C2c and C3c graph the attenuations at 10.6μm and 0.63μm as a function of time over the lifetime of the cloud. Of course a calibrating experiment with no cloud has to be performed in order to establish the relative gains in the two channels, and figure C4 shows the degree of consistency obtained for three such "no-cloud" shots.

It can be concluded that attenuation coefficient at 10.6μm is 10 to 15 times less than at 0.63μm for the sort of clouds we produced. The water content $\Delta\rho$ of these clouds was calculated from equation (B4) to be about 5 g m^{-3}. The mean drop radius, as calculated from $\Delta\rho$ and 0.63μm attenuation according to equation (B9), was about 1.5μm. Hence the concentration of drops was 3.56×10^5 cm^{-3}. The 0.63μm attenuations fell from about 20 dB m^{-1} to about 10 dB m^{-1} after times of about 2, 4 and 11 minutes for clouds 1, 2 and 3 respectively. The fall time for drops of radius 1.5μm is of order 13 - 15 minutes, so that these results suggest that clouds 1 and 2 evaporated before they fell out, but not cloud 3.

It can be concluded, also, that the attenuation by a cloud of water droplets which are optically thin at 10.6μm (i.e. 2a is less than 10μm) of 10.6μm radiation is approximately equal to that of the equivalent thin layer of water. This is implied by the agreement between the theoretical value of $\gamma(10.6\mu m)$ obtained from equation (D29) and the observed value. It implies that scattering is insignificant compared to absorption, which again confirms the small size of the drops (according to figure D3 scattering has fallen to about 15% of absorption at 2μm radius and is negligible at 1μm).

With regard to the large variation in the measured 10.6μm attenuations in figures C1c, C2c and C3c two remarks might be made. In the first place, apparatus alignment was somewhat sensitive to vibration, and some vibration was inevitable when ports were opened and the polaroid film advanced. Secondly, in order to obtain from the photon drag detectors a signal which stood out well above interference pickup from the TEA laser arc and main discharges, it was necessary to operate with power densities of order 15MW cm^{-2} at the surface of the detectors (i.e. 500mV pulses corresponding to 2.5MW for responsivity 0.2 mV kW^{-1} or 15 MW cm^{-2} over the 4mm x 4mm detector area). The threshold for damage is stated to be about 50 MW cm^{-2} but damage was clearly visible on the surface of the germanium crystals after prolonged use. It is thought that the occurrence of a shoulder on several of the upper trace pulses (scale 500 mV $division^{-1}$) was due to excessive power density on the dececter.

The energy density of the laser pulses, about 1 J cm^{-2}, is well below the theoretical threshold of 10 J cm^{-2} for nonlinear effects - evaporation of drops across which the pulse propagates. The optics of the TEA laser (uncoated Ge flat and 1.5m focal length mirror) gave a beam divergence of 10mr which would increase to 50mr on condensing the beam from 5cm to 1cm diameter. Over a 2m path this spreads the beam to 10cm diameter. Dyer et al (A2) report a beam divergence of only 0.2mr for a TEA laser operating in a single transverse mode with an unstable resonator formed by a plane mirror of diameter 2.85cm and a convex mirror of diameter 7.5cm and focal length -14.5m; the separation was 1.3m. We plan to use a convex mirror of focal length -4.5m and diameter 3.75cm in confocal arrangement with a concave mirror of focal length 5m and diameter 7.5cm (expansion 4/3 per pass), but the 7.5cm Ge flat on which the reflector is to be mounted requires to be anti-reflection coated and we are awaiting delivery of this item.

Section C2. Cloud Clearing with a CW 10.6μm Beam

The effect of a CW 10.6μm beam of power 3 - 5 W and diameter 3mm in altering the transmittance of a cloud to a collinear 0.63μm beam from a He-Ne laser has been investigated. Accurate spatial coincidence of the beams can be achieved by expanding the 0.63μm beam to a diameter greater than that of the 10.6μm beam and then defining the path of the coincident beams by allowing the 10.6μm beam to burn holes in two pieces of cardboard.

Significant clearing was achieved only toward the end of a cloud lifetime when it had thinned considerably. The chart recording in figure C6 shows how the transmittance of the He-Ne laser beam varies after the 10.6μm beam is switched on. The transmittance rises from 6% to 28.6% in three seconds, then declines in 2s to a steady value of 17%, and finally it declines to about 6% again 1s after the beam is switched off.

In figure C7a eight such clearing episodes were recorded during the evolution of a cloud produced by feeding steam from an electric kettle into the cool expansion chamber. The magnitude of the clearing incre-

ases considerably as the cloud dispels, an effect also noted by Mullaney et al (C1) (figure C11). In this chart recording transmittance rather than attenuation coefficient is recorded, the logarithmic converter being omitted. The clearing episodes shown in chart C7a are expanded (in time) in the sequence of oscillographs shown in figure C7b. In general the transmittance rises to a peak, and then decreases to a steady-state value apparently because convection draws a steady flow of drops into the beam. Note that the steady-state clearing is only 0.2V at episode no.1 when the cloud is thickest, and has risen to 2.0V at episode no.8 when the cloud is thinnest.

The attenuation of the CW 10.6μm beam should fall owing to evaporation of drops during cloud clearing. Thus attenuations for a CW 10.6μm beam should be smaller than for a TEA laser 10.6μm pulse. We have not made this comparison, but figures C9b and C10b show how CW 10.6μm attenuation varies during evolution of respectively a steam cloud (figure C9a) and a very long duration expansion cloud with ion plus smoke nucleation (figure C10a). The oscillographs record the output from a pyroelectric detector due to the 100Hz (full wave rectified supply frequency) ripple component present in the laser output. (Use of this AC component was convenient and allowed the use of the entire laser output, which the use of a chopper would not. However, since the modulation level was only 5.5% of the DC level, the ripple cannot have significantly affected the observations). The response of the detector is shown in figure C8. For the steam cloud the attenuation at 10.6μm fell from 3.6 dB m^{-1} to zero while that at 0.63μm fell from 11.7 dB m^{-1} to 1.3 dB m^{-1}. In the case of the expansion cloud, the attenuation decreased from 2 dB m^{-1} to 0.13 dB m^{-1} at 10.6μm while the 0.63μm attenuation decreased from 14.7 dB m^{-1} to 2.0 dB m^{-1}.

The ratio of attenuation coefficients, $\gamma(0.63)/\gamma(10.6)$, was 3.3 for the steam cloud but 7.3 for the expansion cloud, implying that the drop size was greater in the steam cloud (see figures D3 and D6). In fact the ratio $\gamma(0.63)/\gamma(10.6)$ is a sensitive indicator for drop size, which might provide the basis for a useful field instrument since $\gamma(10.6)$ gives Δp directly for drops with diameter less than 10μm.

Figure C1a: Chart recording of $\log[I(z)/I(0)]$ for the 0.63 μm beam propagating through cloud 1 produced by adiabatic expansion from excess pressure 5 psi with 40 mA discharge for ion nucleation, showing times at which attenuations of TEA laser pulses were taken. Note time difference between the two recorder pens - 0.17"; port is opened shortly after the temperature drop.

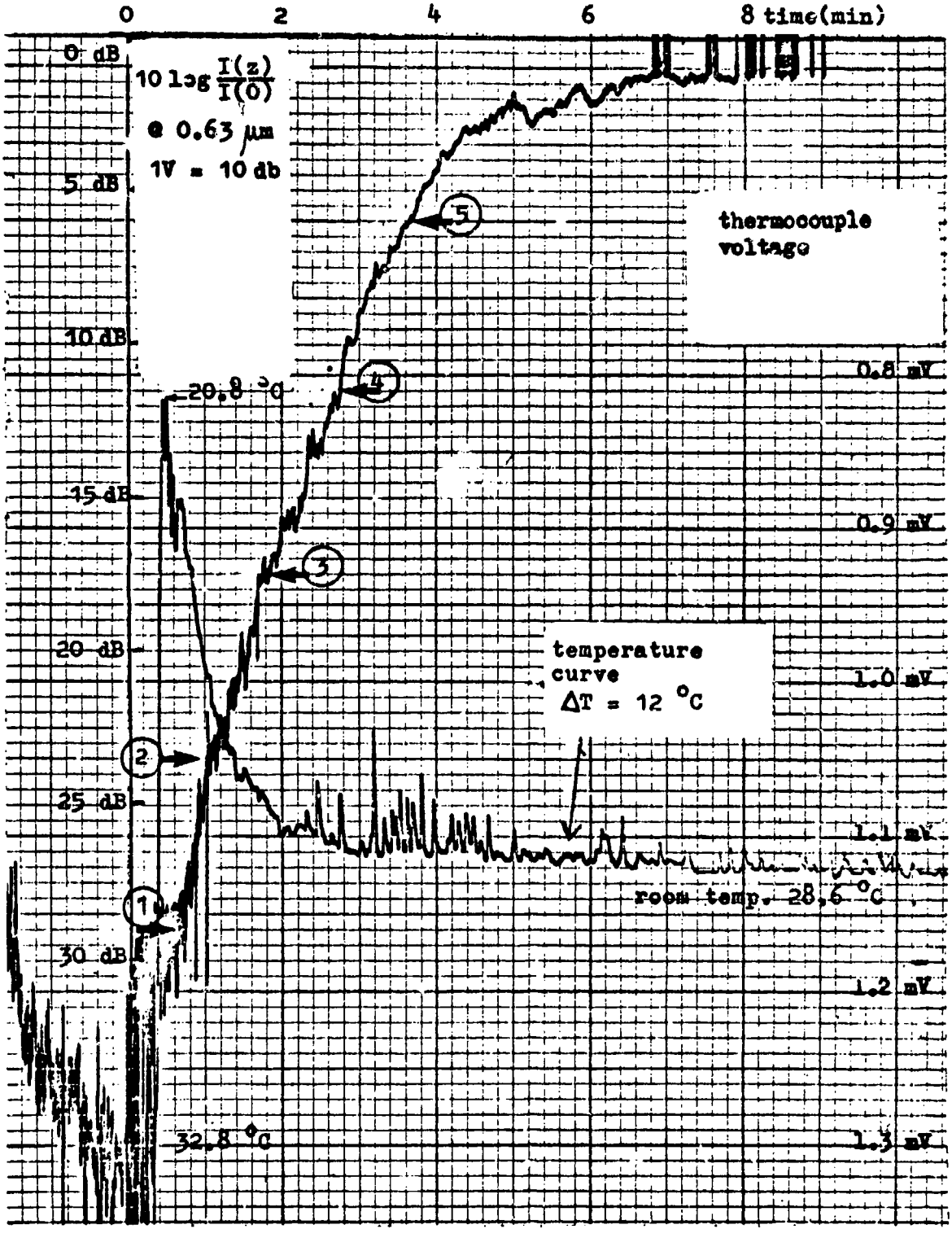

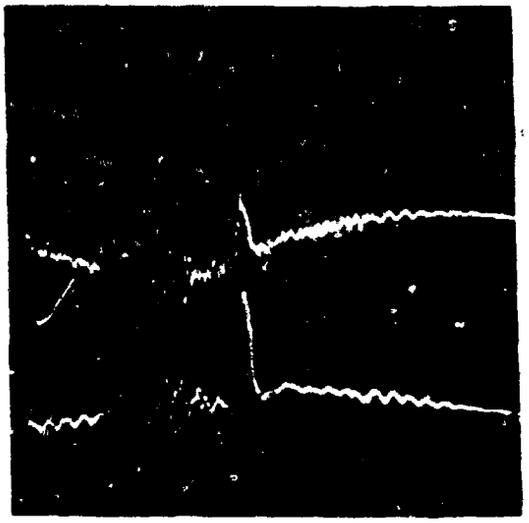

1

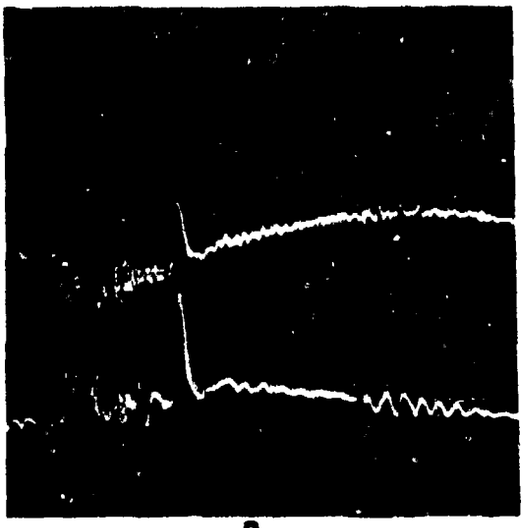

2

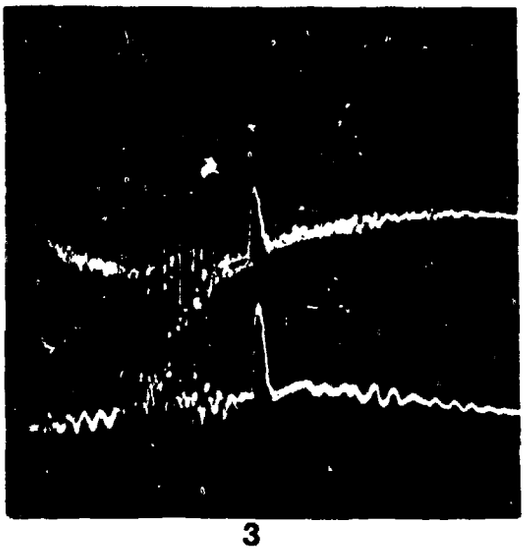

3

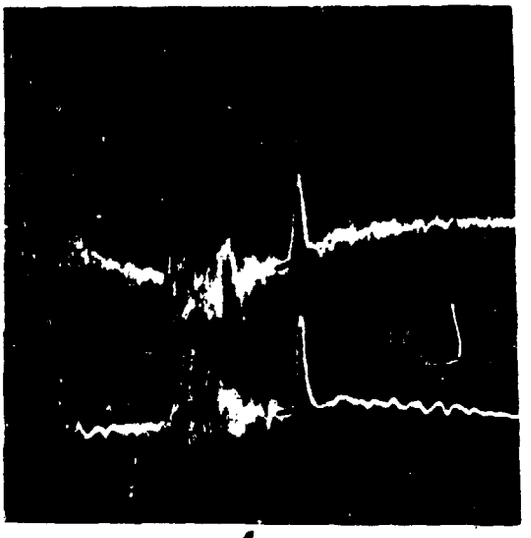

4

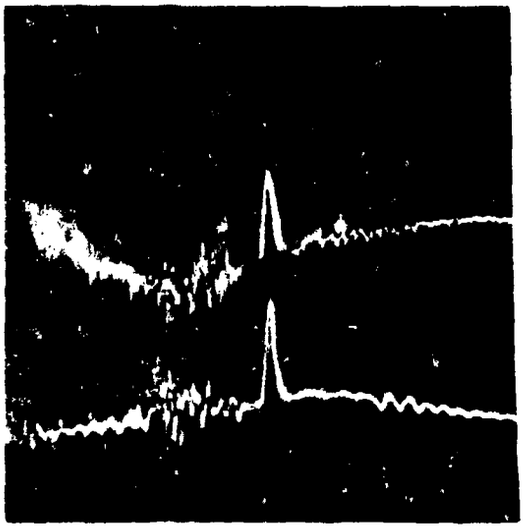

5

Figure C1b: Attenuation of TEA laser pulses ($\sim$10 MW/cm^2 over 20 cm^2) at various times during the evolution of cloud 1 (see figure C1a).

Corrected transmittances are:

(1)	t + 30 sec	0.64
(2)	t + 60 sec	0.66
(3)	t + 100 sec	0.78
(4)	t + 160 sec	0.98
(5)	t + 220 sec	0.98

upper trace: through chamber (500mV/div)
lower trace: around chamber (200mV/div)

sweep speed: 0.5 μs/div

no cloud: pulse ratio = 0.94

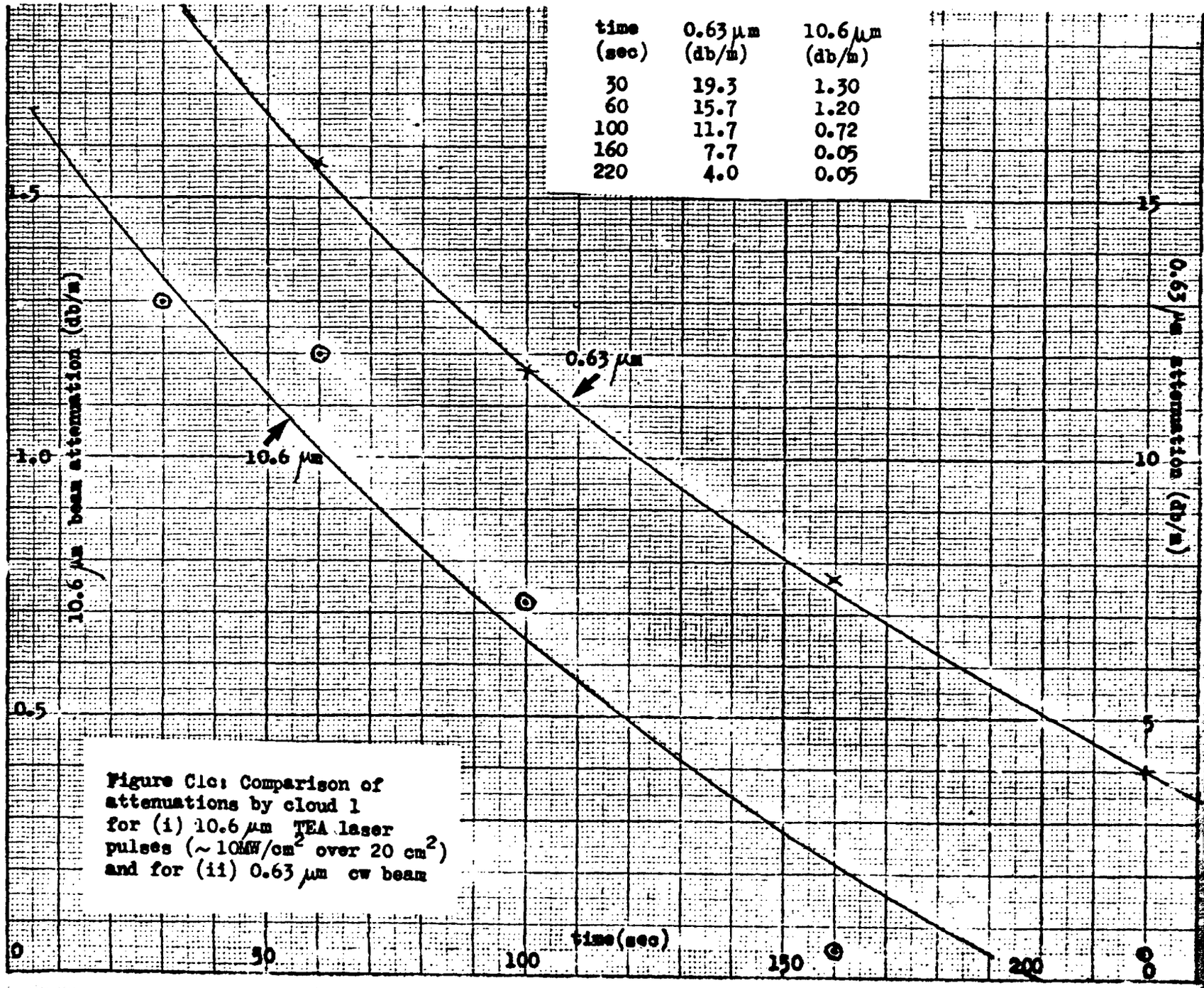

Figure C1c: Comparison of attenuations by cloud 1 for (i) 10.6 μm TEA laser pulses (~10MW/cm^2 over 20 cm^2) and for (ii) 0.63 μm cw beam

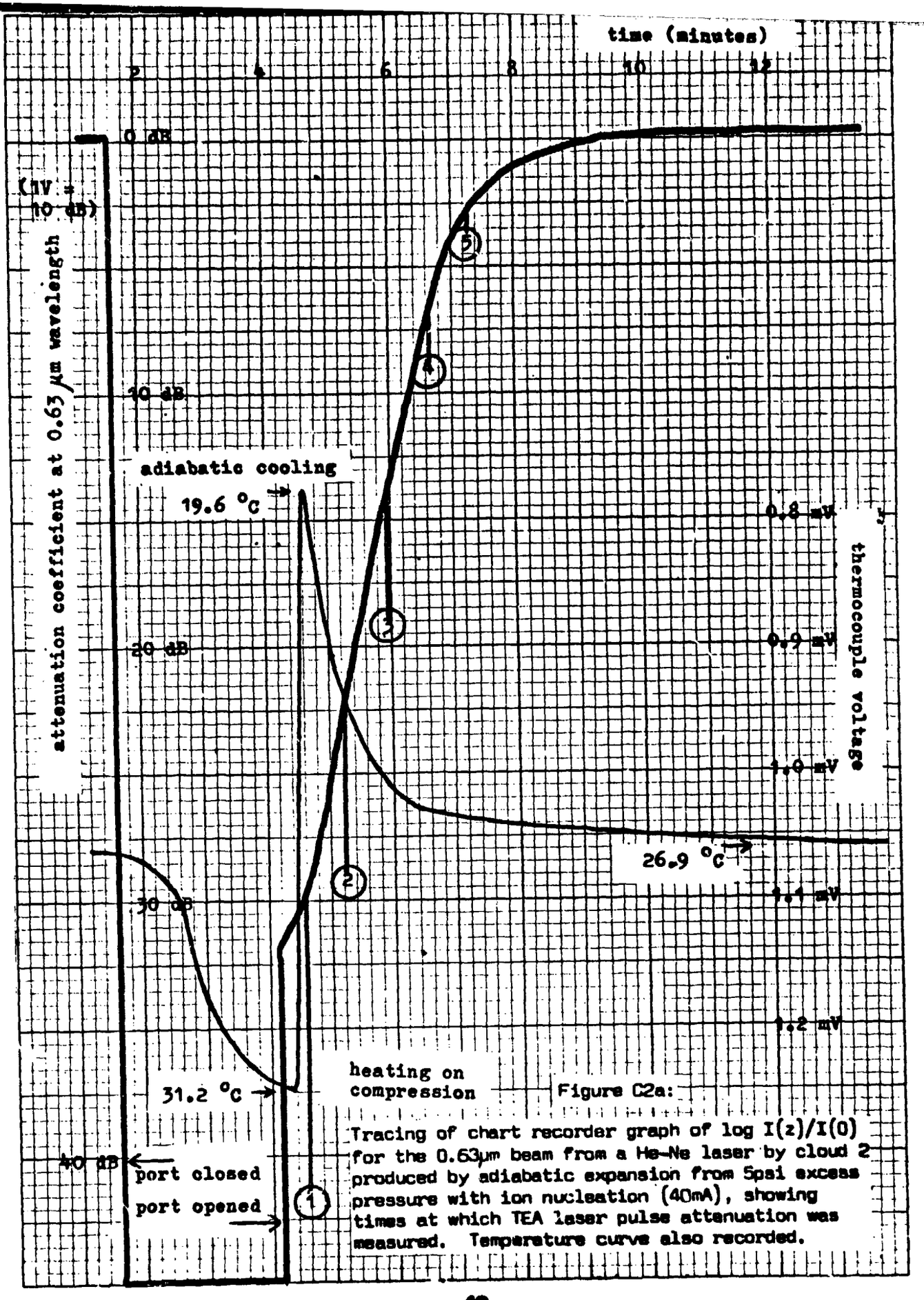

Figure C2a:

Tracing of chart recorder graph of log I(z)/I(0) for the 0.63μm beam from a He-Ne laser by cloud 2 produced by adiabatic expansion from 5psi excess pressure with ion nucleation (40mA), showing times at which TEA laser pulse attenuation was measured. Temperature curve also recorded.

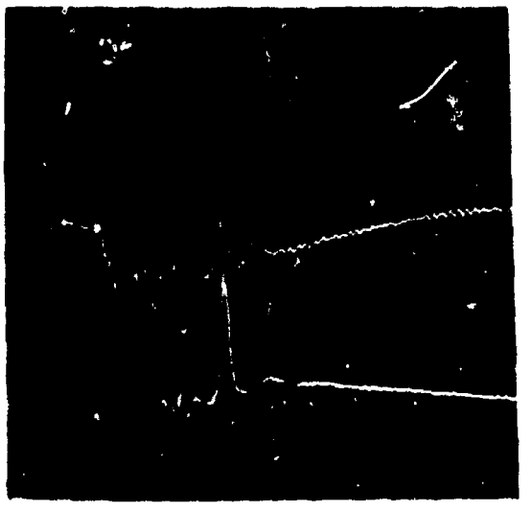

1

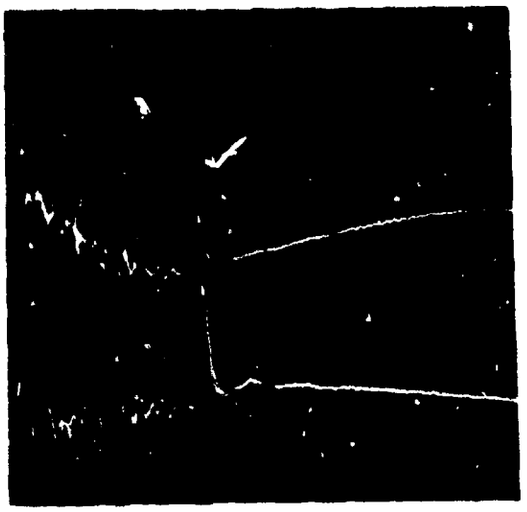

2

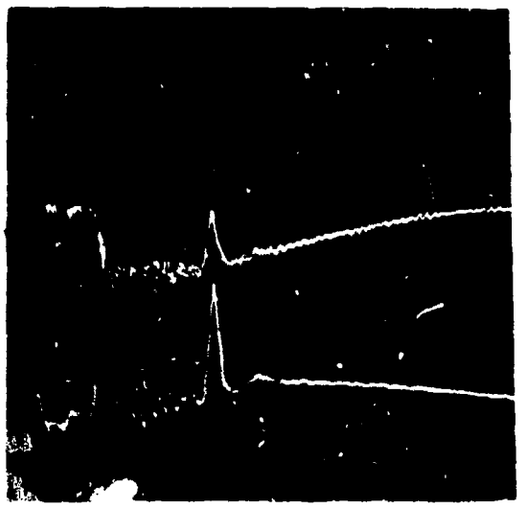

3

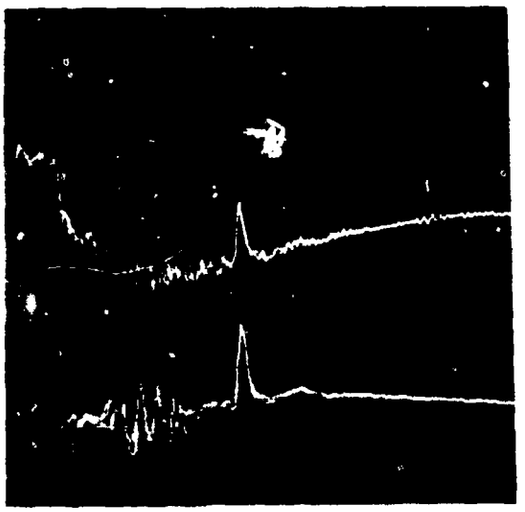

4

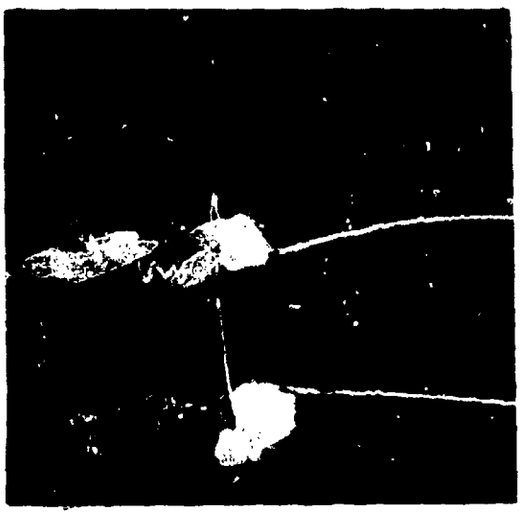

5

Figure C2b: Attenuation of TEA_2 laser pulses (~10 MW/cm^2 over 20 cm^2) at various times during evolution of cloud 2 (see figure C2a).

Corrected transmittances are:

(1) t + 15 sec 0.52
(2) t + 60 sec 0.61
(3) t + 100 sec 0.67
(4) t + 140 sec 0.90
(5) t + 180 sec 0.97

upper trace: through chamber(500 mV/div)
lower trace: around chamber (200 mV/div)

sweep speed: 0.5 μs/div

no cloud: pulse ratio = 0.77

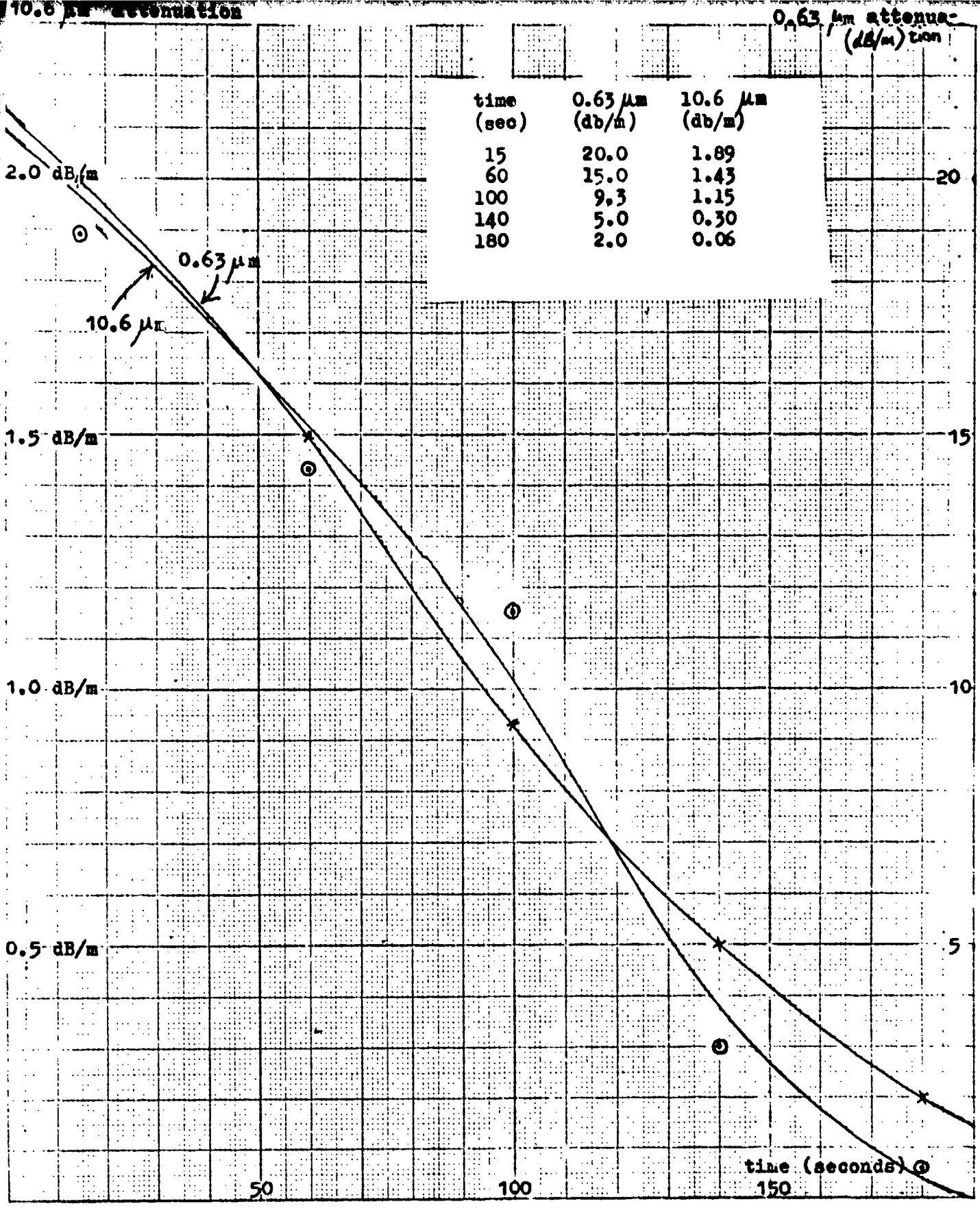

Figure C2c: Comparison of attenuations by cloud 2 for (i) 0.63 μm beam, and (ii) 10.6 μm beam, as the cloud dispels. (TEA laser pulses of ~10 MW/cm^2 and beam cross section 20 cm^2).

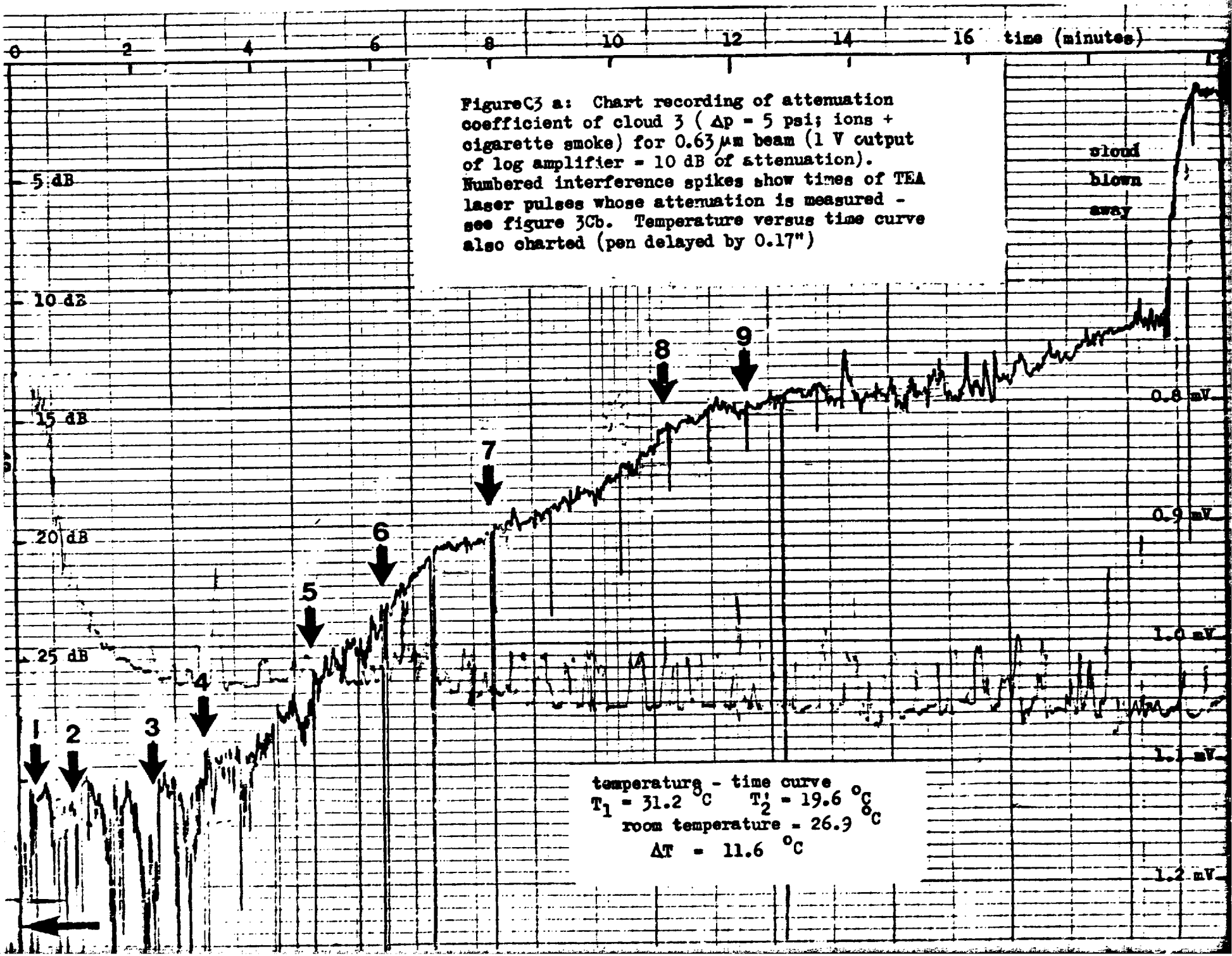

Figure C3 a: Chart recording of attenuation coefficient of cloud 3 (Δp = 5 psi; ions + cigarette smoke) for 0.63 μm beam (1 V output of log amplifier = 10 dB of attenuation). Numbered interference spikes show times of TEA laser pulses whose attenuation is measured - see figure 3Cb. Temperature versus time curve also charted (pen delayed by 0.17")

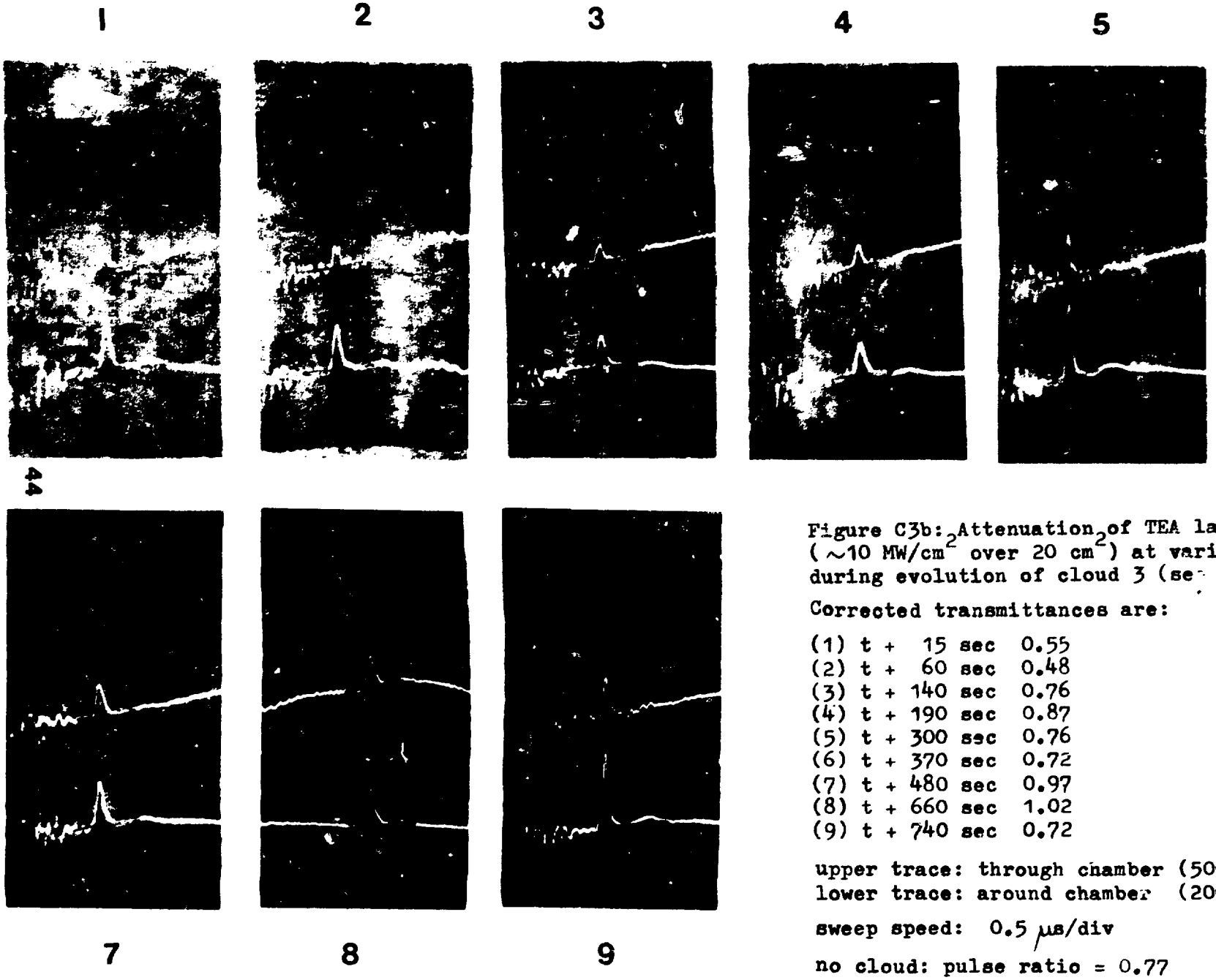

Figure C3b: Attenuation of TEA laser ($\sim$10 MW/cm^2 over 20 cm^2) at various during evolution of cloud 3 (see fig

Corrected transmittances are:

(1) t + 15 sec 0.55
(2) t + 60 sec 0.48
(3) t + 140 sec 0.76
(4) t + 190 sec 0.87
(5) t + 300 sec 0.76
(6) t + 370 sec 0.72
(7) t + 480 sec 0.97
(8) t + 660 sec 1.02
(9) t + 740 sec 0.72

upper trace: through chamber (500 m
lower trace: around chamber (200 m

sweep speed: 0.5 μs/div

no cloud: pulse ratio = 0.77

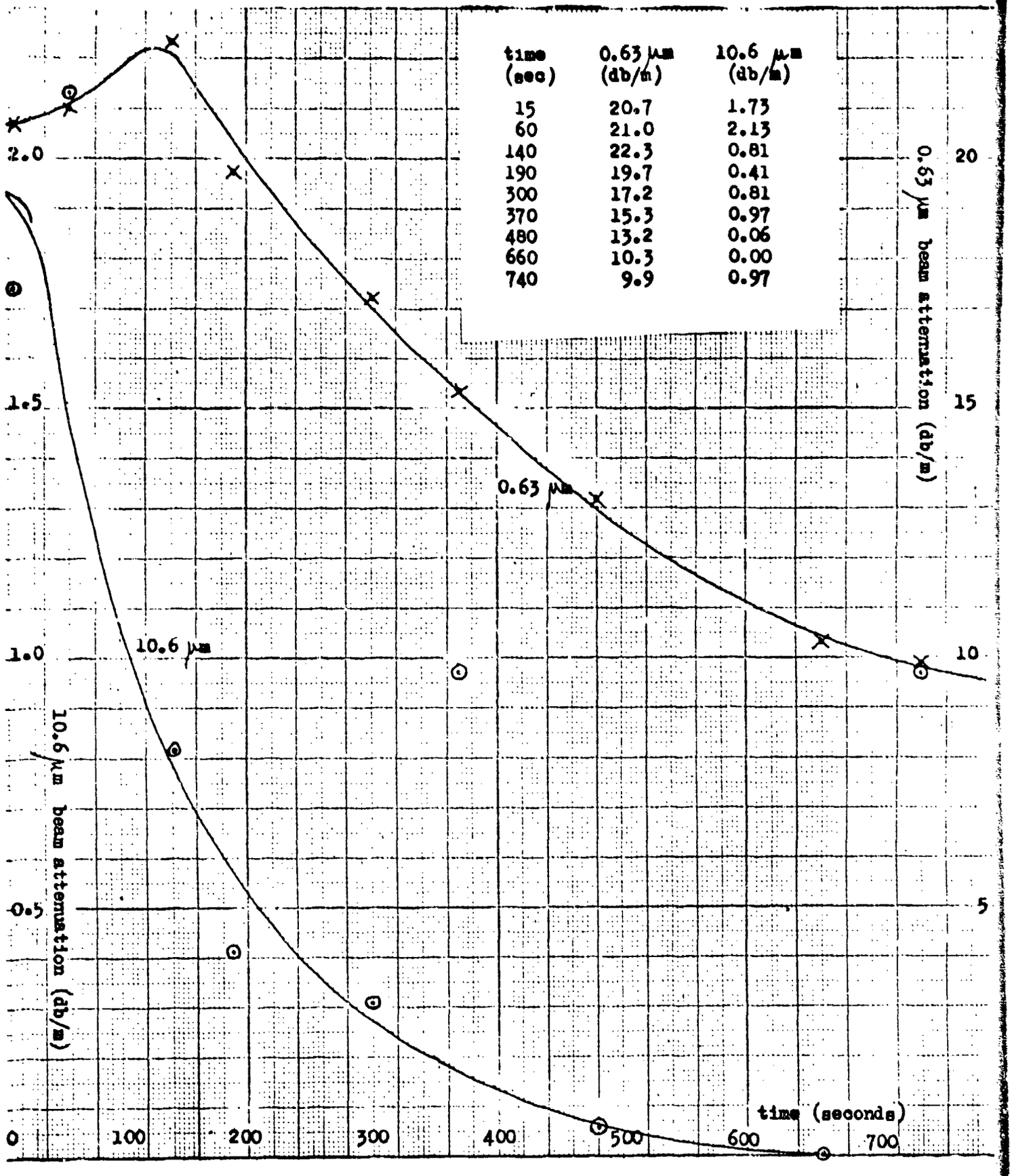

Figure C3o: Comparison of attenuations by cloud 3 for (i) 10.6 μm TEA laser pulses (~10 MW/cm^2 over 20 cm^2) and for (ii) 0.63 μm cw beam.

13.0

——— = 0.72

18.0

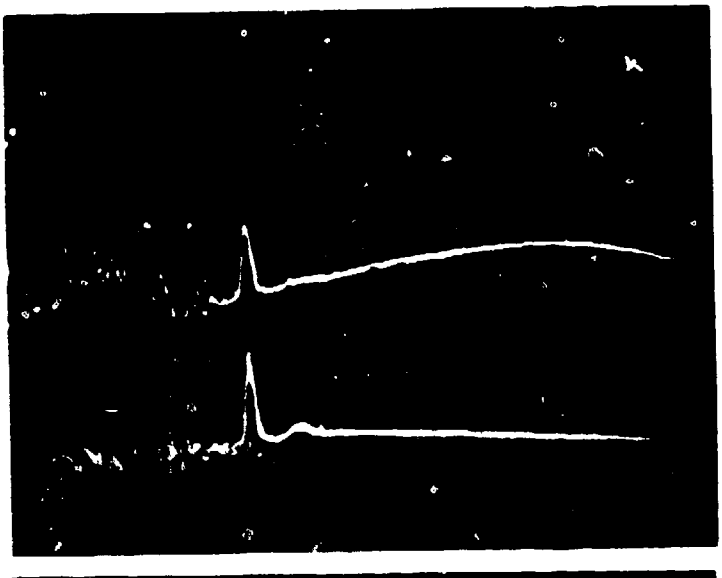

9.5

——— = 0.79

12.0

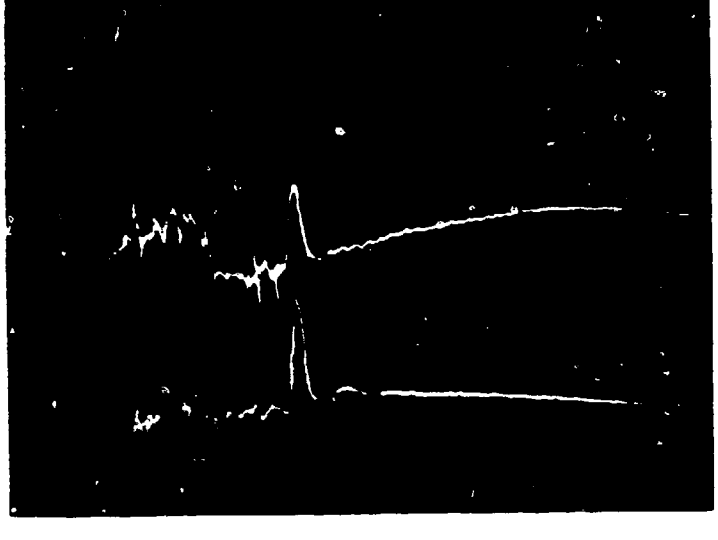

11.0

——— = 0.79

14.0

average = 0.77

Figure C4: No cloud experiments to establish relative gains for the through-chamber and around-chamber channels
Upper trace: through chamber (500 mV/div)
Lower trace: around chamber (200 mV/div)
Sweep speed: 0.5 μs/div

Cloud No.	Δp (psi)	ΔT_o (^oK)	ΔT (^oK)	$\Delta \rho$ (g/m^3)	T (^oK)	T_2 (^oK)	rel humid (%)	$\gamma(0.63\mu)$ (m^{-1})	$\bar{a}$ (μm)	fall time for 25 cm (min)	cloud decay time (min)	$\gamma(10.6\mu)$ (m^{-1}) obs.	$\gamma(10.6\mu)$ (m^{-1}) theor.
1	5	24.1	12.0	4.59	301.6	293.8	47	4.3	1.50	15.3	2.25	0.30	0.44
2	5	24.1	11.6	4.72	300.0	292.6	58	4.9	1.44	16.6	4.25	0.43	0.45
3	5.5	26.2	10.9	5.83	299.7	292.7	73	5.5	1.58	13.8	11.0	0.40	0.55

Δp = initial excess pressure over one atmosphere (1 atm = 14.7 psi)

ΔT_c = temperature fall without condensation

ΔT = observed temperature fall

$\Delta \rho$ = mass of water condensed per unit volume of cloud: calculated from $\Delta \rho = 0.38(\Delta T_o - \Delta T)$ g/m^3

$\gamma(0.63\mu)$ = attenuation coefficient at wavelength 0.63 μm: $I(z) = I(0) \exp(-\gamma z)$

t = time calculated from Stokes's law

cloud decay time is taken as time for $\gamma(0.63\mu)$ to decline to half its initial value

$\gamma(10.6\mu)$ = attenuation coefficient at wavelength 10.6 μm. Theoretical value calculated from $\gamma(10.6\mu) = \kappa\Delta\rho/d$ where κ is the linear absorption coefficient of liquid water and d is the mass density of liquid water: $\kappa = 2k n'$; $\tilde{n} = n + in' = 1.175 + i0.0802$

$\bar{a}$ = mean drop radius: calculated from $\bar{a} = 3\Delta\rho/[2d\,\gamma(0.63\mu)]$

Figure C5: Summary of results for three typical clouds. Observed attenuation for TEA laser pulses (below the non-linear threshold) is compared to the theoretical attenuations.

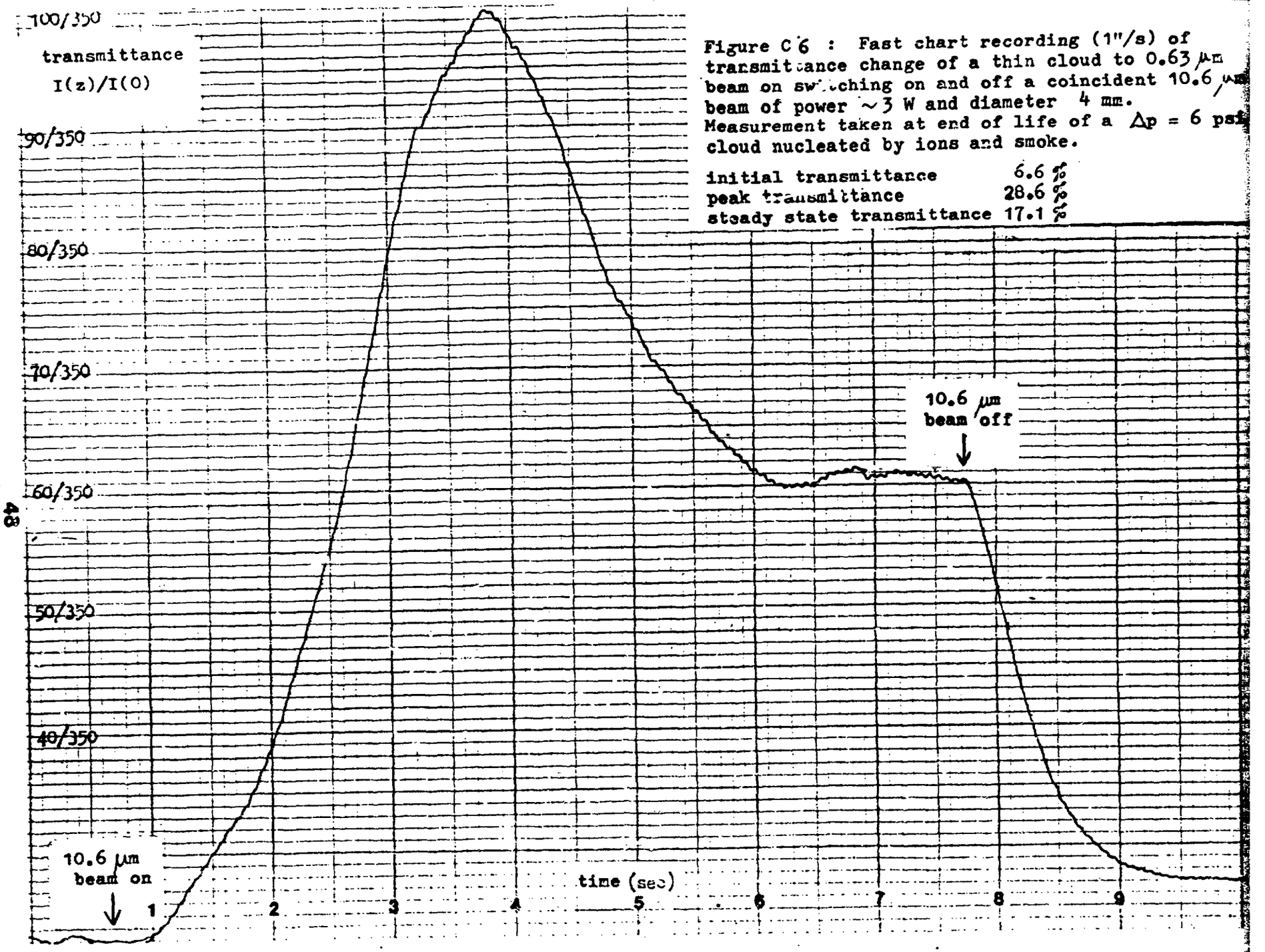

Figure C 6 : Fast chart recording (1"/s) of transmittance change of a thin cloud to 0.63 μm beam on switching on and off a coincident 10.6 μm beam of power ~3 W and diameter 4 mm. Measurement taken at end of life of a Δp = 6 psi cloud nucleated by ions and smoke.

initial transmittance	6.6 %
peak transmittance	28.6 %
steady state transmittance	17.1 %

Figure C7a: Transmittance of steam cloud A at 0.63 μm versus time as cloud dispels (chart speed 0.5"/min). At times marked 1,2,3,4,5,6,7,8 a 10.6 μm beam of power $\sim$3W and diameter $\sim$4 mm was switched on and off. Expanded records of transmittance variation at these times are shown in figure C7b.

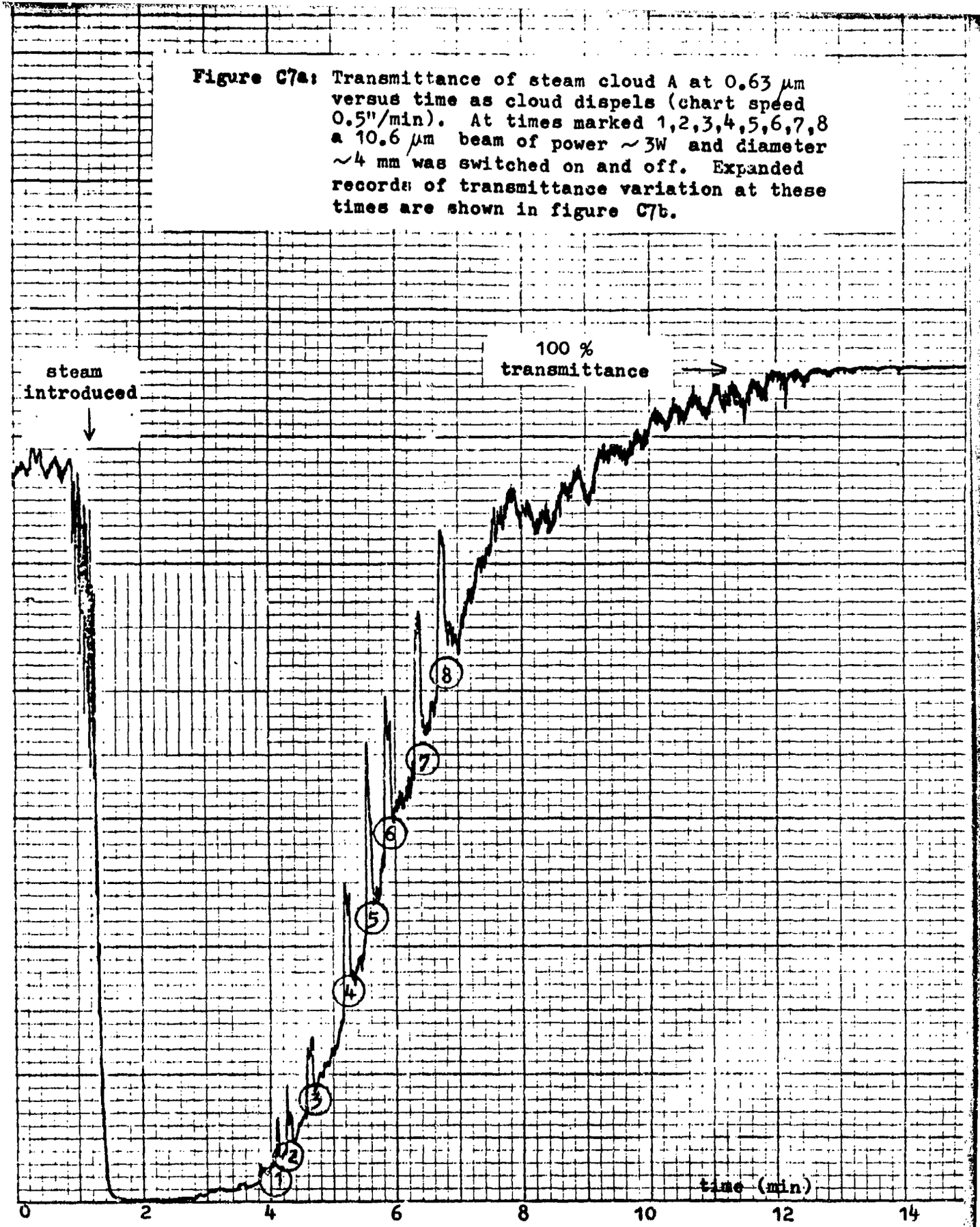

1 V = 2 μA of photomultiplier current

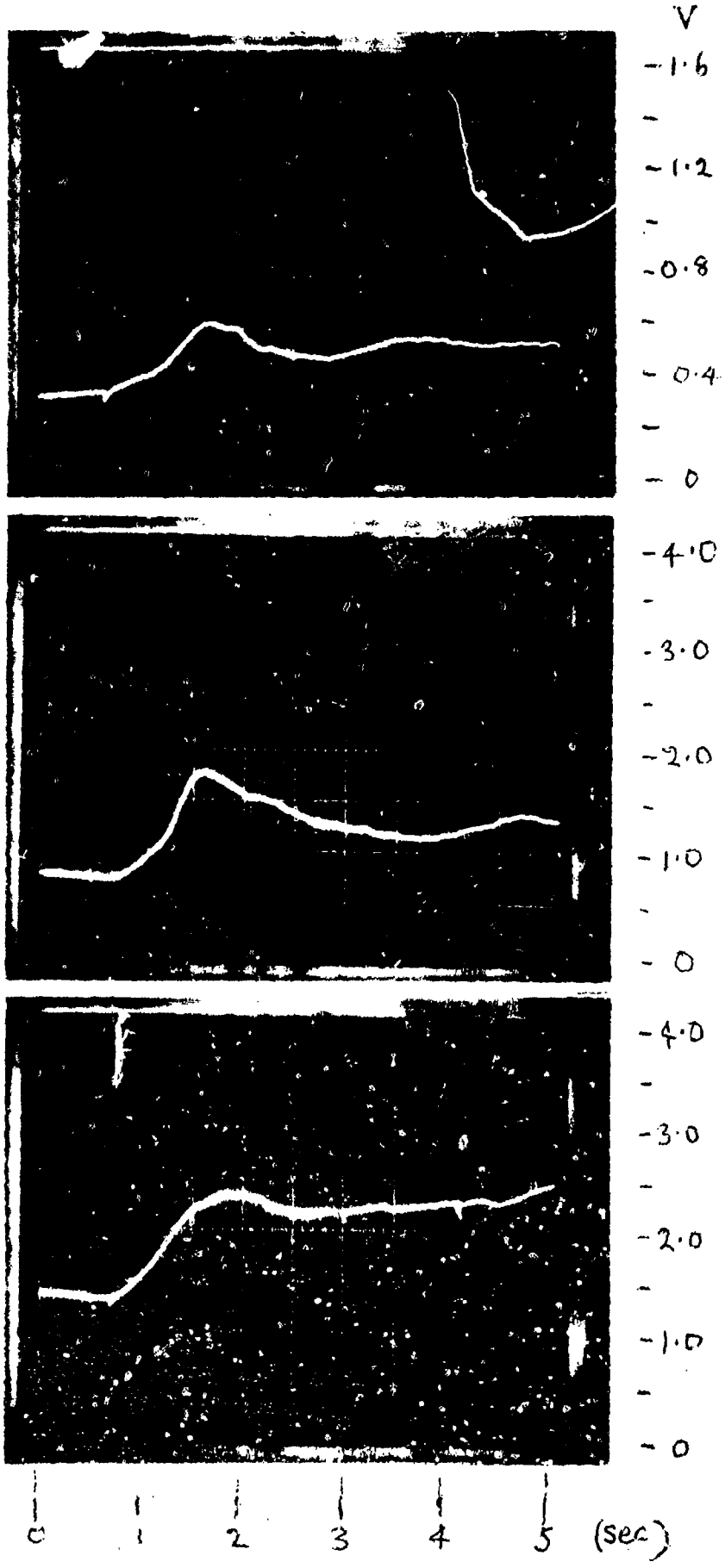

Fig. C7b

1 V = 2 μA of photomultiplier current

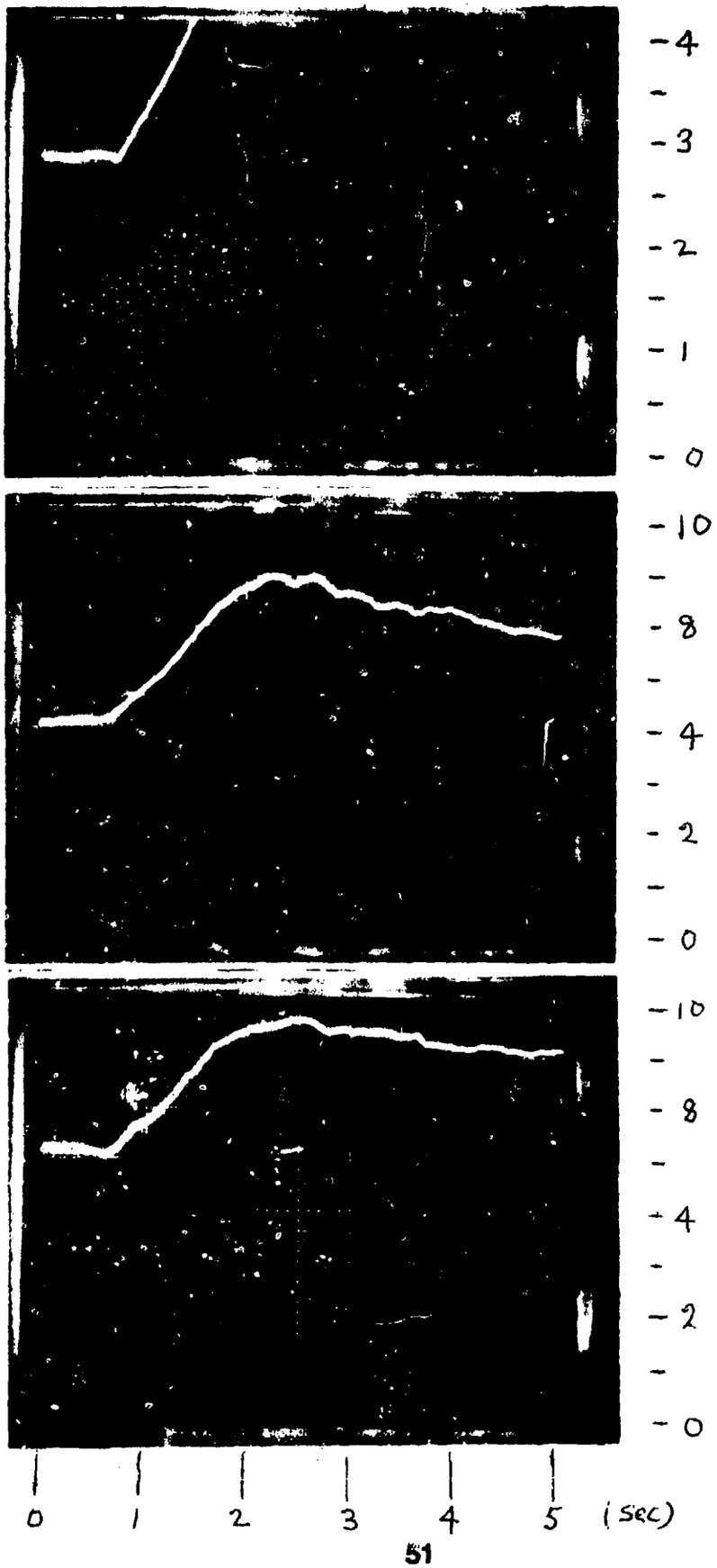

Fig. C7b

1 V = 2 μA of photomultiplier current

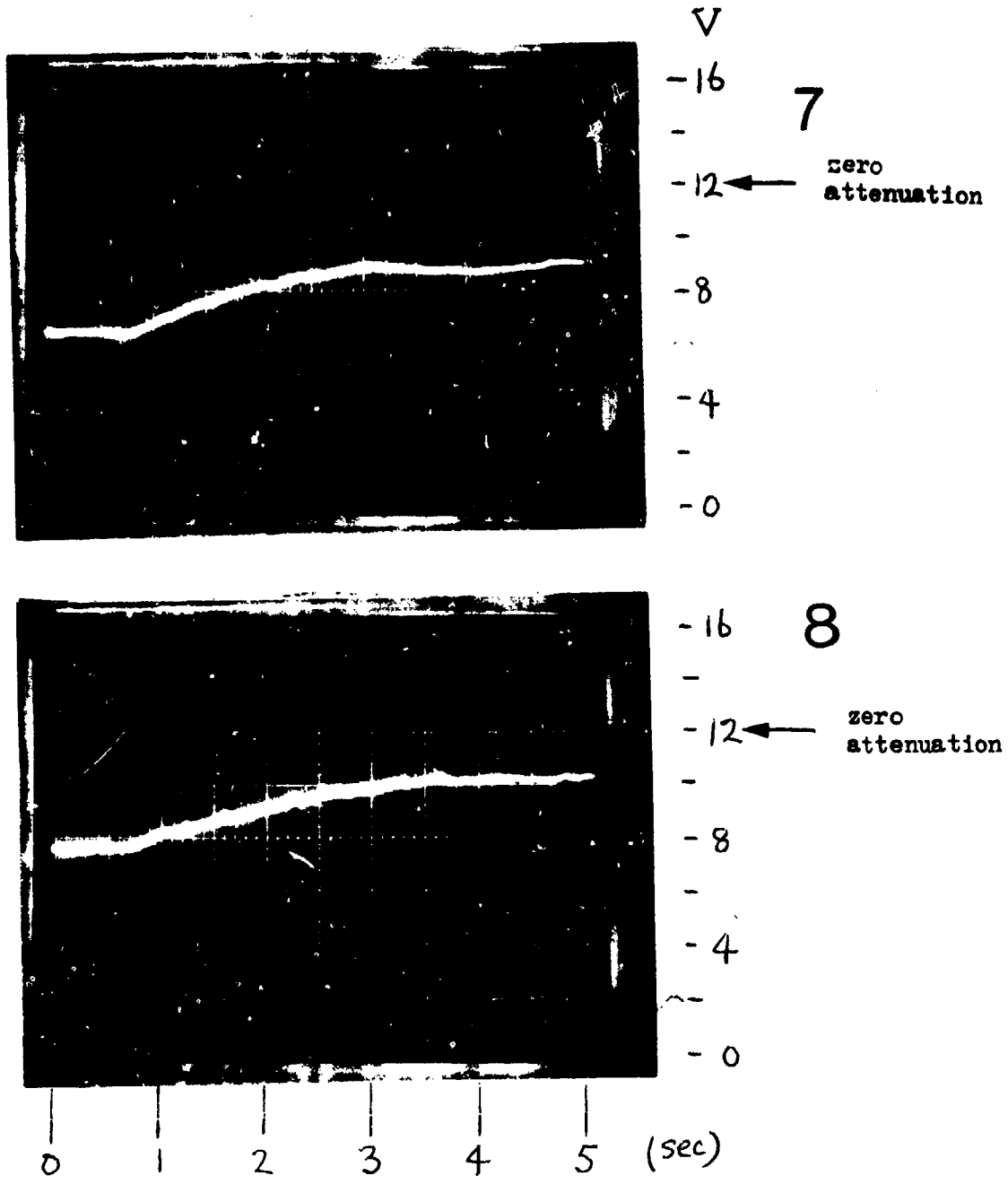

Figure C7b: Clearing by 10.6 μm beam (~ 3 W, 4 mm diam.) of steam cloud A at various times as the cloud dispels, as monitored by transmittance to 0.63 μm beam coincident with infra-red beam.

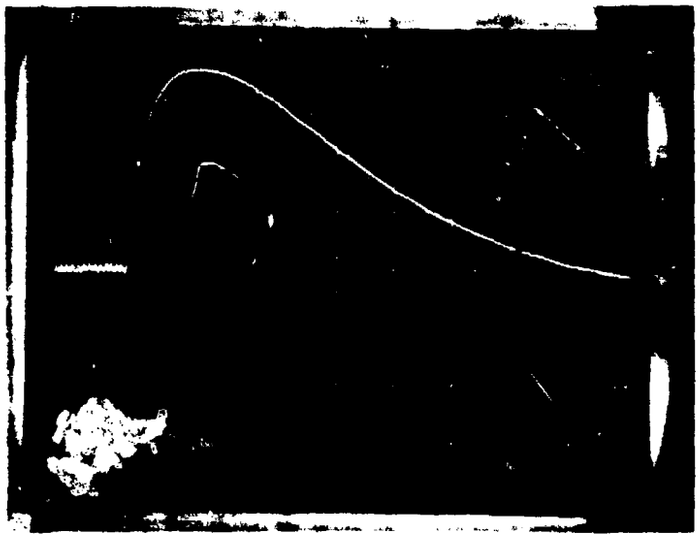

(a)

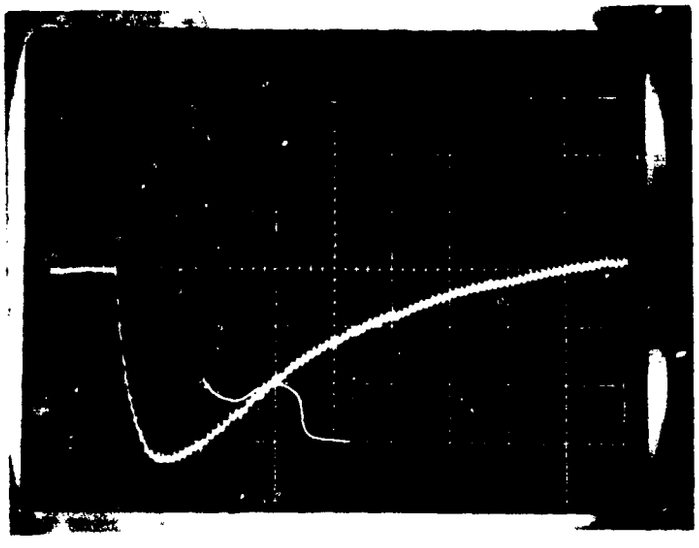

(b)

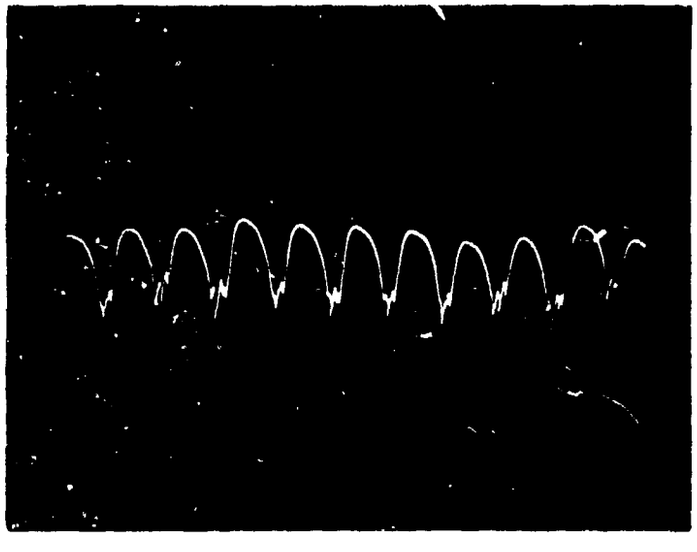

(c)

Figure C8:

Response of Plessey triglycine sulphate pyroelectric detector (type PSC222) with responsivity 10^5 V/W to (a) switching off (b) switching on , and (c) 5.5% modulation at 100 Hz of cw CO_2 laser radiation.

For (a) and (b) scales are:
vertical: 0.5 V/div
horizontal: 0.2 s/div

Figure C9a: Attenuation of a steam cloud for 0.63 μm beam from a He-Ne laser as a function of time, using log amplifier (1V = 10 dB = 2" chart)

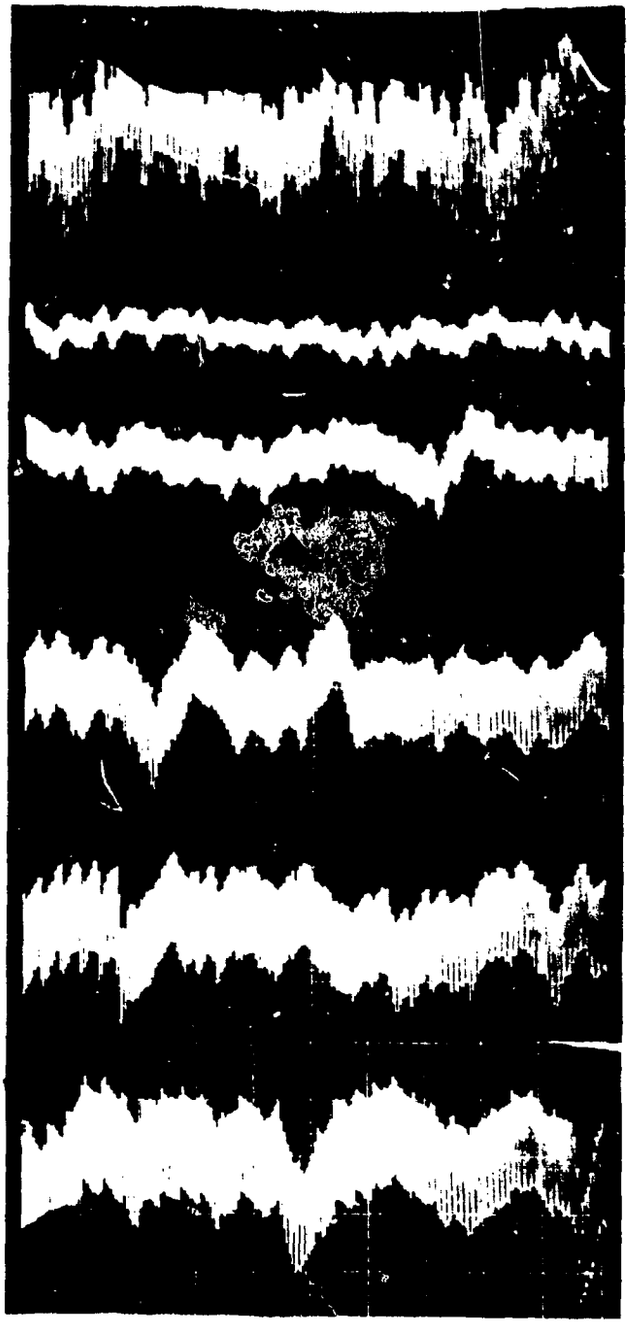

Figure C9b : Attenuation of 3 W cw 10.6 μm beam and attenuation of 0.63 μm beam as a function of time after formation of steam cloud (introduction of steam from electric kettle). 5.5%100 Hz modulation of the cw beam is monitored by a pyroelectric detector; each pulse in above slow sweeps represents the amplitude of this modulation signal. A chart recording of 0.63 μm attenuation (using log amplifier) is shown in figure C10 .

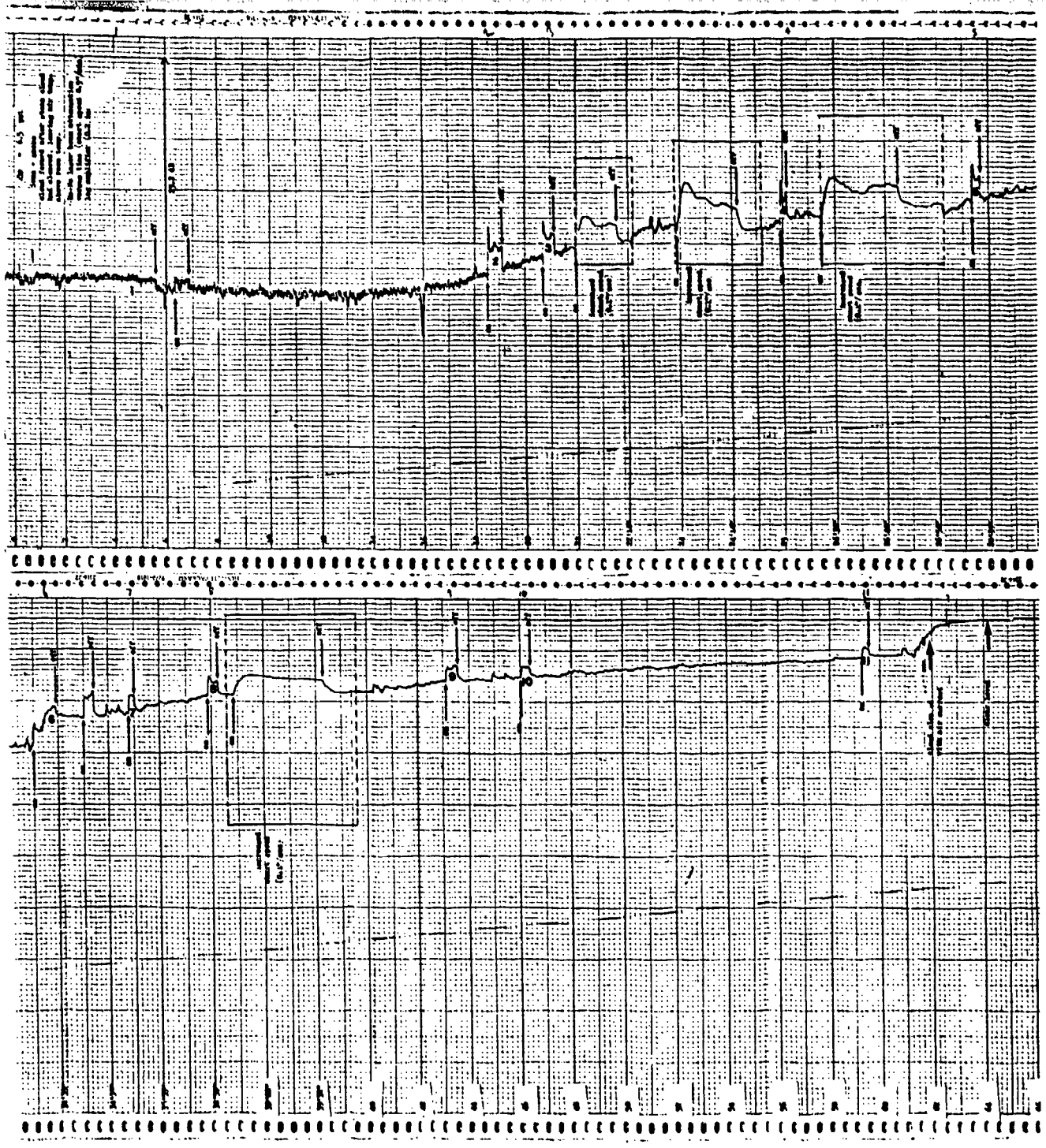

Figure C10a: Attenuation of an expans on cloud (ion + smoke nucleation) for 0.63 μm radiation from a He-Ne laser as a function of time, using logarithmic amplifier (1 V = 10 dB). Gas was slightly pre-heated by a steam cloud. Δp = 6.5 psi .

The attenuation was reduced at times 1, 2 ... 11 , when a 3W (4 mm diameter) cw 10.6 μm beam was switched on (amount of cloud clearing not accurate due to different beam diameters). The normal chart speed of 0.5"/min was increased to 0.1"/sec for four such periods.

Figure C10b: Attenuation of 3 W cw 10.6 μm beam for long duration expansion cloud
(Δp = 6.5 psi : ions & smoke;
air preheated by previous steam)

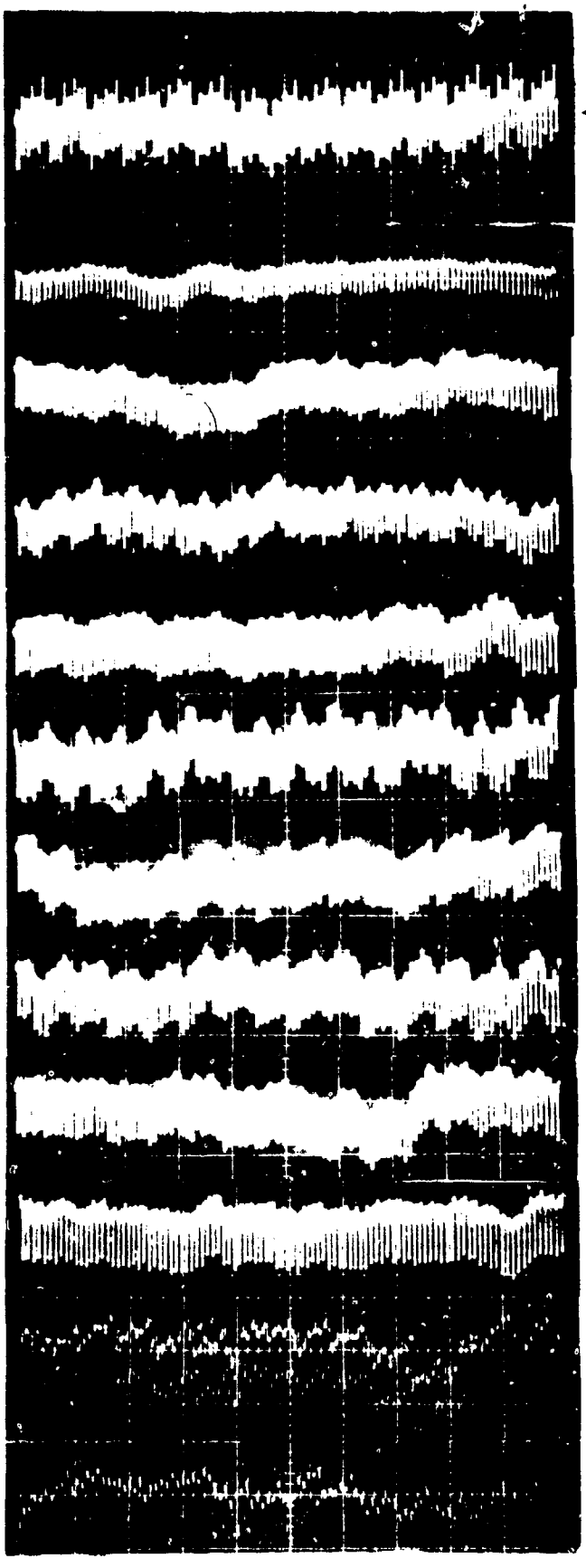

← 100% transmittance (no cloud)

time (min)	cw 10.6 μm (dB/m)	0.63 μm (dB/m)
5	2.00	14.7
19	0.80	12.3
21	0.80	11.3
25	0.67	9.0
28½	0.46	7.7
32	0.46	6.0
35	0.33	5.0
38½	0.46	4.0
43½	0.33	3.0
46	0.33	3.0
59½	0.13	2.0

PART D: THEORY AND LITERATURE SURVEY

Section D1. Scattering by Droplets

General theoretical treatises include books by Van de Hulst (D1), Deirmendjian (D2) and Kerker (D3). The Mie theory has also been discussed by Born and Wolf (D4). In the following curtailed analysis we closely follow Van de Hulst.

Let $E_\perp, E_\parallel$ denote the radiation electric fields respectively perpendicular and parallel to the plane containing the incident and scattered directions. Then for incident fields $E_{o\perp}, E_{o\parallel}$ of unit amplitude

$$E_\perp = S_1(\theta)\ \frac{e^{-ikr+i\omega t}}{ikr}\ ,\quad E_{o\perp} = e^{-ikz+\omega t}$$

$$E_\parallel = S_2(\theta)\ \frac{e^{-ikr+i\omega t}}{ikr}\ ,\quad E_{o\parallel} = e^{-ikz+\omega t} \qquad (D1)$$

where z is the the distance along the direction of the incident wave, r is the distance along the direction of scattering and θ is the angle of scattering. $S_1(\theta)$, $S_2(\theta)$ are complex amplitude functions.

On taking the squares of the moduli we obtain for polarisations perpendicular and parallel to the plane of scattering

$$I_\perp = \frac{i_1}{k^2 r^2} I_0 \quad ; \qquad I_\parallel = \frac{i_2}{k^2 r^2} I_0$$

$$i_1 = |S_1(\theta)|^2 \qquad i_2 = |S_2(\theta)|^2 \qquad (D2)$$

and for unpolarised light

$$I = \frac{\frac{1}{2}(i_1 + i_2)}{k^2 r^2} I_0 \qquad (D3)$$

The scattering cross section is an area of σ_{sca} such that the total power scattered into all directions equals $I_0 \sigma_{sca}$ Thus

$$\sigma_{sca} = k^{-2} \int \tfrac{1}{2}(i_1 + i_2)\, d\Omega = \int r^2 I\, d\Omega \qquad (D4)$$

For a medium with N equal size scatterers per unit volume, the intensity scattered in a direction making angle θ with the incident electric vector from a small volume ΔV is

$$I(\theta) = \frac{N \Delta V}{k^2 r^2} \left[\frac{i_1(\theta) + i_2(\theta)}{2} \right] I_0 \qquad (D5)$$

The power scattered into solid angle $\delta\Omega$ is $I r^2 \delta\Omega$, whilst the incident power is $A I_0 \delta\Omega_0$ where $\Delta V = A \Delta z$. In the case of a distribution of drop sizes, the power scattered into $\delta\Omega$ is

$$I r^2 \delta\Omega = I_0 \Delta V\ \delta\Omega\ k^{-2} \int \tfrac{1}{2} \{ i_1(\theta, a) + i_2(\theta, a) \}\ N(a)\, da \qquad (D6)$$

$$= I_0\ \Delta V\ \delta\Omega\ \beta(\theta)$$

where

$$\beta(\theta) = k^{-2} \int \tfrac{1}{2} \{ i_1(\theta,a) + i_2(\theta,a) \} N(a)\, da \qquad (D7)$$

Calculations by Deirmendjian (D5) for functions $P_1(\theta)$ and $P_2(\theta)$ which are proportional to $i_1(\theta)$ and $i_2(\theta)$ [$P(\theta) = 4 K_{sca}^{-1} a^{-2} i(\theta)$, where $K\pi a^2$ is the attenuation cross section (see below) and $a = ak$ with $k = 2\pi/\lambda$] are shown in figure D1 for an assumed distribution of droplet sizes of the form $a^6 \exp(-1.5a)$. The calculations for water droplets are done for wavelengths 0.70μm and 10.0μm. The solid curve is $P_1(\theta)$ and the dotted curve $P_2(\theta)$. Carrier et al (D6) have calculated the backscattering $\beta(\pi)$ for various cloud models. For example, the fair weather cumulus model having a total drop concentration of $300cm^{-3}$ and most probable radius 3.5μm yields $\beta(\pi) = 2.3 \times 10^{-5}\ m^{-1}\ sr^{-1}$ Suppose that a laser delivers power P_0 into a beam with solid angle of divergence $\delta\Omega_0$. Then a cloud at range z is subject to irradiance $I_0 = P_0/(\delta\Omega_0 A)$ over an area A where $A = z^2 \delta\Omega_0$. Let the backscattering be collected by a mirror of aperture S, so that $\delta\Omega = S/z^2$. Thus the power collected will be

$$\left(\frac{P_0}{\delta\Omega_0 A}\right) A\, \delta z \left(\frac{S}{z^2}\right) \beta(\pi) = P_0 \left(\frac{S}{A}\right) \delta z\ \beta(\pi) \qquad (D8)$$

Take $P_0 = 100MW$ and a beam divergence of 1mr. Then for a cloud at 10km range and $S \sim 10^4\ cm^2$ (~1m diameter mirror) we find, assuming $\delta z = 100m$ and $\beta(\pi) = 2.3 \times 10^{-5}\ m^{-1}\ sr^{-1}$, a returned power of 2.3kW.

Since $\Delta z \sim 1/\gamma$ where γ is the attenuation coefficient the backscattered signal is proportional to $\beta(\pi)/\gamma$, a quantity which should be sensitive to the modal radius of the drop size distribution. The possibility of obtaining information about drop sizes from backscatter measurements, possibly using two wavelengths (10.6μm and 0.63μm) deserves further investigation.

Section D2. Attenuation (Extinction) by Droplets

Consider the resultant amplitude due to scatterers in a slab of thickness δz normal to the direction of propagation. The slab is irradiated with a plane wave of unit amplitude, $\exp(-ikz + i\omega t) = E_0$. At a point P distant z ahead of the slab the total field (including also the incident field) is given by

$$\begin{aligned} E &= e^{-ikz + i\omega t} + \int_{-\infty}^{+\infty}\int_{-\infty}^{+\infty} \frac{S(\theta) e^{-ikr + i\omega t}}{ikr} N\, dx\, dy\, dz \\ &= E_0 \left\{ 1 + \iint \frac{S(\theta)\, e^{-ik(x^2+y^2)/2z}}{ikr} N\, dx\, dy\, dz \right\} \end{aligned} \qquad (D9)$$

where we use

$$r \simeq z + (x^2+y^2)/2z \qquad (z \gg x, y) \qquad (D10)$$

Performing the integration over dxdy with the help of

$$\int_{-\infty}^{+\infty} e^{bx^2} dx = \sqrt{\frac{\pi}{b}} \tag{D11}$$

and with the approximations $S(\theta) \simeq S(0)$ and $z \simeq r$, we find

$$E = E_0 \{ 1 - 2\pi k^{-2} N S(0) \delta z \} \tag{D12}$$

Now if one attributes to the medium a complex refractive index,

$$\tilde{n} = n - in' \tag{D13}$$

then propagation over δz multiplies the wave by the factor

$$e^{-ik\delta z(\tilde{n}-1)} \simeq 1 - ik\,\delta z(\tilde{n}-1) \tag{D14}$$

and this describes what we have found in (D12) if

$$ik\,\delta z(\tilde{n}-1) = 2\pi k^{-2} N S(0) \delta z$$

or

$$\tilde{n} = 1 - 2\pi i k^{-3} N S(0) \tag{D15}$$

Thus after distance z the wave has amplitude

$$E = e^{-ik\tilde{n}z + i\omega t} = e^{-kn'} e^{-iknz + i\omega t} \tag{D16}$$

and since $I \propto E^2$ the attenuation coefficient γ of the medium is given by

$$\gamma = 2kn' = 2k\,\Im[2\pi i k^{-3} N S(0)] \tag{D17}$$

$$= 4\pi k^{-2} \mathcal{R}[S(0)]$$

From γ we define an attenuation cross section σ and an efficiency factor K by means of

$$\gamma = N\sigma \; ; \quad \sigma = \pi a^2 K \tag{D18}$$

so that

$$K = 4a^{-2} \mathcal{R}[S(0)] \qquad a = ak \tag{D19}$$

where a is the drop radius and πa^2 the geometrical cross section. σ includes a contribution from forward scattering.

The Mie calculation for $S(0)$ yields the function $K(a)$ shown in figure D2. Note that $K(a) \longrightarrow 2$ for large a. The doubling of the geometrical shadow is due to diffraction (D1,D7). The cross section for absorption σ_{abs} will be given by

$$\sigma_{abs} = \sigma - \sigma_{sca} \tag{D20}$$

where σ is given by eq.(D18) and σ_{sca} is given by eq.(D4). The relative contributions of absorption and scattering to attenuation at 10.6μm as a function of drop radius are shown in figure D3. Three standard drop size distributions yield the attenuation and scattering coefficients shown in figure D4 after Deirmendjian (D2).

Section D3. Mie Calculation

For the complex amplitude functions $S_1(\theta)$ and $S_2(\theta)$ the rigorous Mie calculation for homogeneous spheres yields

$$S_1(\theta) = \sum_{n=1}^{\infty} \frac{2n+1}{n(n+1)} \left\{ a_n \pi_n(\cos\theta) + b_n \tau_n(\cos\theta) \right\}$$

$$S_2(\theta) = \sum_{n=1}^{\infty} \frac{2n+1}{n(n+1)} \left\{ b_n \pi_n(\cos\theta) + a_n \tau_n(\cos\theta) \right\} \tag{D21}$$

where the functions $\pi_n(\cos\theta)$ and $\tau_n(\cos\theta)$ are defined in terms of ordinary Legendre polynomials $P_n(\cos\theta)$ by

$$\pi_n(x) = \frac{d}{dx} P_n(x)$$

$$\tau_n(x) = x\,\pi_n(x) - (1-x^2)\frac{d}{dx}\pi_n(x) \tag{D22}$$

and where a_n and b_n are coefficients determined by the constants $\tilde{n}$ and a. If we write $\bar{a} = \tilde{n}a$ then

$$a_n = \frac{S_n'(\bar{a})S_n(a) - \bar{a}\,S_n(\bar{a})S_n'(a)}{S_n'(\bar{a})\Phi_n(a) - \bar{a}\,S_n(\bar{a})\Phi_n'(a)}$$

$$b_n = \frac{\bar{a}\,S_n'(\bar{a})S_n(a) - S_n(\bar{a})S_n'(a)}{\bar{a}\,S_n'(\bar{a})\Phi_n(a) - S_n(\bar{a})\Phi_n'(a)} \tag{D23}$$

with

$$S_n(a) = \left(\tfrac{1}{2}\pi a\right)^{\frac{1}{2}} J_{n+\frac{1}{2}}(a)$$

$$\Phi_n(a) = \left(\tfrac{1}{2}\pi a\right)^{\frac{1}{2}} H^{(2)}_{n+\frac{1}{2}}(a) \tag{D24}$$

where $J_{n+\frac{1}{2}}(x)$ is a Bessel function and $H^{(2)}_{n+\frac{1}{2}}(x)$ a Hankel function.

Section D4. Rayleigh Approximation ($ak \ll 1$)

When $a \ll \lambda$ (or $a \ll 1$) the scatterer radiates like a dipole of moment εE_0. For the direction of polarisation normal to the scattering plane the dipole moment is εE_0, whereas for the direction of polarisation in the plane of scattering it is $\varepsilon E_0 \cos\theta$. Hence

$$I = \frac{(1 + \cos^2\theta)\, k^4 |\alpha|^2}{2r^2} I_0 \qquad (D25)$$

Putting $\theta = 0$ and comparing with eq. (D2) we find

$$S(0) = ik^3\alpha \qquad (D26)$$

The polarisation of the drop is α/V where V is the volume of the drop, and hence

$$\frac{\tilde{n} - 1}{4\pi} = \frac{\alpha}{V} = \frac{S(0)}{ik^3V} \qquad (D27)$$

where $\tilde{n}$ is the complex refractive index of water at the frequency considered.

From eqs. (D18) and (D19) we find for the absorption cross section of the droplet

$$\begin{aligned} \sigma_{abs} &= \kappa\pi a^2 = 4\pi k^{-2} \mathcal{R}[S(0)] \\ &= -Vk\,\mathcal{I}[\tilde{n}^2 - 1] = 2kVn'n \\ &= \kappa V \end{aligned} \qquad (D28)$$

where $\kappa = 2kn'n$ is the absorption coefficient of liquid water. For a cloud of drops with concentration N the attenuation coefficient is given by

$$\begin{aligned} \gamma_{abs} &= \int \sigma(a) N(a)\, da = K \int V(a) N(a)\, da \\ &= \kappa(\Delta\rho/d) \end{aligned} \qquad (D29)$$

where $\Delta\rho$ is the mass of water per unit volume of cloud and d is the mass of water per unit volume of water.

This formula is appropriate for absorption of 10.6μm by clouds whose drops are optically thin. Using the data of Centeno (D8) for the refractive index of water at 10.6μm,

$$\tilde{n} = 1.175 + i(0.0802) \qquad (D30)$$

we obtain for the absorption coefficient of liquid water the result

$$\kappa = 2kn'n = 1.12 \times 10^3 \text{ cm}^{-1} \qquad (D31)$$

Thus drops are optically thin provided that $2a < 17.2\mu m$. Under these conditions the power extracted from the laser beam is proportional to the volume of a drop, and eq. (D29) is then valid. Physically this means that the absorption of a cloud is the absorption of the equivalent thin layer of water. When $a < 2\mu m$ (figure D3) scattering will be small compared to absorption and we may write $\gamma \sim \gamma_{abs}$. Substituting eq. (D31) into (D29) one finds that $\gamma_{abs} = 0.112\ m^{-1}$ for $\Delta\rho = 1\ g\ m^{-3}$, which corresponds to 0.4 dB km^{-1} per g m^{-3} of liquid water. Rensch and Long (D9) mention that all distribution models with most probable radius

between 0.3μm and 2.0μm predict 0.4 $(dB\ m^{-1})(g\ m^{-3})^{-1}$ for 10.6μm attenuation, so that this wavelength is suitable for measurement of liquid water content of clouds. The experimental results described in Section C bear out this conclusion.

From eqs. (D4) and (D25)

$$\sigma_{sca} \approx \tfrac{8}{3}\pi k^4 |\varepsilon|^2 = k^4 V^2 (n^2-1)^2/6\pi \tag{D32}$$

In the case when there are N scatterers per unit volume which are spaced by distances small compared to a wavelength we can write

$$\varepsilon N = \frac{\tilde{m}^2 - 1}{4\pi} \tag{D33}$$

where $\tilde{m}$ is the complex refractive index for the cloud (as opposed to $\tilde{n}$ which is for liquid water). Now substitution into eq. (D32) yields

$$\sigma_{sca} = \tfrac{8}{3}\pi k^4 |\varepsilon|^2$$

$$= \frac{8\pi^3}{3\lambda^4}\frac{(n^2-1)^2}{N^2} \tag{D34}$$

Section D5. Diffraction Approximation ($ak \gg 1$)

When an object is viewed from a distance z which is large enough for the object to be well within the central Fresnel zone (radius $\sqrt{\lambda z}$), then the amplitude at the viewing point P is given by

$$E = e^{-ikz+i\omega t} - \frac{ie^{i\omega t}}{r\lambda} e^{-ikr} \iint e^{-ik(x\cos\phi + y\sin\phi)\sin\theta}\, dx\, dy \tag{D35}$$

where r, θ, φ are polar coordinates of P referred to axes with origin in the particle and with x-y plane normal to the incident light. (The distance from P to a general point (x, y, 0) on the particle's plane is $r - (x\cos\phi + y\sin\phi)\sin\theta$). The form of eq. (D35) is that of (D1) for a single particle if

$$S(\theta,\phi) = \frac{k^2}{2\pi} A D(\theta,\phi) \tag{D36}$$

with

$$A D(\theta,\phi) = \iint e^{-ik(x\cos\phi + y\sin\phi)\sin\theta}\, dx\, dy \tag{D37}$$

where A is the area of the shadow. From eq. (D3) the scattered intensity is given by

$$I = \frac{A^2 \{D(\theta,\phi)\}^2}{\lambda^2 r^2} I_0 \tag{D38}$$

Since $D(0,\phi) = 1$, eqs. (D18) and (D19) yield

$$\sigma = (\pi a^2)(4a^{-2})\left(\frac{K^2}{2\pi}\right)A = 2A \tag{D39}$$

which confirms that diffraction doubles the geometrical cross section.

For a sphere the function $D(\theta,\phi)$ can be evaluated to

$$D(\theta,\phi) = \frac{2J_1(a\sin\theta)}{a\sin\theta} \qquad a = ak \tag{D40}$$

where J_1 is a Bessel function of the first kind. The first dark ring of this well-known diffraction pattern occurs at

$$a\sin\theta = 3.83 \tag{D41}$$

Now

$$S_1(\theta) = S_2(\theta) = a^2\,\frac{J_1(a\sin\theta)}{a\sin\theta} \tag{D42}$$

For the relative intensities of the first and second diffraction rings relative to the central maximum see figure D5.

Section D6. Natural Fogs and Clouds

The analysis given by Wright (D10) seems to describe the situation most succinctly. For the drop size distribution a gamma function distribution law (D2) is assumed:

$$N(a)da = \frac{N\mu^{\mu+1}}{\Gamma(\mu+1)}\left(\frac{a}{a_0}\right)^{\mu}\exp\left(-\frac{\mu a}{a_0}\right)d\left(\frac{a}{a_0}\right) \tag{D43}$$

where $\Gamma(\mu+1)$ is the complete gamma function, N is the total drop concentration, a is the drop radius, a_0 the most probable radius, and μ is the width parameter. At large radii this reduces to the Junge distribution law.

The total volume of liquid water per unit volume of cloud is given by

$$\begin{aligned} q &= \tfrac{4}{3}\pi\int_0^{\infty} a^3 N(a)da \\ &= \tfrac{4}{3}\pi a_0^3\,\frac{(\mu+1)(\mu+2)(\mu+3)}{\mu^3}\,N \end{aligned} \tag{D44}$$

The attenuation (extinction) coefficient for a particular wavelength is given by

$$\gamma = N\int_0^{\infty}\pi a^2 K(a,\tilde{n})\,N(a)da \tag{D45}$$

where $\tilde{n}$ is the complex refractive index of water. The exact Mie calculation of $K(a,\tilde{n})$ is complicated and tedious but for refractive index (D30) we may use the Van de Hulst approximation

$$K(a,\tilde{n}) = 2 - \frac{4}{\eta}\cos g\, e^{-\eta\tan g}\sin(\eta-g) + \frac{4}{\eta^2}\cos^2 g\left\{\cos 2g - e^{-\rho\tan g}\cos(\rho-2g)\right\} \quad (D46)$$

where

$$\tilde{n} = n - in'$$

$$\tan g = \frac{n'}{n-1} \qquad \eta = 2a(n-1) \quad (D47)$$

The approximation is valid for $\eta \ll 1$ and a correction factor has been applied by Deirmendjian (D2). On this basis Wright obtains the attenuation coefficients for 1.06μm and 10.6μm radiations which are shown in figure D6 as a function of a_0. The attenuation coefficients are plotted for three values of μ and are not particularly sensitive to μ.

For large a $(=ak)$ the simple assumption

$$K(a,\tilde{n}) \longrightarrow 2 \quad (D48)$$

can be made, in which case eq. (D45) integrates up to

$$\gamma = 6\pi a_0^2 N \quad (D49)$$

Measurements of attenuations at 1.06μm and 10.6μm are used by Wright first to infer a mode radius a_0 from the ratio $\gamma(1.06)/\gamma(10.6)$ by reference to figure D6. Then 10.6μm attenuation establishes $\Delta\rho = qd$ by eq. (D29), and from q one finds N by use of (D44).

Use of eq. (D49) in (D44) yields

$$\Delta\rho = qd = \frac{2a_0}{9}\gamma d\,\frac{(\mu+1)(\mu+2)(\mu+3)}{\mu^3} \quad (D50)$$

This differs from (88) by the factor $(\mu+1)(\mu+2)(\mu+3)/3\mu^3$ on the left hand side; for $\mu = 2$ the factor is 2.5, for $\mu = 4$ it is 1.1 and for $\mu = 6$ it is 0.8.

Section D7. Experimental Observations

A general view of the literature up to 1972 has been given by Vatsia (D11).

The first extensive work on transmittance of natural fogs to radiation in the spectral band 0.35 – 10 μm was carried out by Arnulf et al (D12). Figure D7 summarises the results.

Gates and Shaw (D13) measured the transmittance of various clouds to sun-

light between 0.48μm and 12μm, concluding that the transmittance is consistently higher in the 8.0 to 12.0 μm region than in the 0.48 to 5.0μm region.

Kurnick et al (D14) have reported transmittance of rain, snow, sleet, freezing fog and fog in Chicago to 1 - 11μm radiations - see figure D8.

Johnson and Burch (D15) investigated the transmittance of artificial fogs at wavelengths 0.434, 1.01, 3.5, 10.0, 13.5 and 345 μm. The fogs were generated by spraying liquid nitrogen into the top of a chamber containing air saturated by contact with water at the bottom of the chamber slightly above room temperature. Figure D9 summarises the results.

Chu and Hogg (D16) have measured attenuations of natural fogs and rain over a 2.6km path for various laser beams (He-Ne at 0.63μm, He-Xe at 3.5μm, and CO_2 at 10.6μm). Fogs attenuated 10.6μm radiation least, whilst rain attenuated 0.63μm radiation least. Fogs containing 0.1 g m^{-3} of water attenuated 10.6μm radiation by 15 dB km^{-1}, whist rain at 25 mm h^{-1} (1 g m^{-3}) produced 12.5 dB km^{-1} (figure D10).

Rensch and Long (D9) measured attenuation by very light fog and by rain of 0.63μm and 10.6μm laser beams. For rain at 24 mm h^{-1} they find attenuations of about 10 dB km^{-1} for both beams.

Sanders and Selby (D17) have measured attenuations by dense natural clouds at several laser wavelengths - 0.63, 1.15, 3.39μm (He-Ne), 10.6μm (CO_2), and 337μm (CN). Clouds were sampled with a 4-stage Casella impactor; distributions had mode radii in the range 1.6 to 4.5μm and the total drop concentrations ranged from about 200 to 2500 cm^{-3} (the liquid water contents being in the range 0.03 to 0.4 g m^{-3}). The measurements were made at Great Dun Fell, Cumbria, a site (at altitude 2780 feet) where visibility was less than 200m for 264 days during the year 1966 at 9 a.m. They state that the absence of large drops (20 - 100μm) might be expected at the base of stratus clouds where drops are at an early stage of evolution. Attenuation at 10.6μm (over a 90m path) was compared with attenuation at 0.63μm (over a 45m path). Expressing the attenuations in dB km^{-1} the former was always less than the latter, the ratio varying from 0.31 to 0.64, corresponding to a range of 10.6μm attenuation coefficient 9.5 - 45.8 dB km^{-1} (figure D11)

Wright (D10) reports observations with a transmissometer which operates continuously and automatically over a path of 560m at wavelengths 0.63μm 1.06 μm and 10.6μm. Figure D12 compares attenuation coefficients for 10.6μm and 1.06μm beams over the month of May, 1975. Figure D13 shows attenuations vs. time during a fog on May 9, 1975.

With regard to backscatter and lidar Collis (D18,19) has reviewed the potential use for atmospheric probing. Backscatter measurements have been made by Fiocco and Smullin (D20), Rensch and Long (D21), Brandewie and Davis (D22) and Hughes et al (D23). Clemesha et al (D24) describe a laser radar system for atmospheric studies. Herman et al (D25) prop-

ose a bistatic lidar which would enable aerosol size distributions to be inferred from polarisation measurements. ee also Barrett and Ben-Dov (D26).

Section D8. Cloud Clearing

A drop of radius $a(t)$ at time t gradually shrinks as it evaporates. In a radiation flux F this shrinkage is given by

$$a(t) = a(0)\ e^{-\frac{t}{\tau}} \qquad (D51)$$

$$\tau F = \frac{3\eta H d}{\kappa} = 10\ J\ cm^{-2}$$

where H is the heat required to convert unit mass of water at room temperature into vapour and η is a factor which accounts for loss of heat to the medium. Analysis of cloud clearing by laser beams sufficiently intense to evaporate drops has been made by Glickler (D27), also Lamb and Kinney (D28) and Sukhroukov et al (D29).

Measurements of the clearing due to a CW 10.6μm beam, as monitored by the change in transmittance for a collinear 0.63μm beam, have been made by Mullaney et al (D30). Figure D14 shows how transmittance varies with time after switching on the 10.6μm beam. The ultimate steady-state transmittance is less than the peak value reached some 0.5s after switch-on (for beams with power density between 5 and 50 W cm^{-2}) because of the onset of convection which draws drops into the cleared channel. They measure 1 - 10 cm s^{-1} for the velocity of the convection and find 0.1 - 1.0 K for the temperature rise of the ascending air immediately above the beam. Their clouds are produced by introducing steam into a chamber (0.83m long) refrigerated to 275K. They estimate drop radii in the 2 - 7μm range, and concentrations between 10^3 and 10^4 cm^{-3}. The product $F\tau$ was found to be constant as F is varied, in agreement with eq. D51, and they obtain 28 ± 4 J cm^{-2} for its value, implying that $\eta \approx 3$.

In the case of TEA laser pulses there is insufficient time for loss of heat to the medium, implying that $\eta \approx 1$ in eq.D51. Moreover the heating is sufficiently rapid (a few tenths of a microsecond) for the material of the drop to be inertially confined. The evaporation may then take the form of a micro-explosion after the radiation pulse has passed, which would change the parameters of the medium only for a subsequent pulse. The threshold energy density of 10 J cm^{-2} can be exceeded by optical condensation of the 20 cm^2 beam of our TEA laser, but it will be necessary to limit the beam divergence to less than 1mr by use of an unstable resonator before tests of these nonlinear effects can be carried out for our laboratory clouds.

In some elegant experiments Kafalas has examined the behaviour of single drops irradiated with a focused TEA laser pulse (power density only 10 MW cm^{-2}, however). Photomicrographs of the droplet were obtained by Kafalas and Ferdinand (D31) (i) before the pulse, (ii) 0.9μs after the pulse and(iii) 2.3μs after the pulse. The drop was positioned at the focus of three microscopes illuminated by 20ns sparks in succession. Figure D15 shows their results. For optically thin drops the explosion is spherical, and they find 130 m s^{-1} (Mach 0.4 in air) for the vapour

front expansion of a 12 μm radius drop averaged over the first 1.3μs. For optically thick drops front surface explosion with rear surface spallation gave a "dumbbell" expansion; a shock initiated at the front surface travels through the drop to cause spallation at the rear surface.

Kafalas and Herrmann (D32) used a schlieren system to follow the expansion of the shock fronts. They observed (figure D16) (i) expansion of a shock front with velocity Mach 1 in air driven by a temperature step and (ii) an expanding sphere of water vapour behind the thermal shock. The velocity of the latter decreased from 130 m s^{-1} over the first 2 - 3 μs, to 15 m s^{-1} over the next 5 - 15 μs, and finally to 10 m s^{-1} over the last 16 - 37 μs of observation. The duration of the laser pulse was 0.175μs. They calculate that the energy dissipated in the explosion (0.11mJ) was comparable to the energy required to evaporate the drop (0.16mJ).

In view of the several orders of magnitude change in the absorption which occurs when water changes from liquid to vapour phase, it is of considerable interest to measure the shape of a TEA laser pulse with energy density greater than the evaporation threshold, 10 J cm^{-2}, and with duration short enough for at least partial inertial confinement. In 0.1μs an explosively evaporating drop will have expanded to radius ~13μm, whatever its initial radius. Does such a drop absorb like liquid water for the leading part of the pulse and as vapour for the following part? We plan to investigate this effect.

PART D REFERENCES

D1 H.C.Van de Hulst, Light Scattering by Small Particles, Wiley (New York: 1957)

D2 D.Deirmendjian, Electromagnetic Scattering on Spherical Polydispersions, Elsevier (New York: 1969)

D3 M.Kerker, The Scattering of Light, Academic Press (New York: 1970)

D4 M.Born and E.Wolf, Principles of Optics, Pergamon Press (New York: 1959) Ch.8

D5 D.Deirmendjian Scattering and Polarisation Properties of Water Clouds and Hazes in the Visible and Infrared, Appl. Opt. 3, 187 (1964)

D6 L.W.Carrier, G.A.Cato and K.J.von Essen, The Backscattering and Extinction of Visible and Infrared Radiation by Selected Major Cloud Models, Appl. Opt. 6, 1209 (1967)

D7 C.Bar-Isaac and A.Hardy, Simple Derivation of the Factor Two in Mie Theory, Am. J. Phys. 43, 275 (1975)

D8 M.Centeno V, The Refractive Index of Liquid Water in the Near Infrared Spectrum, J. Opt. Soc. Am. 31, 244, (1941)

D9 D.B.Rensch and R.K.Long, Comparative Studies of Extinction and Backscattering by Aerosols, Fog and Rain at 10.6μm and 0.63μm, Appl. Opt. 9, 1563 (1970)

D10 P.J.Wright, A Comparative Study of Atmospheric Transmission at Three Laser Wavelengths in Relation to the Meteorological Parameters, Research Report, Plessey Radar Ltd., Newport Road, Cowes, Isle of Wight, England

D11 M.L.Vatsia, Atmospheric Optical Environment, U.S.Army Electronic Command Research Report ECOM-7023 (1972)

D12 A.Arnulf, J.Bricard, E.Cure and C.Veret, Transmission by Haze and Fog in the Spectral Region 0.35 to 10 Microns, J. Opt. Soc. Am. 47, 491 (1957)

D13 D.M.Gates and C.C.Shaw, Infrared Transmission of Clouds, J. Opt. Soc. Am. 50, 876 (1960)

D14 S.W.Kurnick. R.N.Zitter and D.B.Williams, Attenuation of Infrared Radiation by Fogs, J. Opt. Soc. Am. 50, 578 (1960)

D15 D.R.Johnston and D.E.Burch, Attenuation by Artificial Fogs in the Visible, Near Infrared and Far Infrared, Appl. Opt. 6, 1497 (1967)

D16 T.S.Chu and D.C.Hogg, Effects of Precipitation on Propagation at 0.63, 3.5 and 10.6 Microns, Bell Systems Tech J. 47, 723 (1968)

D17 R.Sanders and J.E.A.Selby, Comparative Measurements of the Attenuation of Visible and Infrared Laser Radiation in Cloud, Technical Report of EMI Electronics Ltd., Feltham, England

D18 R.T.H.Collis, Lidar: A New Atmospheric Probe, Quart. J. Roy. Met. Soc. 92, 220 (1966)

D19 R.T.H.Collis, Lidar, Appl. Opt. 9, 1782 (1970)

D20 G.Fiocco and L.Smullin, Detection of Scattering Layers in the Upper Atmosphere (60 - 140 km) by Optical Radar, Nature 199, 1275 (1963)

D21 D.B.Rensch and R.K.Long, Comparative Studies of Extinction and Backscattering by Aerosols, Fog and Rain at 10.6μm and 0.63μm, Appl. Opt.9, 1563 (1970)

D22 R.A.Brandewie and W.C.Davis, Parametric Study of a 10.6μm Laser Radar, Appl. Opt. 11, 1526 (1972)

D23 A.J.Hughes, J.O'Shaughnessy and E.R.Pike, FM-CW Radar Range Measurement at 10 μm Wavelength, IEEE J. Quantum Electron. QE-8, 909 (1972)

D24 B.R.Clemesha, G.S.Kent and R.W.H.Wright, A Laser for Atmospheric Studies, J. Appl. Meteor. 6, 386 (1967)

D25 B.M.Herman, S.R.Browning and J.A.Reagan, Determination of Aerosol Size Distributions from Lidar Measurements, J. Atmos. Sci. 28, 763

D26 E.W.Barrett and O.Ben-Dov, Application of Lidar to Air Pollution Measurements, J. Appl. Meteor. 6, 500 (1967)

D27 S.L.Glickler, Propagation of a 10.6μm Laser Through a Cloud including Droplet Vapourisation, Appl. Opt. 10, 644 (1971)

D28 G.L.Lamb and R.B.Kinney, Evaporation of a Mist By Intense Light Beam, J. Appl. Phys. 40, 416 (1969)

D29 A.P.Sukhroukov, R.V.Kokhlov and E.N.Shumilov, Dynamics of Clearing Clouds with a Laser Beam, Zh ETF Pis. Red. 14, 245 (1971)

D30 G.J.Mullaney, W.H.Christiansen and D.A.Russell, Fog Dissipation Using a CO_2 Laser, Appl. Phys. Lett. 13, 145 (1968)

D31 P.Kafalas and A.P.Ferdinand Jr., Fog Droplet Vaporisation and Fragmentation by a 10.6μm Laser Pulse, Appl. Opt. 12, 29 (1973)

D32 P.Kafalas and J.Herrmann, Dynamics and Energetics of the Explosive Vaporisation of Fog Droplets by a 10.6μm Laser Pulse, Appl. Opt. 12, 772 (1973)

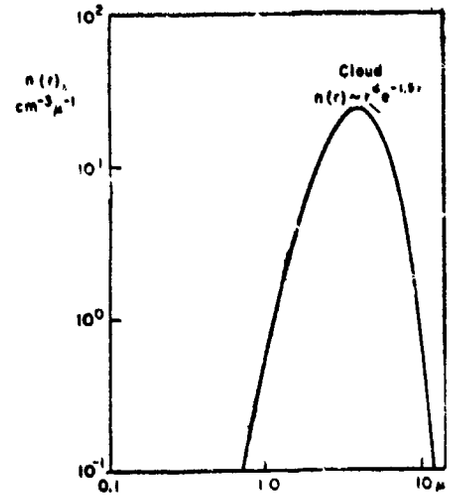

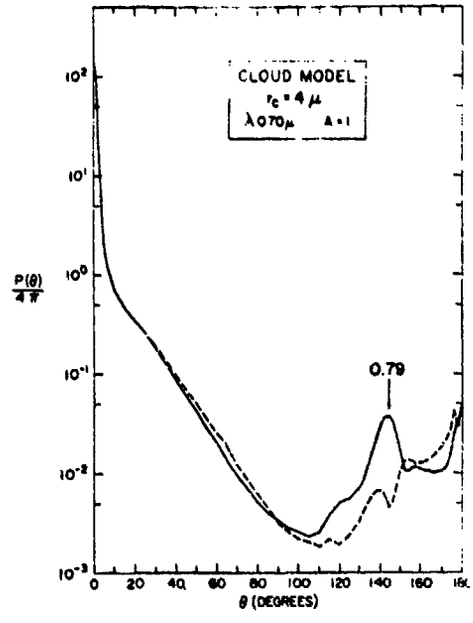

Same as Fig. 6 but at λ0.70 μ and real index 1.33. Computed values at θ: 0(1)10(5)130(2)180°.

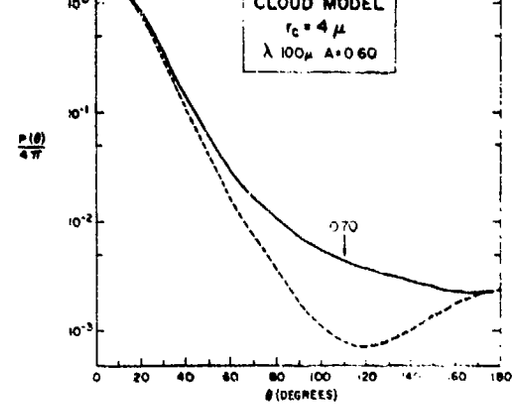

Fig. 6. Intensity functions for a water cloud illuminated by λ10.0-μ infrared radiation. Computed values at θ: 0(5)180°.

Figure D1: Normalized phase functions $P_1(\Theta)/4\pi$ (solid curve) and $P_2(\Theta)/4\pi$ (dotted curve) for scattering of (i) 0.70 μm and (ii) 10.0 μm radiations by the polydispersion shown, as calculated by D. Diermendjian (ref. D2). The cross section for scattering into solid angle $\delta\Omega$ in direction θ is $\sigma_{sca}\,\delta\Omega\,P(\theta)/4\pi$, where σ_{sca} is the total scatter cross section.

(After D.Deirmendjian, ref. D2)

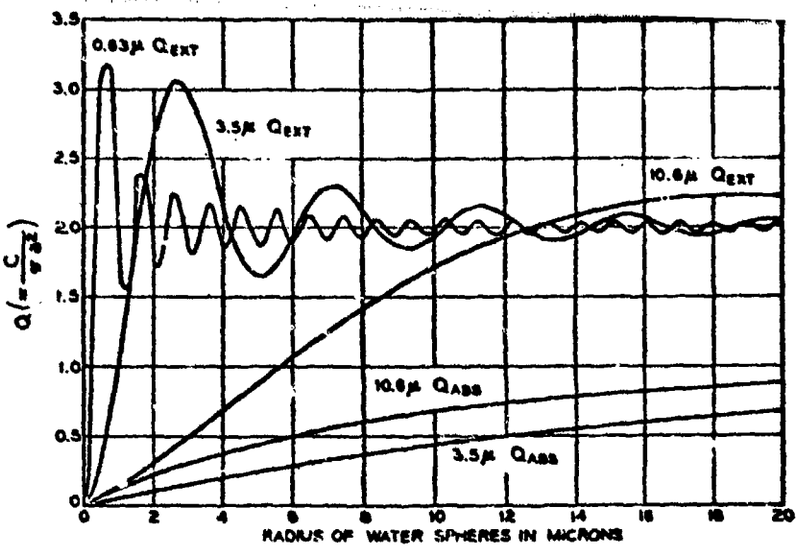

Approximate extinction and absorption cross sections.

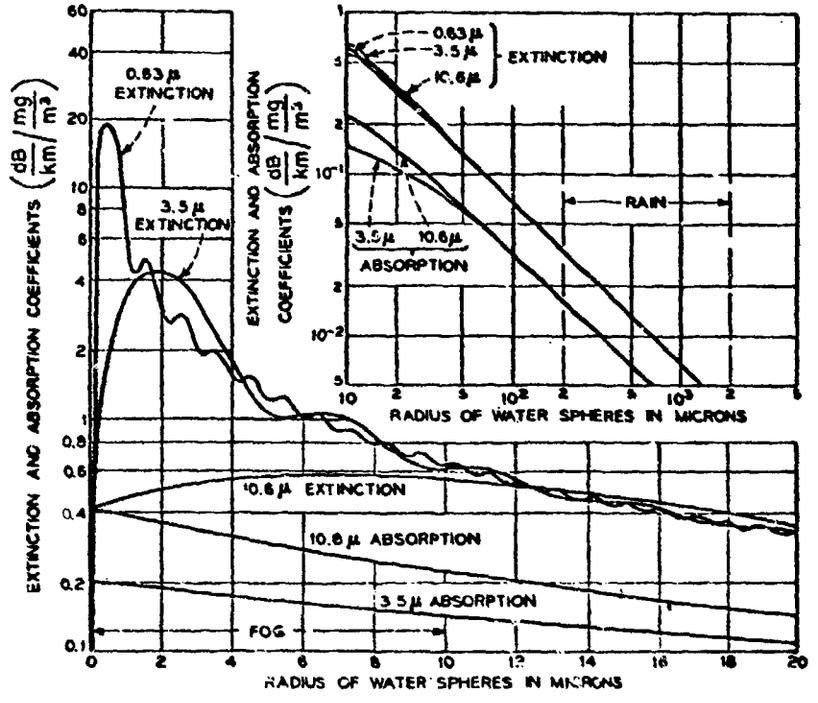

Extinction and absorption coefficients of precipitation with monodisperse drop-size distribution.

Figure D2: The Mie efficiency factor Q (or K) as a function of drop radius for different wavelengths.

Extinction and absorption coefficients (in db/m per g/m^3 of condensed water) for a monodispersion as a function of drop radius.

(After T.S. Chu and D.C. Hogg, ref. D16)

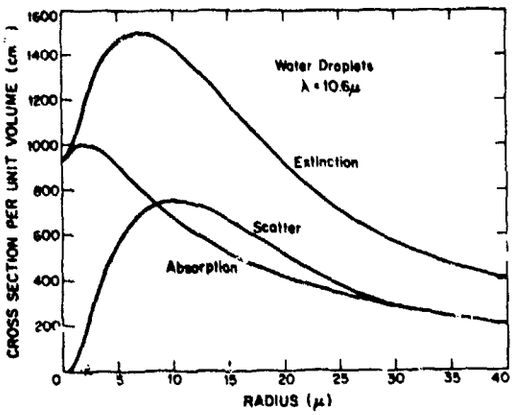

Figure D3: Attenuation, scattering, and absorption coefficients for unit volume of condensed water at wavelength 10.6 μm as a function of drop radius.

(After P. Kafalas and A.P. Ferdinand, ref. D31)

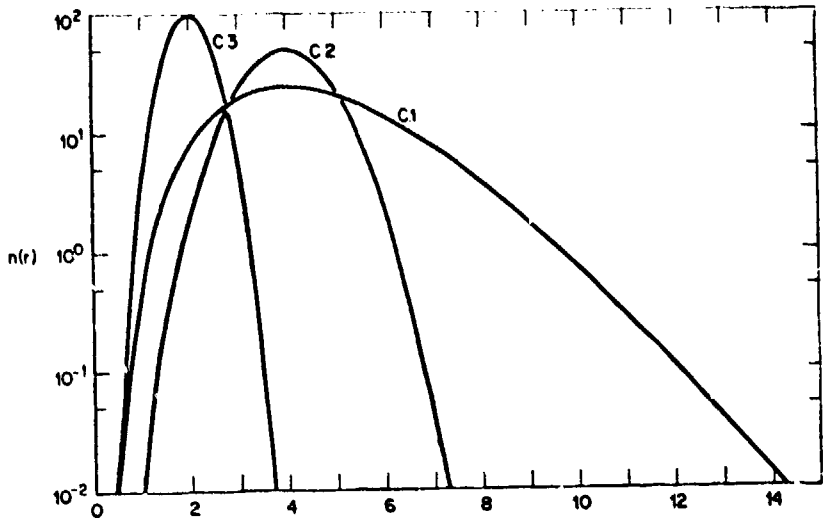

—Cloud-type distribution functions. The scale for the radius *r* is linear

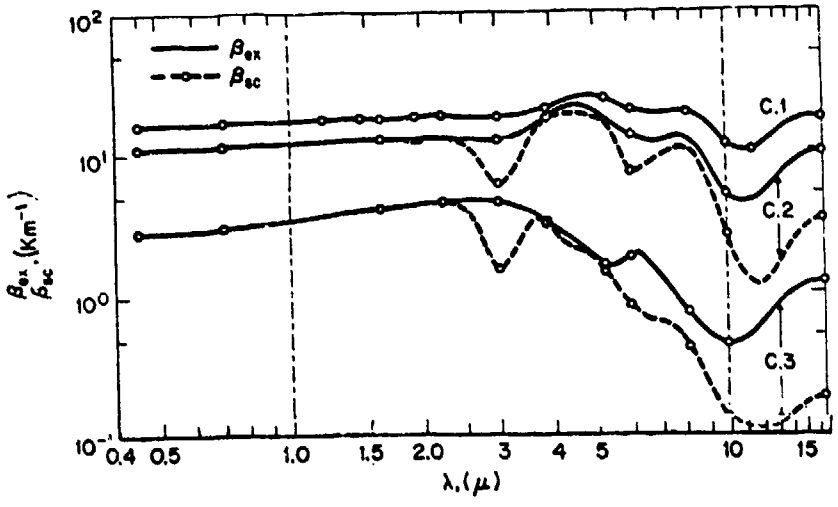

—Wavelength dependence of the volume extinction coefficient (solid line) and, in some cases, of the scattering coefficient (dashed line) for various distributions of *water spheres* equivalent to 100 particles per cm^3 in each case.

Figure D4: Attenuation (solid curve) and scattering (dashed curve) coefficients as functions of wavelength for cloud models C1, C2, and C3 normalized to 100 drops cm^{-3}.

(After D.Deirmendjian, ref. D2)

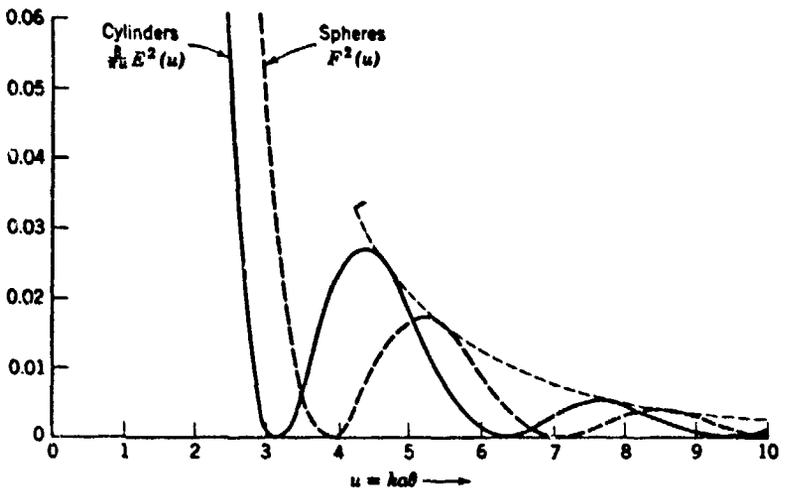

Relative intensities across first and second diffraction rings in the diffraction patterns of spheres and of randomly oriented cylinders, all with radius a.

Figure D5: Relative intensities of first and second diffraction rings with respect to the central maximum.

(After H.C. Van de Hulst, ref.D1)

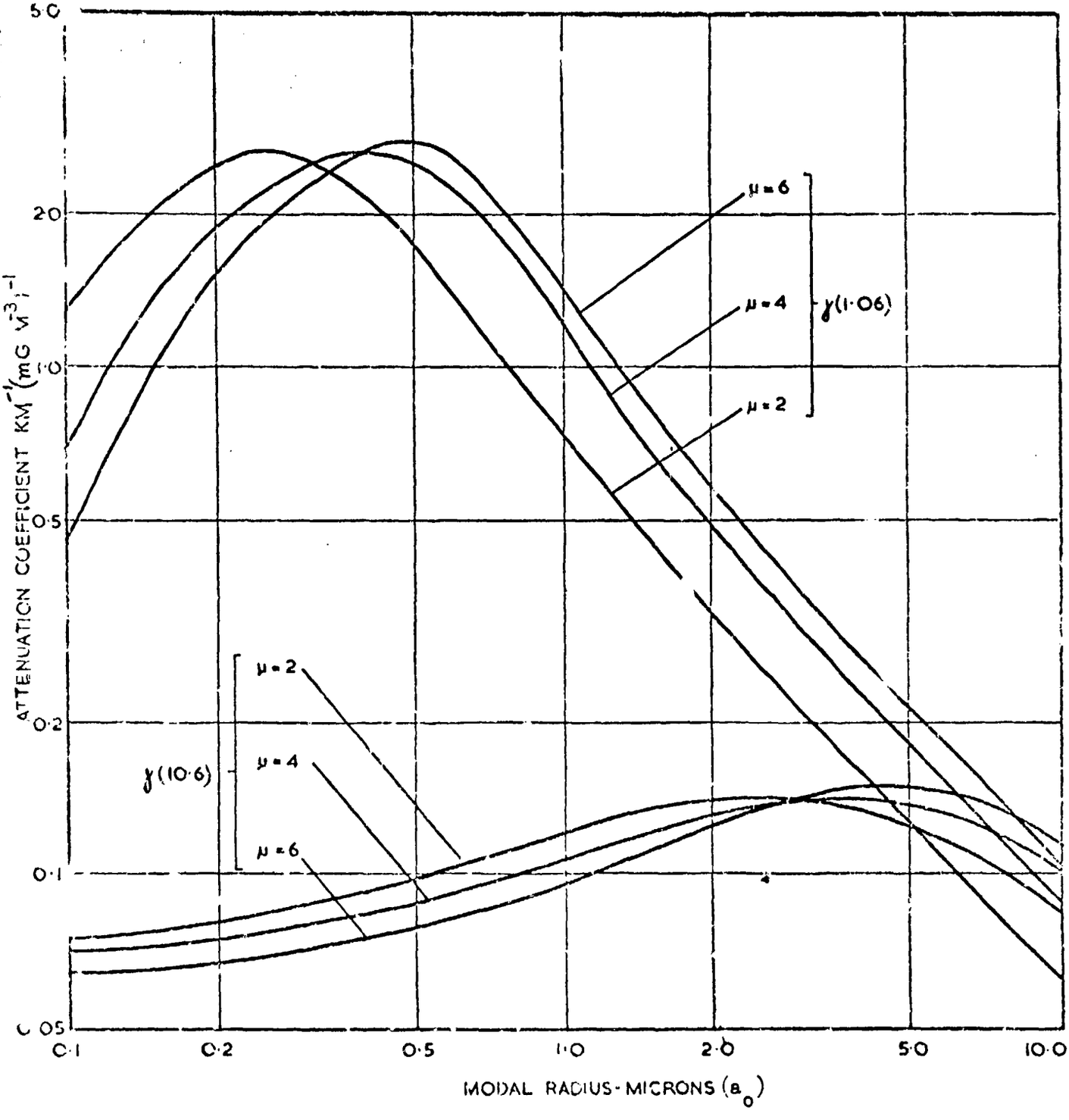

Figure D6: Theoretical attenuation coefficient at 1.06 μm and 10.6 μm versus modal radius (a_o) for various width parameters (μ)
(After P.J. Wright, ref. D10)

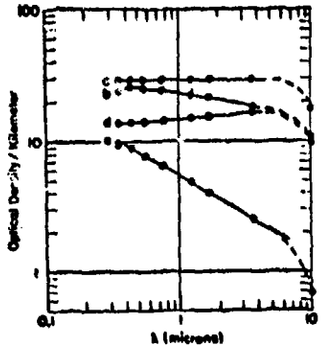

Optical transmission data for some fogs reported by Arnulf, Bricard, Curé, and Véret. The ordinate units are those of AIICV and differ from the units of the present work by the factor log$_e$.

FigureD7: Attenuation coefficient (x log$_e$) as a function of wavelength for natural fogs reported by ref. D9. (After Kurnick et al., ref. D14)

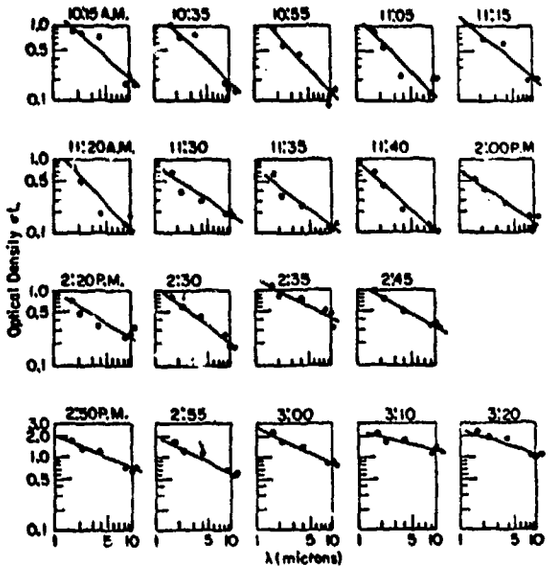

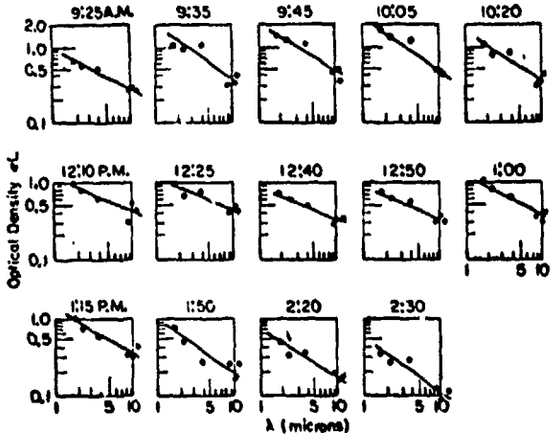

Optical transmission data obtained during a second fog.

Optical transmission data obtained during a fog. L is the path length (200 yards).

Figure D8: Optical thickness of two fogs at various time as a function of wavelength (After Kurnick et al., ref. D14)

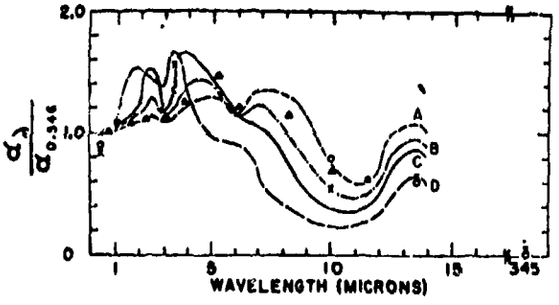

Ratio of attenuation coefficients $\alpha_\lambda/\alpha_{0.546}$ plotted against wavelength. O's and X's represent fog generation and fog dissipation, respectively. Two values for fog dissipation at 0.436 μ indicate that there are two drop size distributions as seen by this wavelength. The Δ's represent Diermendjian's theoretical calculations and are $\alpha_\lambda/\alpha_{0.55}$. The solid lines are theoretical curves of Zuyev *et al.*[8] for a drop size distribution given by $f(a) = 1/[\Gamma(\mu + 1)]\, r^{-\mu+1}\,(r^\mu/r)e^{-\mu r}$, where $r = a/r$, a is the radius of the drops, r is the most probable radius in the distribution, and μ is a parameter characterizing the distribution half-width. For curve *A*, $\mu = 2$, $r = 3$; curve *B*, $\mu = 2$, $r = 2$; curve *C*, $\mu = 10$, $r = 3$; curve *D*, $\mu = 10$, $r = 2$.

Figure D9: Attenuation coefficient (relative to that at a fixed wavelength of 0.546 m) as a function of wavelength for fogs A, B, C, D produced artificially. (After D.R. Johnston and D.E. Burch, ref. D15)

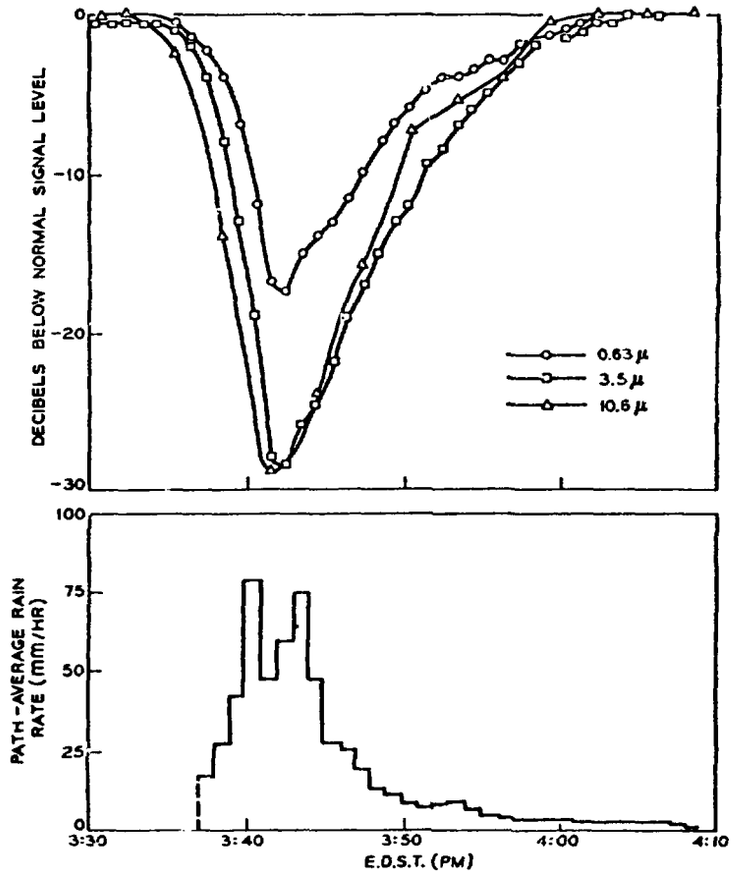

— Measured attenuation over 2.6 km during a rain shower on July 11, 1967. 0 dB-signal level in clear weather.

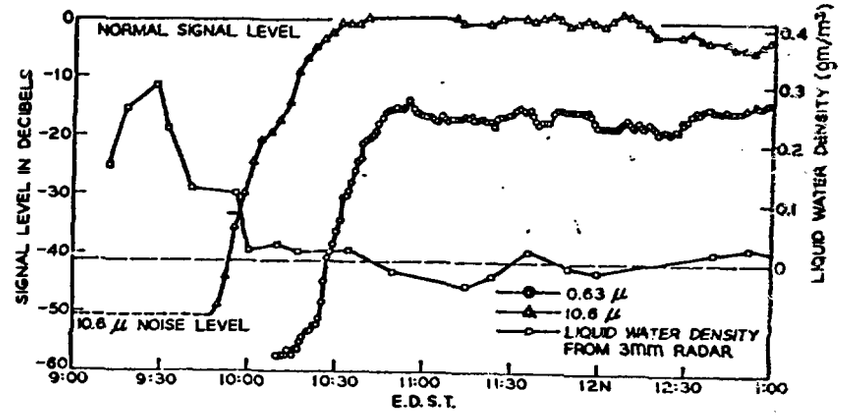

— Correlation between attenuation of laser beams and liquid water content measured by a 3 mm wavelength radar in fog.

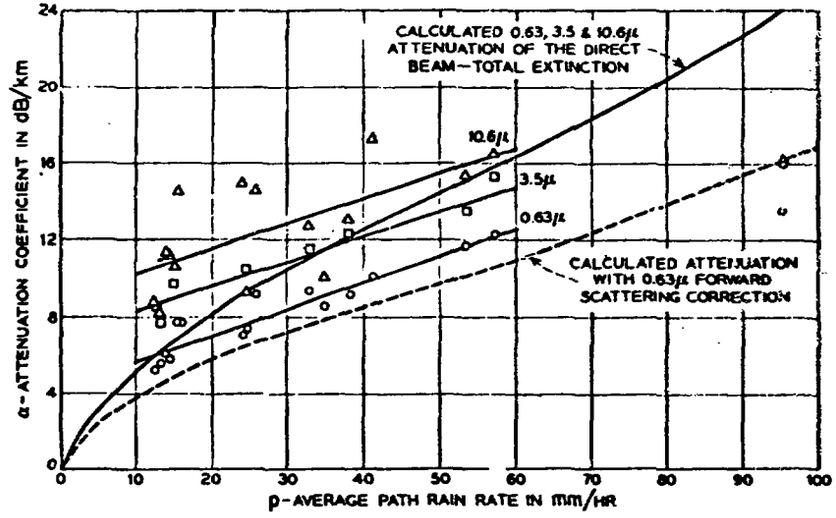

— Measured attenuation coefficients of a rain storm for a 2.6 km path.

Figure D10 Attenuation of laser beams at 0.63 μm, 3.5 μm , and 10.6 μm by fog and rain. (After T.S. Chu and D.C. Hogg, ref. D16) .

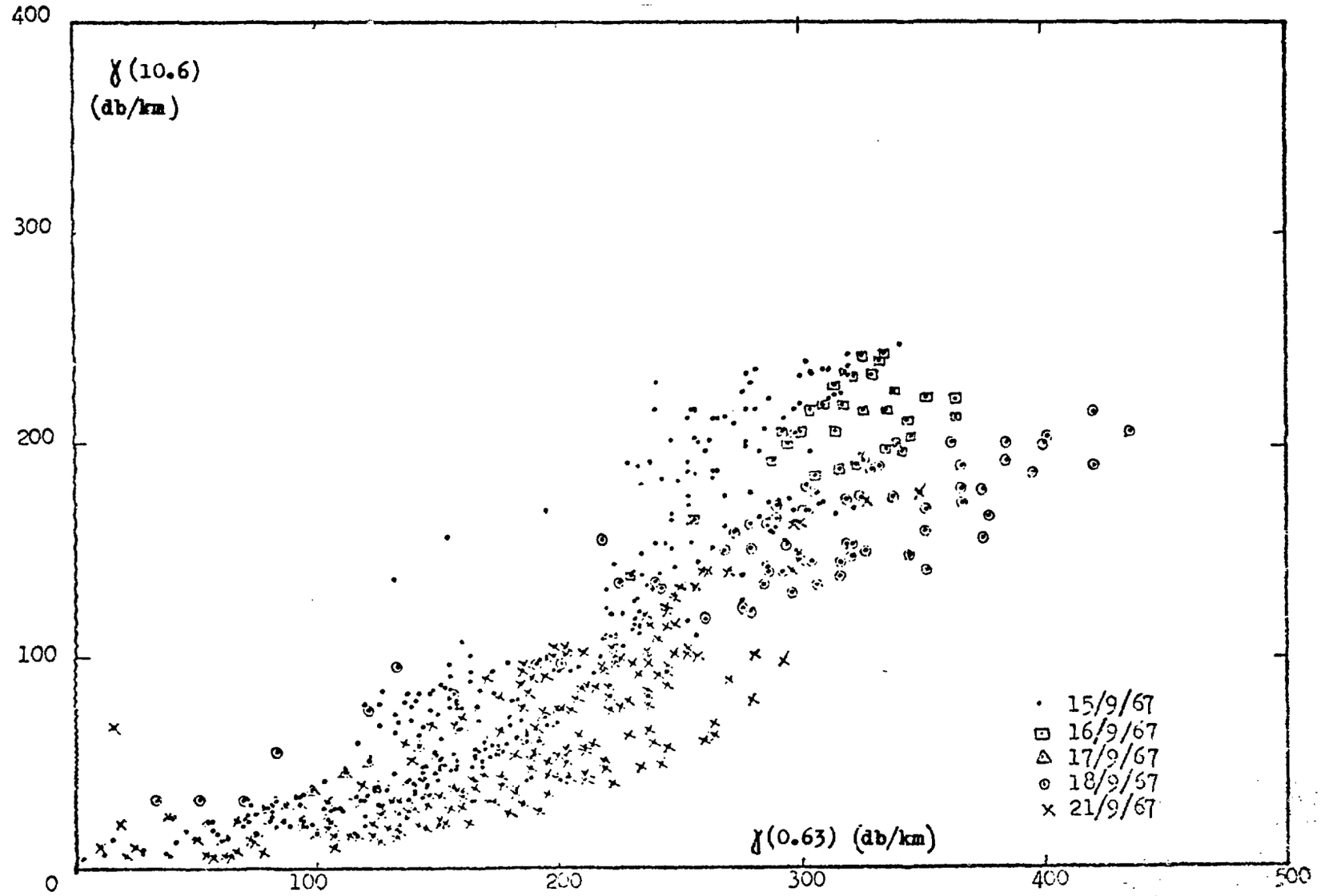

Figure D11: Attenuation coefficient at 10.6 μm versus attenuation coefficient at .63 μm for natural clouds with modal radius of drops between 2 and 3 μm

(After R. Sanders and J.E.A. Selby, ref. D17)

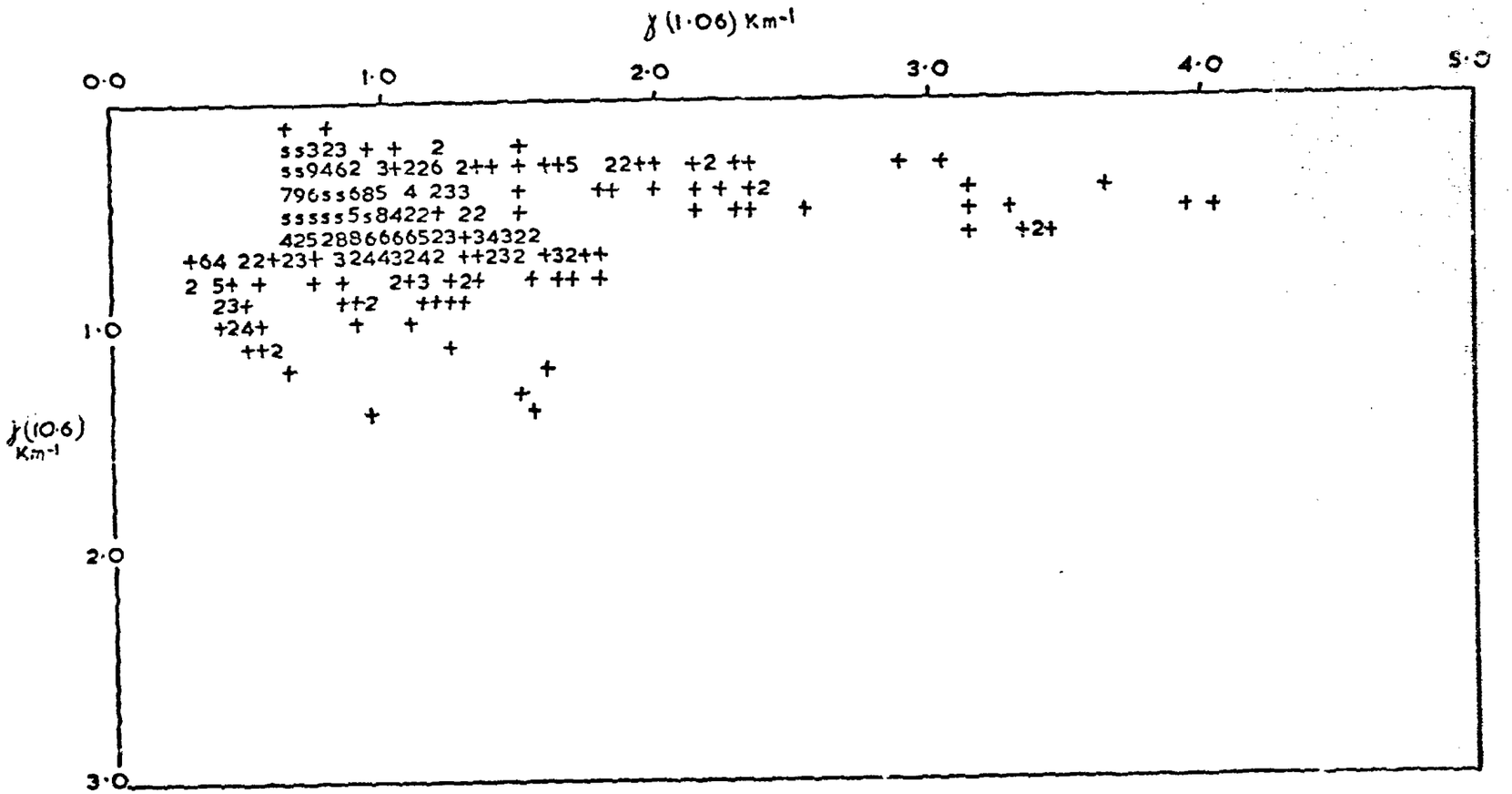

Figure D12: Measured attenuations during May 1975 at 10.6 μm and 1.06 μm under all atmospheric conditions (After P.J. Wright, ref. D10[1]

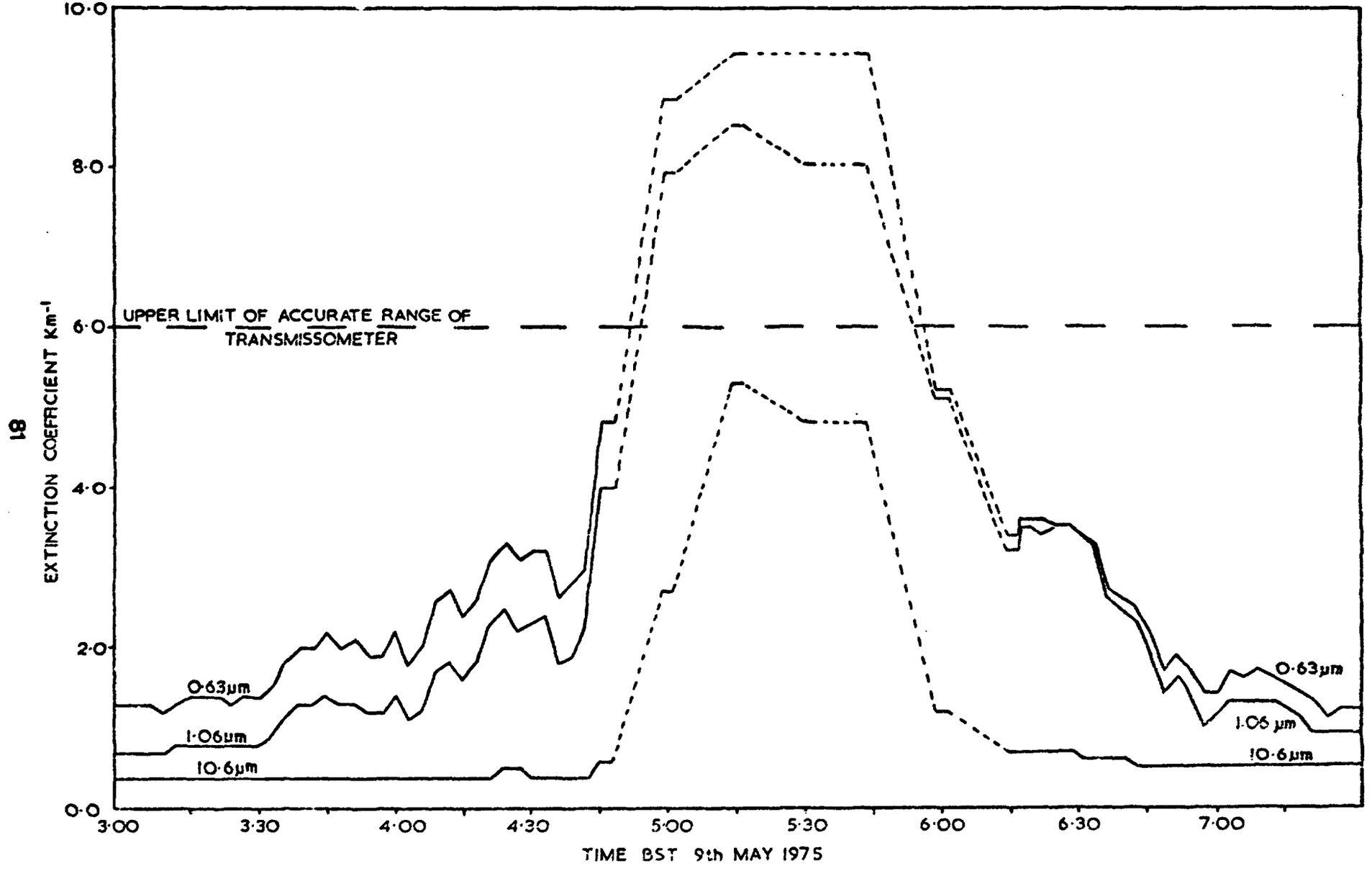

Figure D13: Attenuations at 0.63 μm , 1.06 μm, and 10.6 μm versus time for the fog of May 9, 1975 (After P.J. Wright, ref. D10)

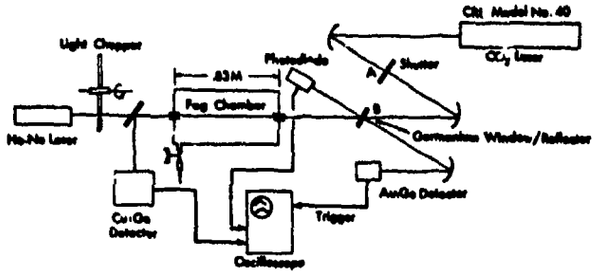

Experimental arrangement for fog dissipation measurements.

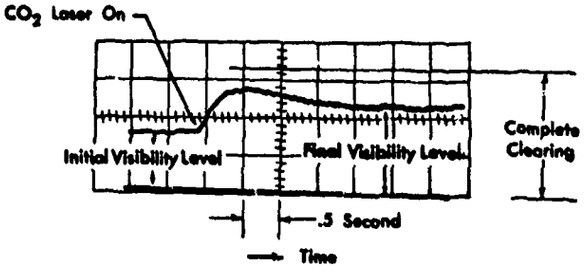

Output of the visibility probe (He-Ne beam).

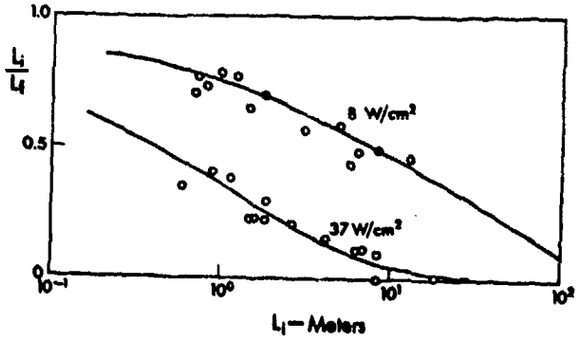

Clearing effectiveness of the CO_2 laser as a function of initial characteristic length.

Figure D14: Variation of transmittance of 0.63 μm beam through a laboratory fog due to drop evaporation by a coincident 10.6 μm beam with power density between 5 and 50 W/cm^2. L is reciprocal attenuation coefficient or optical depth, deduced from measured I(z)/I(0)

(After Mullaney et al., ref D30)

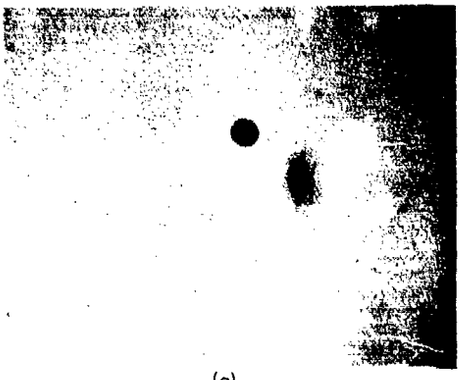

(a)

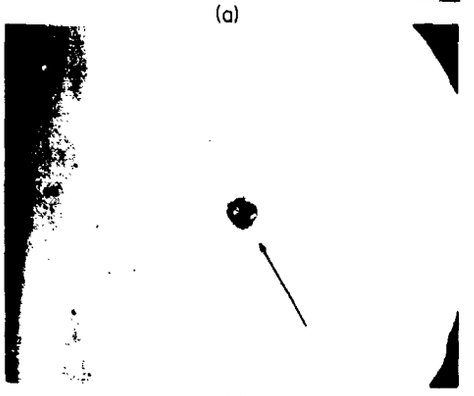

(b)

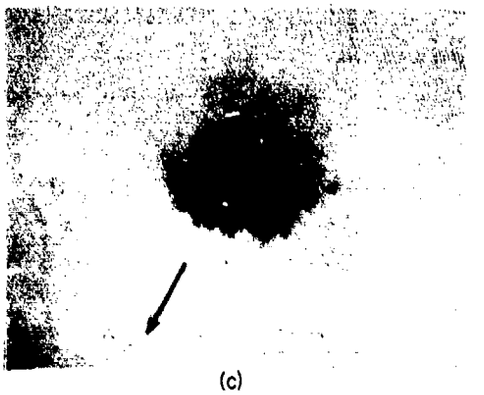

(c)

Fig. 4. Photomicrograph of a 20-μm-radius water droplet being irradiated by a 10.6-μm laser pulse. (a) Droplet before the pulse, (b) droplet during the pulse, (c) droplet 1.3 μsec later. (The arrows show the direction of the pulse in projection.)

Fig. 6. A 12-μm (radius) droplet 2.0 μsec after incidence of the laser pulse.

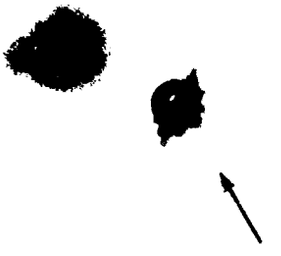

Fig. 7. A 26-μm (radius) droplet 0.9 μsec after incidence of the laser pulse.

Figure D15: Photomicrographs of drops undergoing explosive evaporation on irradiation by a focussed 10.6 μm pulse with power density ~ 10 MW/cm^2

(After P. Kafalas and A.P. Ferdinand, ref. D31)

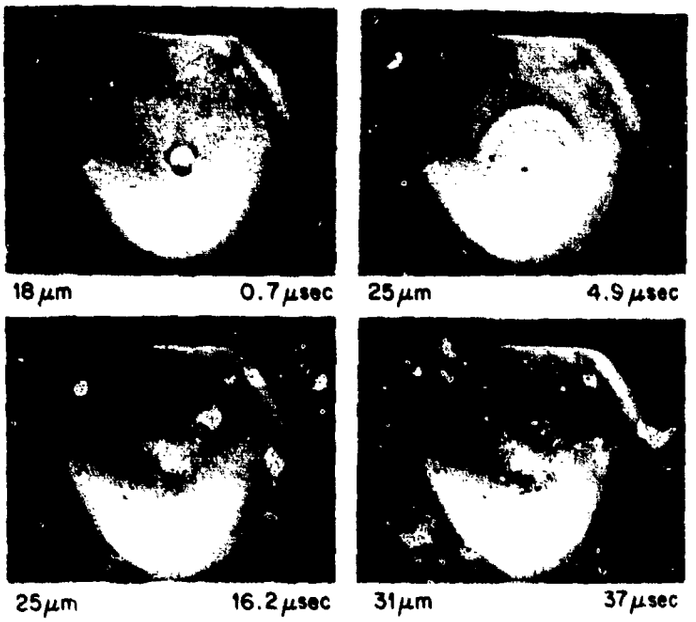

Fig. 2. Schlieren photographs of four exploding water droplets. The radius of each droplet is shown at the left and the elapsed time since the 10.6-μm laser pulse is shown at the right. Laser pulse direction: left to right.

Fig. 4. Schlieren photograph of a large (~35 μm radius) exploding water droplet 6.7 μsec after the 10.6-μm laser pulse. Laser pulse direction: left to right.

Figure D16: Schlieren photographs of the expanding shock and vapour fronts associated with the explosive evaporation of drops irradiated by focussed TEA laser pulses.

(After P. Kafalas and J. Herrmann, ref. D32)

APPENDIX X1: THERMAL BLOOMING AND BEAM DEFLECTION REFERENCES

(E: experimental T: theoretical)

(E1) W.R. Callen, B.G. Huth and R.G. Pantell, Optical Patterns of Thermally Self-defocused Light, Appl. Phys. Lett. 11, 103 (1967)

(E2) E.A. McClean, L. Sica and A.J. Glass, Interferometric Observations of Absorption Induced Index Change Associated with Thermal Blooming, Appl. Phys. Lett. 13, 369 (1968).

(E3) F.G. Gebhardt and D.C. Smith, Effects of Wind on Thermal Defocusing of CO_2 Laser Radiation, Appl. Phys. Lett. 14, 52 (1969).

(E4) D.C. Smith, Thermal Defocusing of CO_2 Laser Radiation in Gases, IEEE J. Quant. Electr. QE-5, 600 (1969).

(E5) J.R. Kenemuth, C.B. Hogge and P.V. Avizonis, Thermal Blooming of a 10.6μ Laser Beam in CO_2, Appl. Phys. Lett. 17, 220 (1970).

(E6) H. Kleinman and R.W. O'Neil, Deflection of a CO_2 Laser Beam in an Absorbing Gas, J. Opt. Soc. Amer. 61, 12 (1971).

(E7) F.G. Gebhardt and D.C. Smith, Effects of Diffraction on the Self-induced Thermal Distortion of a Laser Beam in a Crosswind, Appl. Opt. 11, 244 (1972).

(E8) F.G. Gebhardt and D.C. Smith, Kinetic Cooling of a Gas by Absorption of CO_2 Laser Radiation, Appl. Phys. Lett. 20, 129 (1972)

(E9) R.G. Buser and R.S. Rohde, Severe Self-Induced Beam Distortion in Laboratory Simulated Laser Propagation at 10.6μ, Appl. Opt. 12, 205 (1973).

(E10) R.G. Buser, R.S. Rhode, P.J. Berger, F.G. Gebhardt and D.C. Smith, Transient Thermal Blooming of Single and Multiple Short Laser Pulses, Appl. Opt. 14, 2740 (1975).

(T1) J. Wallace and M. Camac, Effects of Absorption at 10.6μ on Laser Beam Transmission, J. Opt. Soc. Amer. 60, 1587 (1970).

(T2) A.D. Wood, M. Camac and E.T. Gerry, Effects of 10.6μ Laser Induced Air Chemistry on the Atmospheric Refractive Index, Appl. Opt. 10, 1877 (1971).

(T3) J.N. Hayes, P.B. Ulrich and A.H. Aitken, Effects of the Atmosphere on the Propagation of 10.6μ Laser Beams, Appl. Opt. 11, 257 (1972).

(T4) P.V. Avizonis, C.B. Hogge, R.R. Butts and J.R. Kenemuth, Geometric Optics of Thermal Blooming in Gases. Part I, Appl. Opt. 11, 554 (1972)

(T5) P.B. Ulrich and J. Wallace, Propagation Characteristics of Collimated, Pulsed Laser Beams through an Absorbing Atmosphere, J. Opt. Soc. Amer. 63, 8 (1973).

(T6) A.H. Aitken, J.N. Hayes and P.B. Ulrich, Thermal Blooming of Pulsed Focused Gaussian Laser Beams, Appl. Opt. 12, 193 (1973).

(T7) A.K. Ghatak and S.K. Sharma, Thermal Self-defocusing of Laser Beams, Appl. Phys. Lett. 22, 141 (1973).

(T8) L.R. Bissonette, Thermally Induced Non-linear Propagation of a Laser Beam in an Absorbing Fluid Medium, Appl. Opt 12, 719 (1973)

(T9) R.F. Lutomirski and R.G. Buser, Mutual Coherence Function of a Finite Optical Beam and Application to Coherent Detection, Appl. Opt. 12,2153 (1973).

(T10) J. Wallace and J.Q. Lilley, Thermal Blooming of Repetitively Pulsed Laser Beams, J. Opt. Soc. Amer. 64, 1651 (1974).

(T11) J. Wallace and J. Pasciak, Compensating for Thermal Blooming of Repetitively Pulsed Lasers, J. Opt. Soc. Amer. 65, 1257 (1975).

APPENDIX X2: PARTICLE SIZING METHODS

(a) Direct particle sizing methods (1 - 6) involve the measurement of imprints left on a slide coated with a material such as MgO or gelatine as a current of air impacts the drops onto the slide. For example, a four-stage Casella impactor (2) draws air through a series of four jets behind each of which is a gelatine coated glass disc; at about 17.5 litres min^{-1} airflow the first disc collects 100μm drops, the second 10μm, the third 3.5μm and the fourth 1.3μm. The stains left on the gelatine are sized and counted over some area; the ratio of stain diameter to drop diameter is typically 1.4, a factor that has to be found by calculation. The efficiency of collection of drops of different sizes at any stage may vary, and must be corrected for.

(b) The Direct impact methods give low sampling rates, require tedious measurement and analysis, and disturb the sample. Optical methods are free from these objections. They are based on a number of different principles.

(i) Most direct is the correlation between the intensity of the light pulse scattered by a drop and the size of the drop (7,8). In an ingenious application of this principle drops are drawn through an intracavity He-Ne laser beam causing substantial change of output (9). A multichannel pulse height analyser enables particles in various size groups to be counted and the counts can then be directly displayed on an oscilloscope as a count spectrum. In a commercial version* of this instruments cover the following size ranges: 0.01 - 5 μm, 2 - 30 μm, 20 - 300 μm and 300 - 4500 μm. Sampling rate is up to 10kHz.

(ii) Forward scattering of light from a laser beam collected by a lens gives a diffraction pattern at the focal plane of the lens from which can be deduced (at least in principle) the size distribution of the scatterers (10 - 13). In a commercial version* of this principle a multielement detector at the focal plane picks up the diffraction rings from different size groups. The output is multiplexed through an analogue to digital converter, the particle size distribution computed in a signal processor and the spectrum displayed on a paper printout.

(iii) Measurement of the velocity spectrum of the drops and use of Stokes's law gives the radius distribution. Optical heterodyne techniques for the velocity spectrum have been exploited by Gollub et al (14). An alternative is to allow the drops to move through an interference fringe pattern produced by interfering a split laser beam. By picking up the scattered light pulses, then extracting the periodicity of the pulse train with great accuracy by multiplying the train with many different time-delayed versions of itself (digital correlator) one measures the velocity spectrum for particles traversing the interference pattern (15). A commercial version is available.*

(iv) Knollenberg (16) has measured particle sizes by projecting a magnified image as a shadow over an array of optical fibres feeding photomultipliers.

(v) A fifth method, yet to be tested, is an adaptation of the method employed by Cole et al (17). The descent of drops under Stokes's law will be gated a distance d above a 0.63μm laser beam transverse to

their descent paths. On opening the gate, first the largest and then progressively smaller drops pass through the beam. Monitoring the forward scattered diffraction lobe at the focal plane of a lens, the oscillation of the Mie efficiency factor $K(a)$ with drop radius $a = a/k$ is sought on a chart recording using a logarithmic amplifier to give output proportional to $N(a)\, a^2 K(a)$.

(c) Electrostatic methods for sizing drops have been investigated by Keily and Millan (18). The additional capacitance added as a drop strikes a collection electrode causes a small pulse of extra charging current proportional to the volume of the drop added.

*Particle Measuring Systems, Boulder, Colorado 80301
•Precision Dev..es and Systems, Malvern, England WR14 1AL

APPENDIX X2 REFERENCES

1 H.K.Weickmann and H.J.auf Kampe, J. Meteorol. 10, 204 (1953)
2 K.R.May, Quart. J. Roy. Met. Soc. 87, 374 (1961)
3 L.F.Clague, J. Appl. Meteorol. 4, 549 (1965)
4 J.Warren, J. Atmos. Sci. 26, 1049 (1969)
5 P.B.MacReady Jr and D.M.Takeuchi, J. Appl. Meteorol. 7, 591 (1968)
6 P.A.Spyers-Duran and R.R.Brabam Jr, J. Appl. Meteorol. 6, 1108 (1967)
7 B.A.Silverman, B.J.Thompson and J.H.Ward, J. Appl. Meteorol. 3, 790 (1964)
8 H.H.Blau Jr, M.L.Cohen, L.B.Lapson, P.von Thuna, R.T.Ryan and D.Watson, Appl. Opt. 9, 1798 (1970)
9 S.A.Schleusener, Rev. Sci. Instr. 39, 1916 (1968)
10 J.R.Hodkinson, Appl. Opt. 5, 839 (1966)
11 P.F.Mullaney and P.N.Dean, Appl. Opt.8, 2361 (1969)
12 A.L.Fymat, Rassegna Internazionale Electronica Nucleare e Aerospaziale, Rome, 1973
13 L.C.Chow and C.L.Tien, Appl. Opt. 15, 378 (1976)
14 J.P.Gollub, I.Chabay and W.H.Flygare, Appl. Opt. 12, 2838 (1973)
15 E.R.Pike, J. Phys. D: Appl. Phys. 5, (1972)
16 R.G.Knollenberg, J. Appl. Meteorol. 9, 86 (1970)
17 J.E.Cole III, R.A.Dobbins and H.Semerjian, J. Appl. Meteor. 9, 684 (1970)
18 D.P.Keily and S.G.Millan, J. Meteorol. 17, 349 (1960)

APPENDIX X3

A compact 50-J CO_2 TEA laser with VUV preionization and the discharge mechanism*

P. F. Browne and P. M. Webber

Physics Department, University of Manchester Institute of Science and Technology, Manchester M60 1QD, England

(Received 9 February 1976; in final form 1 April 1976)

A design is reported for a compact and simply constructed CO_2 TEA laser giving pulses of up to 50 J with 0.1-μs duration from a discharge of dimensions $45 \times 6 \times 6$ cm^3. The gas is preionized by VUV irradiation from two lines of 34 series arcs to either side of the uniform field electrodes to which potentials of +50 kV and −50 kV are applied. The mechanism of preionization and the conditions for a uniform discharge are considered.

PACS numbers: 42.60.Cz, 52.80.Mg, 84.70.+p

The ionization of large volumes of gas at atmospheric and higher pressures by vacuum ultraviolet or x-ray irradiation from arrays of hot transient arcs is of increasing interest. The phenomenon has played a central role in the development of TEA lasers. The earliest TEA lasers excited the gas mix by corona discharges from arrays of pins, which may or may not be fed through ballast resistors.[1–3] These were superceded by devices employing uniform-field electrodes, the gas being preionized by means of an auxiliary discharge of limited energy; the auxiliary discharge (of corona type) may occur to a dielectric-coated electrode,[4–6] to pins,[7,8] or to fine tungsten wires to either side of the main discharge.[9–11] More recently, there has emerged a third class of device in which the gas is preionized by vacuum ultraviolet radiation from arrays of hot transient arcs in series[12] or in parallel[13,14] with the main discharge. Uniform discharges at atmospheric pressure over gaps as large as 30 cm can be achieved by this method.[15] The mechanism of VUV preionization, however, is still obscure, nor are the conditions for a uniform discharge fully understood.

We report a particularly simple and compact design for a CO_2 TEA laser with VUV preionization, with good performance. Bruce-profiled solid aluminum electrodes with base dimensions 50×15 cm are supported, with a 6-cm gap, inside a Perspex box of dimensions 105×35×25 cm. Reflectors are mounted directly to the end faces; a thick rubber gasket serves both as gas seal and spring loading for three adjustment screws. Shock waves from the discharge do not cause significant misalignment.

For reflectors we have used an uncoated Ge flat (72% reflectivity) and a gold-coated Cu-Zr concave reflector with radius of curvature 3 m, both of diameter 7.5 cm. An unstable resonator also proved effective. Gas flow rates, in l/min, are in the ranges 4–9 He, 2–3 CO_2, 2 N_2.

The gas is preionized by VUV radiation from two lines of arcs to either side of the main electrodes and 28 cm apart (Fig. 1). Each line consists of 34 arcs in series between tungsten or copper pins which are glued into the ravine between touching capillary glass tubes (7-mm o.d.; 2.5-mm i.d.). Earthed conducting rods inside the capillaries polarize the glass and increase the capacity to earth of each pin. The gaps were 3–4 mm. The striking potential was less than 20 kV, but the lines were usually fed from a 0.5-μF capacitor charged to 50 kV, so that 625 J is discharged through 68 arcs. The ringing period of 6 μs indicates a circuit inductance of 1.6 μH, and the peak current $V(C/L)^{1/2}$ then works out at 3000 A.

Breakdown between a main electrode and an arc line (only 7 cm away) was avoided by applying +50 kV to one electrode and −50 kV to the other by means of the circuit shown in Fig. 2. On triggering the pressurized spark gap S′ the capacitor C′ is discharged through the arcs. Apparently due to preionization of the gas, a −50 kV pulse is fed onto the main discharge circuit (heavily outlined in Fig. 2). Thus 100 kV appears across S_2 which breaks down, and since S_1 is in the same chamber of pressurized N_2 it also fires. Thus the main discharge circuit is completed automatically. We have also triggered S_1 independently, using pickup

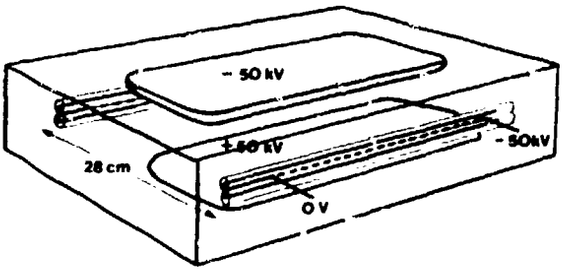

FIG. 1. Bruce-profiled solid aluminum electrodes of base dimensions 15×53 cm and the two lines of preionization arcs.

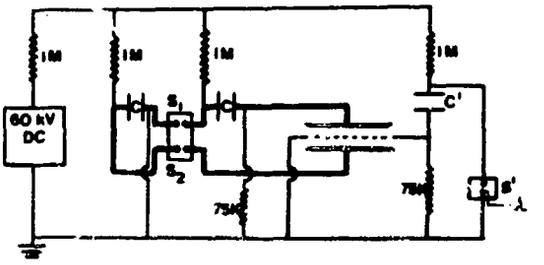

FIG. 2. Circuit diagram with low-inductance main discharge circuit heavily outlined.

FIG. 3. Double air breakdown.

from the arc current to fire a thyratron which feeds a current pulse, via a variable delay line, to the primary of an induction coil. Varying the delay by ~1 μs seems not to be important. We have operated the system with $C = 0.12$ μF and with $C = 0.25$ μF (Fig. 2). For the latter value (not the maximum) 625 J is discharged through a gas volume of $15 \times 6 \times 6$ cm^3 (= 1.62 l), which is 386 J/l.

Imprints burnt onto polaroid film suggest a fairly uniform power density over an area of 20 cm^2 with a sharp boundary. A photon drag detector indicates typically 12.5 MW/cm^2 for the mean power density, implying 250-MW total power. The pulse width, at half-power points, is 0.1 μs, implying pulse energy of 25 J. Interference fringes visible on these imprints, which rotate as the Ge output window is rotated, are attributed to a wedge of 5.7 arc min on this etalon. Figure 3 shows double air breakdown at about 10 and 24 cm in front of a concave mirror which intercepts the beam. The above data was obtained with $C = 0.12$ μF (Fig. 2).

Concerning preionization of the gas, two mechanisms would seem to operate. (i) Impurities, reaction products, or additives, which are present in a few parts per million, may be ionized by photons with quantum energy less than 11 eV.[16,17] Above about 11 eV CO_2 absorbs strongly, and the molecule ionizes at 13.7 eV. N_2 ionizes at 15.6 eV. At 10.4 eV quantum energy the absorption coefficient of CO_2 has reached 500 cm^{-1} and that of N_2 650 cm^{-1}.[10,19] This type of photoionization apparently was operative in systems described by Levine and Javan[20] and by Seguin *et al.*[12]

(ii) Other systems (including our own) seem not to be affected by additives. Also, Judd and Wada[13] report that a LiF filter reduced preionization by 80%, although it is transparent up to 11 eV. The question then becomes how can shorter-wavelength radiation propagate over distances of the order of 15 cm. As quantum energy increases well beyond the ionization limit both measured and theoretical photoionization cross sections decrease. For a hydrogenlike atom the theoretical cross section

(b) In the case of class 3 T&A lasers, 200-eV bremsstrahlung from hot localized arcs may account for the preionization. Assume that the arc develops from a single avalanche, and that the current channel, due to shock wave expansion, has radius $c_s t$ after time t, where c_s is the velocity of sound. For $t = 3$ μs one obtains $c_s t = 1$ mm, and for an arc gap of 3 mm the arc volume is 10^{-2} cm^3. If one assumes that 25 eV is lost in ionization per atom in this volume, then 1 J is required to fully ionize the arc volume. If one dissipates an additional 6 J in the arc volume the result should be a 100-eV plasma. The bremsstrahlung power at frequency ν within bandwidth $\Delta\nu$ and solid angle $\Delta\Omega$ from volume V_a is given by[21]

$$J = 5.4 \times 10^{-46} (N_e N_i T^{1/2}) \exp(-h\nu/kT) V_a \Delta\nu \Delta\Omega \text{ W} \quad (1)$$

for unity Gaunt factor and single ionization. Substituting $h\nu = 200$ eV, $\Delta\nu/\nu = 0.2$, $kT = 100$ eV, $N_e = N_i = 2.7 \times 10^{19}$ cm^{-3}, $V_a = 10^{-2}$ cm^3, and $\Delta\Omega = \frac{1}{8}$, one finds $J = 567$ W/arc. In 3 μs some 68 arcs will give enough 200-eV quanta to ionize 1.6 l to the extent of 2×10^{12} ion pairs cm^{-3}.

n_0 ion pairs due to preionization will grow to n pairs after avalanching through distance x, where $n = n_0 \exp(\alpha x)$. When unit area of anode has collected n/α electrons, there will have developed in front of the cathode a thin layer L of positive space charge, with thickness x and charge per unit area en. α. The field of this space charge will cancel the applied field E throughout the major part of the gap when $en/\alpha = E/4\pi$. For $E = 16$ kV/cm and $\alpha = 10$ cm^{-1} (an uncertain value intermediate between the pure gas values[22]), the applied field is annulled when $n = 10^{12}$ cm^{-3}. Avalanching is now quenched, except possibly between L and the cathode if photoelectric emission occurs.

An unwanted channel discharge will occur if a single avalanche is allowed to develop into a streamer,[23–25] which implies a change from collisional to uv ionization at short range—soft uv can travel only $\sim 2 \times 10^{-3}$ cm before being absorbed. This change occurs when the field due to the blobs of space charge at the head of an avalanche becomes comparable to E, giving two regions of field intensification. The critical field is reached for an avalanche multiplication of order $10^{7.23}$. The accelerating field must be cut off before an individual avalanche attains this multiplication. That is, we re-

quire $n \approx n_e \approx 10^6$, implying $n_0 \approx 10^4$ cm^{-3} for $n \approx 10^{12}$ cm^{-3}.

In the absence of secondary emission at the cathode some $2.5 \cdot 10^{14}$ ion pairs cm^{-3} would have to be created in order to discharge 0.25 μF at 50 kV through 1.6 l of gas. Since avalanching is quenched at 10^{12} pairs cm^{-3}, there must occur successive bursts of avalanching interspersed with intervals when the positive space charge is being swept out. This sweeping out may be rapid, because the mobility of He_2^+ ions, 20 cm s(V cm)$^{-1}$, exceeds that of any other ion by an order of magnitude and because the field between L and the cathode will be greater than E (the ion current would equal the electron current for a field of about $20E$). It is probably important that the preionization should continue during the discharge.

The authors are indebted to Dr. C. Smalley for machining, by means of a specially cut tool, Bruce-profile electrodes.

*Work supported by U.S. Department of the Army, European Research Office, London.

[1]A.J. Beaulieu, Appl. Phys. Lett. **16**, 504 (1970).
[2]R. Fortin, Can. J. Phys. **49**, 257 (1971).
[3]K.A. Laurie and M.M. Hale, IEEE J. Quantum Electron. **QE-7**, 530 (1971).
[4]R. Dumanchin, M. Michon, J.C. Farcy, G. Boudinet, and J. Rocca-Serra, IEEE J. Quantum Electron. **QE-8**, 163 (1972).
[5]A.K. Laflamme, Rev. Sci. Instrum. **41**, 1578 (1970).
[6]G. Otis, Rev. Sci. Instrum. **43**, 1621 (1972).
[7]L.J. Denes and O. Farish, Electron. Lett. **7**, 337 (1971).
[8]M.C. Richardson, A.J. Alcock, K. Leopold, and P. Burton, IEEE J. Quantum Electron. **QE-9**, 236 (1973).
[9]P.R. Pearson and H.M. Lamberton, IEEE J. Quantum Electron. **QE-8**, 145 (1972).
[10]T.Y. Chang and O.R. Wood, IEEE J. Quantum Electron. **QE-8**, 721 (1972).
[11]D.S. Stark, P.H. Cross, and H. Foster, IEEE J. Quantum Electron. **QE-11**, 774 (1975).
[12]H.J. Seguin, J. Tulip, and D.C. McKen, IEEE J. Quantum Electron. **QE-10**, 311 (1974).
[13]O.P. Judd and J.Y. Wada, IEEE J. Quantum Electron. **QE-10**, 12 (1974).
[14]A.J. Alcock, K. Leopold, and M.C. Richardson, Appl. Phys. Lett. **23**, 562 (1973).
[15]M.C. Richardson, K. Leopold, and A.J. Alcock, IEEE J. Quantum Electron. **QE-9**, 934 (1973).
[16]I. Liberman and W.D. Parlow, IEEE J. Quantum Electron. **QE-10**, 750 (1974).
[17]A.J. Palmer and Y.J. Wada, IEEE J. Quantum Electron. **QE-10**, 751 (1974).
[18]G.L. Weissler, Handb. Phys. **21**, 304 (1956).
[19]G.V. Marr, *Photoionization Processes in Gases* (Academic, New York, 1967), pp. 175 and 184.
[20]J.S. Levine and A. Javan, Appl. Phys. Lett. **22**, 55 (1973).
[21]C.W. Allen, *Astrophysical Quantities*, 2nd ed. (University of London Press, London, 1963), p. 90.
[22]S.C. Brown, *Basic Data of Plasma Physics* (MIT Press, Cambridge, Mass., 1959), p. 125.
[23]H. Raether, *Electron Avalanche and Breakdown in Gases* (Butterworth, Washington, D.C., 1964).
[24]K.H. Wagner, Z. Phys. **139**, 165 (1966).
[25]E.D. Lozanskii and O.B. Firsov, Sov. Phys.-JETP **29**, 367 (1969).